ISSN : 2959-6602

Journal of Engineering and Technology (JET)

Volume 4

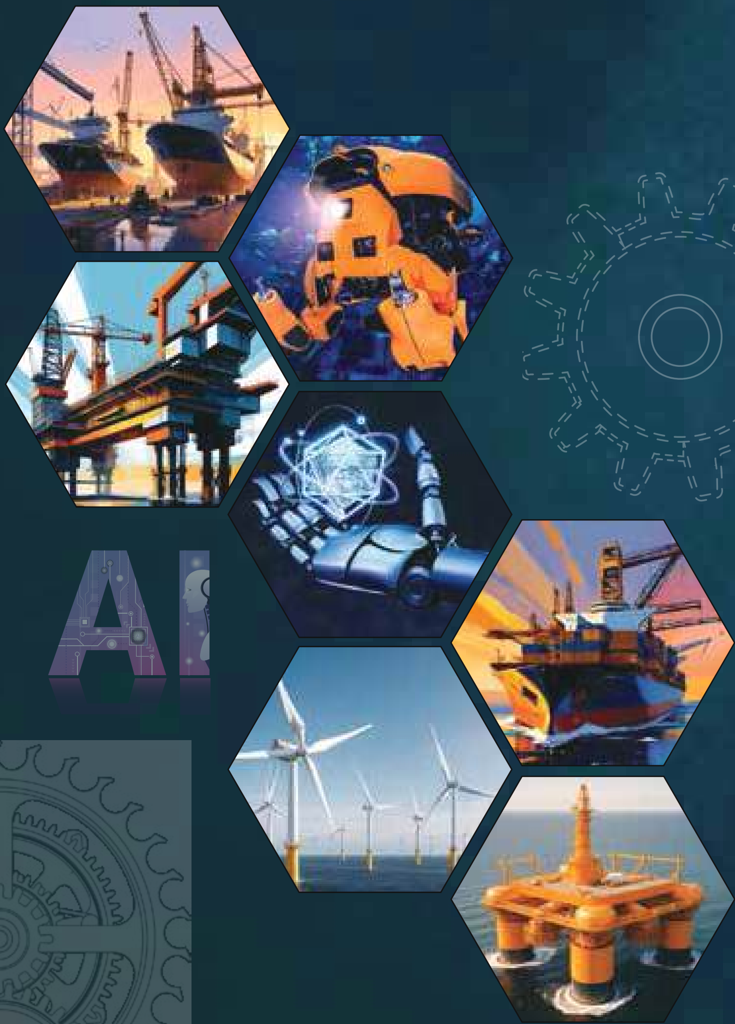

Faculty of Engineering and Technology
Bangladesh Maritime University

ISSN 2959-6602

Journal of Engineering and Technology

Volume 4, June 2026
ISSN : 2959-6602

The Research Journal of
Faculty of Engineering and Technology
Bangladesh Maritime University

We Strive for Maritime Excellence

ISSN : 2959-6602

Disclaimer

All articles published in this journal undergo editorial and peer review in accordance with the journal's academic and publication standards. The Journal is committed to maintaining the quality, integrity, and scholarly reliability of its published content.

ISSN

2959-6602

Submission

The initial submission of manuscripts and editorial correspondence should be sent to the Chief Editor , Journal of Engineering and Technology (JET), Faculty of Engineering and Technology , Bangladesh Maritime University, 14/06-14/23, Pallabi, Mirpur-12, Dhaka-1216, email: jet@bmu.edu.bd. Authors should consult the notes for contributors at the back of the journal before submitting their manuscripts.

Published by

Faculty of Engineering and Technology,
Bangladesh Maritime University
14/06-14/23, Pallabi Mirpur-12, Dhaka- 1216

Designed by

Ayyid Raihan, Session 2019-20, ID: 19411014,
Tasnim Tabassum Tusti, Session 2019-20 ID: 19411011, and
Md. Abdullah Al Muhymen Araf , Session 2020-21 ID: 21411019

ISSN : 2959-6602

Table of Contents

ISSN : 2959-6602

Journal of Engineering and Technology

Journal of Engineering and Technology (JET) - Vol : 04 (2026)
ISSN : 2959-6602

Bangladesh
Maritime University

Amine-Based Post-Combustion CO_2 Capture: Theory, Mathematical Modelling, and Python Implementation

Md. Mahedi Hasan Bappy[a], Md Ashraful Islam Opi[b], Dr. S M Rashidul Hasan[c]*, Dr. Khandakar Akhter Hossain[d]

Abstract:

Meeting the International Maritime Organization's ambition of net-zero shipping by around 2050 will require carbon-mitigation technologies that are both retrofit-compatible and rigorously characterised for the constrained environment of a vessel. This paper presents a transparent, modular Python framework for simulating amine-based post-combustion CO_2 capture (PCC) and assessing its suitability for onboard application. The model couples five physically grounded sub-models: Arrhenius temperature-dependent reaction kinetics, van't Hoff and Henry's-law vapour–liquid equilibrium, Hatta-number enhancement of reactive mass transfer, a two-film overall mass-transfer-coefficient formulation, and a counter-current staged absorber resolved by iterative successive substitution. Four industrially relevant solvents—monoethanolamine (MEA), diethanolamine (DEA), methyldiethanolamine (MDEA), and piperazine—are characterised across a range of operating conditions. For the base case (5 M MEA, 40 °C, 5% CO_2 inlet), the model predicts a capture efficiency of 89.68%, removing 13.82 kg CO_2 h^{-1} per column, with a Hatta number of 1678 confirming operation in the fast pseudo-first-order regime. Sensitivity analyses identify absorber temperature as the dominant performance variable, followed by amine selection, and show that increasing amine concentration does not monotonically improve capture—an outcome that underscores the value of rigorous simulation over heuristic design. In contrast to proprietary process simulators, the framework is fully open, independently testable, and structured as reusable modules, providing a foundation for techno-economic assessment and the design of compact onboard carbon-capture systems for maritime decarbonization.

Article History :
Received 13 April 2026
Accepted 23 June 2026
Published 30 June 2026

Keywords: post-combustion capture; amine absorption; Hatta number; maritime decarbonization; process modelling; MEA.

[a,b]*Department of Naval Architecture and Offshore Engineering, Bangladesh Maritime University*
[c]*Assistant Professor, Department of Naval Architecture and Offshore Engineering, Bangladesh Maritime University*
[d]*Vice Chancellor, Bangladesh Maritime University, Email: admiraldrakhter@bmu.edu.bd*
**Corresponding Author: Email: rashidul.naoe@bmu.edu.bd*

Nomenclature

Symbol	Description	Unit	Symbol	Description	Unit
k_2	Second-order reaction rate constant	$L·mol^{-1}·s^{-1}$	E_i	Instantaneous-reaction enhancement limit	–
H_e	Henry's-law constant for CO_2	$Pa·L·mol^{-1}$	D_{am}	Diffusivity of amine in solution	$m^2·s^{-1}$
K_G	Overall gas-phase mass-transfer coeff.	$mol·Pa^{-1}·m^{-2}·s^{-1}$	N_{CO2}	Molar flux of CO_2 per stage	$mol·s^{-1}$
k_L	Liquid-film mass-transfer coeff.	$m·s^{-1}$	A_{eff}	Effective interfacial area per stage	m^2
k_G	Gas-film mass-transfer coeff.	$mol·Pa^{-1}·m^{-2}·s^{-1}$	p_{CO2}^*	Equilibrium partial pressure of CO_2	Pa
N	Number of theoretical stages	–	G_{mol}	Molar gas flow rate	$mol·s^{-1}$
α	Solvent CO_2 loading	$mol·mol^{-1}$	P	Operating (total) pressure	Pa
r	Reaction rate	$mol·L^{-1}·s^{-1}$	Q_g	Flue-gas volumetric flow rate	$m^3·s^{-1}$
$[CO_2]$	Dissolved CO_2 concentration	$mol·L^{-1}$	L_{mol}	Molar liquid flow rate	$mol·s^{-1}$
$k_{2,ref}$	Rate constant at reference temp.	$L·mol^{-1}·s^{-1}$	Q_l	Liquid volumetric flow rate	$L·s^{-1}$
E_a	Apparent activation energy	$kJ·mol^{-1}$	y	Gas-phase CO_2 mole fraction	$mol·mol^{-1}$
R	Universal gas constant	$J·mol^{-1}·K^{-1}$	j	Stage index	–
T	Operating (absorber) temperature	K	a_p	Specific packing surface area	$m^2·m^{-3}$
T_{ref}	Reference temperature (298.15 K)	K	D	Column internal diameter	m
p_{CO2}	Partial pressure of CO_2	Pa	H	Packed column height	m
$H_{e,ref}$	Henry's constant at reference temp.	$Pa·L·mol^{-1}$	n	Iteration index	–
ΔH_{abs}	Enthalpy (heat) of absorption	$kJ·mol^{-1}$	MW	Molar mass (molecular weight)	$g·mol^{-1}$
E	Enhancement factor	–	y_{in}	CO_2 inlet mole fraction	$mol·mol^{-1}$
Ha	Hatta number	–	α_{lean}	Lean-solvent loading	$mol·mol^{-1}$
C_{am}	Free amine concentration	$mol·L^{-1}$	η	CO_2 capture efficiency	%
D_{CO2}	Diffusivity of CO_2 in solution	$m^2·s^{-1}$	L/G	Liquid-to-gas molar ratio	$mol·mol^{-1}$

1. Introduction

International shipping is responsible for roughly 2.5–3% of global anthropogenic greenhouse-gas emissions, the overwhelming majority of which is CO_2 [1]. Although maritime transport remains among the most carbon-efficient modes of freight per tonne-kilometre, its absolute footprint is substantial: in 2018 the sector emitted approximately 1,076 million tonnes of greenhouse gases, of which 1,056 million tonnes were CO_2 [2]. Without decisive intervention, these emissions are projected to rise by 50–250% by 2050, placing the industry on a trajectory fundamentally at odds with international climate commitments.

In response, the International Maritime Organization (IMO) has adopted binding targets to reduce carbon intensity by at least 40% by 2030 and to reach net-zero emissions by or around 2050 [3]. Meeting these targets within a fleet dominated by long-lived, fossil-fuelled vessels has intensified research into a broad portfolio of mitigation strategies, among which the chemical absorption of CO_2 directly aboard ships has emerged as particularly attractive [4]. Onboard carbon capture and storage (OCCS) is appealing precisely because it is retrofit-compatible: it can be deployed on existing vessels without requiring a wholesale transition to alternative propulsion fuels. Using rigorous process simulations, feasibility studies have demonstrated the potential of monoethanolamine and piperazine for capturing CO_2 from both diesel and LNG marine engines, while quantifying the thermal-energy demand that governs practical deployment [5].

Among point-source capture options, post-combustion capture by reactive absorption into aqueous alkanolamines is the most extensively developed and widely deployed [6], [7], [8], [9], [10], [11]. In a typical configuration, CO_2-laden flue gas is contacted counter-currently with an aqueous amine solution in a packed absorber column [9], [10], where the amine reversibly forms carbamate or bicarbonate complexes depending on its molecular class. The CO_2-rich solvent is then regenerated in a stripper at elevated temperature, liberating the captured CO_2 and returning lean solvent to the absorber for reuse [11], [12]. This selectivity, reversibility, and technological maturity make amine absorption a credible pathway for maritime decarbonization.

1.1 Research Gap

Despite the apparent simplicity of this cyclic process, the engineering of an amine absorber is governed by a tightly coupled interplay of reaction kinetics, vapour–liquid equilibrium, gas–liquid mass transfer with simultaneous chemical reaction, and exothermic heat effects. Capturing these interacting phenomena with sufficient fidelity is essential for reliable column design, efficiency prediction, and process optimisation—requirements that become especially acute within the severe space, weight, and energy constraints of a ship. Commercial process simulators can model these systems with high rigour, but their proprietary and largely closed architectures limit transparency, modular reuse, and rapid early-stage screening of solvents and operating conditions for shipboard application. There remains, therefore, a clear need for an accessible, physically transparent, and extensible modelling framework tailored to the demands of maritime OCCS design.

This paper addresses that need by presenting a structured, openly documented Python simulation tool that resolves the governing physics through five interconnected sub-models: (1) Arrhenius-based, temperature-dependent reaction kinetics; (2) van't Hoff equilibrium solubility; (3) Hatta-number theory for the enhancement of gas–liquid mass transfer; (4) a two-film resistance model for the overall mass-transfer coefficient; and (5) a counter-current staged absorber solved by iterative successive substitution. The remainder of the paper develops the theoretical basis of each component, details its computational implementation, presents the simulation results, and reports a sensitivity analysis across the principal operating variables governing capture performance.

2. Methodology

The modelling methodology adopted in this work translates the governing physical theory developed in detail in Section 3 - into a deterministic, fully open simulation workflow. Rather than relying on the closed correlations of a commercial process simulator, the framework is constructed as a set of independent, individually verifiable sub-models that are coupled in a fixed computational sequence. This section describes the overall modelling approach and system boundary, states the simplifying assumptions on which the model rests, and sets out the integrated solution workflow used to obtain a converged column solution.

2.1 Modelling Approach and System Boundary

The framework resolves the absorber through five physically grounded sub-models executed in sequence: (1) temperature-dependent reaction kinetics; (2) vapour–liquid equilibrium; (3) reactive-mass-transfer enhancement; (4) a two-film overall mass-transfer coefficient; and (5) a counter-current staged absorber. Each sub-model is implemented as a self-contained Python function that consumes a shared input state and returns a single physically meaningful quantity, so that any individual component can be tested, replaced, or refined without disturbing the others. Figure 1 shows how data propagate through these components: operating conditions and amine properties feed the kinetic and equilibrium models, whose outputs 〖k〗_2 (T) and $H_e(T)$ drive the enhancement-factor and two-film calculations, which in turn supply the overall coefficient KG to the staged absorber that produces the engineering results.

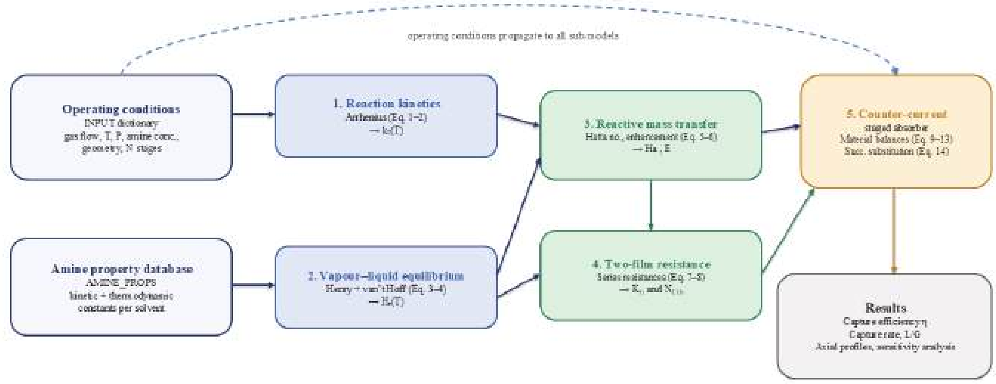

Figure 1: Architecture of the coupled simulation framework, showing the flow of data between the five sub-models.

The thermodynamic and transport theory of Section 3 governs the local behaviour at every point in the column, while the system boundary of the present model is restricted to the absorber itself. Figure 2 places this boundary within the complete shipboard capture loop: engine exhaust is cooled and contacted counter-currently with lean amine in the absorber, treated gas is vented to the stack, and the CO_2-rich solvent passes through a lean/rich heat exchanger to a stripper, where heat supplied by a reboiler regenerates the solvent and liberates CO_2 for compression and onboard storage. The absorber is the decisive unit for capture performance and the focus of this study; the regeneration train is represented only as the thermal context against which the regeneration-energy estimate is interpreted.

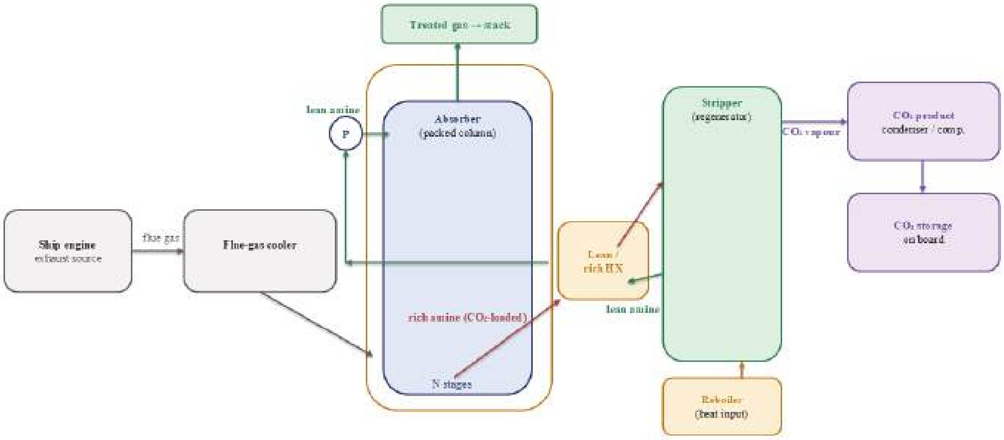

Figure 2: Process flow diagram of the shipboard post-combustion capture system.

2.2 Modelling Assumptions

To keep the model transparent and computationally light while retaining the dominant physics, the following assumptions are made:

- Steady-state operation: all stage compositions are time-invariant at convergence.
- Isothermal column: the absorber operates at a single specified temperature, so the exothermic heat of absorption is not resolved spatially.
- Ideal-gas behaviour of the flue-gas phase, used to convert volumetric to molar flow (Equation 9).
- Interfacial equilibrium described by Henry's law (Equation 3), with temperature dependence from the van't Hoff relation (Equation 4).
- Constant liquid- and gas-film mass-transfer coefficients (kL, kG), set by the packing and hydrodynamics rather than computed from local flow.
- Well-mixed theoretical stages: each of the N stages is treated as a uniform control volume with a single gas and liquid composition.
- Negligible solvent evaporation, water balance, and column pressure drop over the modelled height.

2.3 Integrated Solution Workflow

For a given case, the workflow proceeds in two phases. In the first, the temperature-dependent properties and transport parameters are evaluated once: the rate constant $k_2(T)$ and the Henry's constant $H_e(T)$ are obtained from Equations 2 and 4, and these feed the Hatta number, enhancement factor, and overall mass-transfer coefficient of Equations 5–7. In the second phase, the staged absorber is solved iteratively. The gas- and liquid-composition arrays are initialised, and the material balances of Equations 11 and 12 are applied stage-by-stage from the bottom of the column to the top. Because the gas composition is fixed at the bottom and the liquid composition at the top, the stage equations constitute a boundary-value problem that is resolved by successive substitution: the full stage sweep is repeated until the largest change in any stage composition between consecutive iterations falls below the tolerance of Equation 14, subject to a ceiling of 500 iterations. Figure 3 summarises this procedure. Once converged, the capture efficiency, capture rate, solvent loading, and regeneration-energy metrics are computed from the resolved composition profiles, and the same pipeline is re-evaluated under perturbed inputs to generate the sensitivity results of Section 4.4.2.

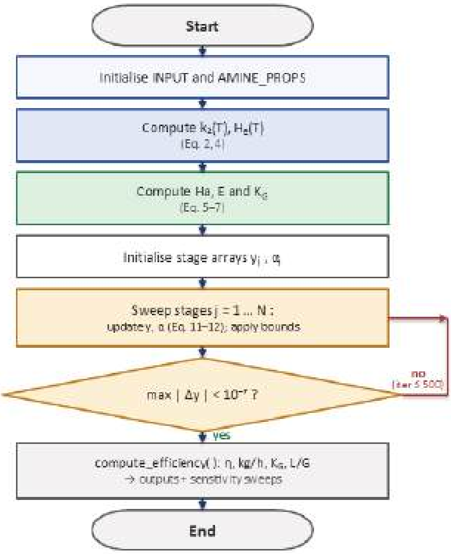

Figure 3: Solution algorithm for the counter-current staged absorber, resolved by successive substitution to the convergence tolerance of Equation 14.

3. Theoretical Background

This section develops the physical and chemical theory underlying the five sub-models introduced in Section 2. It proceeds from the absorption chemistry of the amine–CO_2 system, through the reaction kinetics and vapour–liquid equilibrium that set the local driving forces, to the reactive mass-transfer and two-film resistance relations that determine the overall rate of CO_2 uptake. Together these relations provide the constitutive equations on which the modelling workflow of Section 2 operates.

3.1 Amine Absorption Chemistry

When CO_2 contacts an aqueous amine solution, it follows one of two reaction pathways depending on the amine class. For primary and secondary amines such as MEA and DEA, the dominant pathway is carbamate formation:

$$2RNH_2 + CO_2 \rightleftharpoons RNHCOO^- + RNH_3^+$$

This route, the zwitterion mechanism, accounts for the rapid reaction between CO_2 and primary or secondary amines [13], [14]. Tertiary amines such as methyldiethanolamine do not form stable carbamates; instead, they act as a base that catalyses CO_2 hydration toward bicarbonate [15], [16]. Because direct carbamate formation is sterically hindered for tertiary amines such as MDEA [17], CO_2 is absorbed through the slower base-catalysed hydration reaction:

$$R_3N + CO_2 + H_2O \rightleftharpoons R_3NH^+ + HCO_3^-$$

Piperazine, a cyclic diamine, can react at both nitrogen atoms to form a zwitterionic intermediate, giving it a very high reaction rate. The overall capacity for CO_2 uptake is quantified by the solvent loading α, defined as the moles of absorbed CO_2 per mole of amine. Maximum loadings range from 0.5 mol/mol for primary amines (the theoretical carbamate stoichiometry) up to 1.0 mol/mol for tertiary amines [18].

3.2 Reaction Kinetics: The Arrhenius Equation

The reaction between CO_2 and an amine follows a second-order rate law, first-order in both CO_2 and amine concentration:

$$r = k_2(T) \cdot [CO_2] \cdot [\text{Amine}] \tag{1}$$

The temperature dependence of the rate constant k_2 is described by the Arrhenius equation, conveniently expressed relative to a reference state (typically 298.15 K):

$$k_2(T) = k_{2,ref} \cdot \exp\left[-\frac{E_a}{R} \cdot \left(\frac{1}{T} - \frac{1}{T_{ref}}\right)\right] \tag{2}$$

where k_{2ref} is the rate constant at the reference temperature T_{ref}, E_a is the apparent activation energy, and R is the ideal-gas constant [19]. The exponential term quantifies how the reaction accelerates with temperature. Among the amines considered, piperazine has the lowest activation energy (33 kJ/mol) and MEA an intermediate value (41 kJ/mol), whereas MDEA has the highest (55 kJ/mol) and therefore the slowest intrinsic kinetics.

3.3 Vapour–Liquid Equilibrium: Henry's Law and the van't Hoff Equation

At the gas–liquid interface, CO_2 is assumed to be in local thermodynamic equilibrium between the two phases. For dilute systems this is described by Henry's law:

$$[CO_2]_{liq} = \frac{p_{CO_2}}{H_e} \tag{3}$$

where p_{CO2} is the partial pressure of CO_2 (Pa) and H_e is the Henry's-law constant (Pa•L/mol). A larger H_e indicates lower solubility, so the amine must work against a less favourable equilibrium [20]. The temperature dependence of H_e is captured by the van't Hoff equation, which relates the constant to the enthalpy of absorption [21]. Because CO_2 absorption is exothermic, H_e rises with temperature—less CO_2 dissolves as the system heats up:

$$H_e(T) = H_{e,ref} \exp\left[-\frac{\Delta H_{abs}}{R}\left(\frac{1}{T} - \frac{1}{T_{ref}}\right)\right] \tag{4}$$

Here ΔH_{abs} is the molar enthalpy of absorption (J/mol), negative for an exothermic process. For MEA, $\Delta H_{abs} \approx -84$ kJ/mol—among the highest of the common amines—which explains both its excellent solubility and its substantial regeneration-energy penalty.

3.4 Mass Transfer with Chemical Reaction: Hatta Number and Enhancement Factor

Gas–liquid mass transfer in a reactive system differs fundamentally from purely physical absorption. The chemical reaction consumes dissolved CO_2 within the liquid film, steepening the concentration gradient and increasing the interfacial flux. This acceleration is quantified by the enhancement factor E, the ratio of the actual absorption flux to that achievable by physical diffusion alone. The controlling dimensionless group is the Hatta number (Ha) [22], the square root of the ratio of the maximum reaction rate in the film to the maximum diffusive transport rate:

$$\mathrm{Ha} = \frac{\sqrt{k_2 C_{am} D_{CO_2}}}{k_L} \tag{5}$$

where $D_{CO2} \approx 1.7\times10^{-9}$ m²/s is the diffusivity of CO_2 in amine solution and $k_L \approx 2\times10^{-4}$ m/s is the liquid-phase mass-transfer coefficient (set by the packing and hydrodynamics). The relationship between Ha and E follows two limiting regimes: in the slow-reaction regime (Ha $\ll$ 1), $E \approx 1 + Ha^2/2$, the reaction being too slow to enhance transfer appreciably; in the fast-reaction regime (Ha $\gg$ 3), E ≈ Ha, the reaction occurring entirely within the film and strongly enhancing transfer. Enhancement is bounded above by the instantaneous-reaction limit E_i, in which the rate is governed purely by amine diffusion toward the interface:

$$E_i = C_{am}\sqrt{\frac{D_{am}}{D_{CO_2}}} + 1 \tag{6}$$

For the base case (5 M MEA at 40 °C), Ha ≈ 1678, placing operation firmly in the fast-reaction regime; CO_2 reacts within the liquid film almost immediately upon dissolution, and the enhancement factor is consequently very large relative to physical absorption.

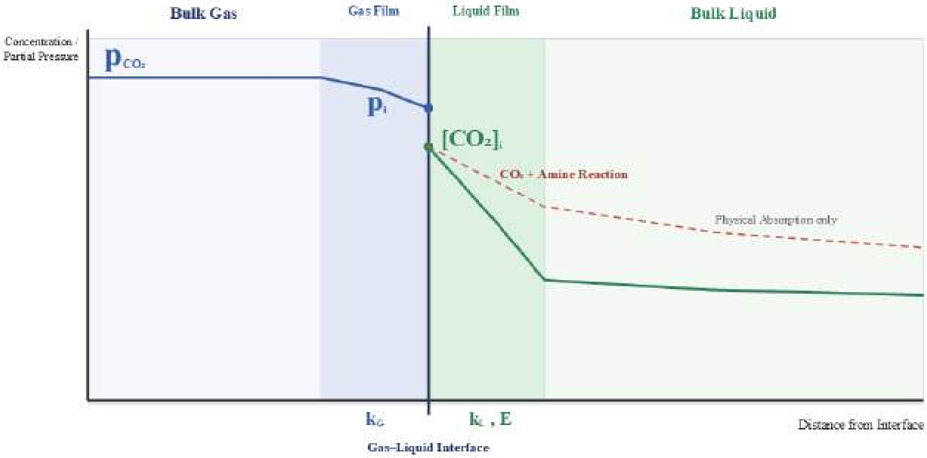

Figure 4: Two-film model of CO_2 absorption.

3.5 Overall Mass-Transfer Coefficient

The rate of CO_2 transfer across the interface is governed by two resistances in series—a gas-side film resistance and a liquid-side film resistance—combined through two-film theory into the overall gas-phase mass-transfer coefficient K_G:

$$\frac{1}{K_G} = \frac{1}{k_G} + \frac{H_e}{Ek_L} \tag{7}$$

By analogy with resistances in an electrical circuit, the total resistance is the sum of the individual contributions. Dividing the liquid-side term by E reflects the substantial reduction afforded by the chemical reaction. For amine systems, where $k_G \sim 5\times10^{-6}$ mol/Pa/m²/s, the gas-side resistance tends to dominate when H_e is small (highly soluble amines such as MEA). The molar flux at any point in the column is then:

$$N_{CO_2} = K_G A_{eff}\left(p_{CO_2} - p^*_{CO_2}\right) \tag{8}$$

where A_eff is the effective interfacial area (m²) and p^*_{CO2} is the equilibrium partial pressure of CO_2 corresponding to the current liquid loading. The difference (p_{CO2} -p^*_{CO2}) is the thermodynamic driving force for absorption.

4. Results, Analysis and Discussion

4.1 Counter-Current Staged Absorber Model

4.1.1 Column Configuration and Material Balances

The absorber is modelled as a series of N theoretical stages (default N = 20), each representing a thin section of the packed column. Gas flows upward, entering at stage 1 (the bottom), while liquid flows downward, entering at stage N (the top). This counter-current arrangement maximises the mass-transfer driving force over the column height [23]. The molar gas and liquid flow rates follow from the inlet conditions via the ideal-gas law and the known amine concentration [23]:

$$G_{mol} = \frac{PQ_g}{RT} \tag{9}$$

$$L_{mol} = Q_l C_{am} \times 1000 \tag{10}$$

At each stage j, the gas-phase mole fraction y and liquid-phase loading α are updated from material balances derived from Equation 8:

$$y_{j+1} = y_j - \frac{N_{CO_2}}{G_{mol}} \tag{11}$$

$$\alpha_j = \alpha_{j+1} + \frac{N_{CO_2}}{L_{mol}} \tag{12}$$

The interfacial area available per stage follows from the column geometry and packing characteristics:

$$A_{eff} = a_p\left(\frac{\pi D^2}{4}\right)\left(\frac{H}{N}\right) \tag{13}$$

where a_p is the specific packing surface area, D is the column diameter, and H/N is the height per stage (m).

4.1.2 Iterative Solution Procedure

Because the absorber is a boundary-value problem—the gas composition is fixed at the bottom and the liquid composition at the top—a direct marching solution is not possible.

The system is instead solved by successive substitution: an initial guess is made for all stage compositions, and the balance equations are applied repeatedly until convergence, judged by

$$\max_j \left|y_j^{(n)} - y_j^{(n-1)}\right| < 10^{-7} \quad (14)$$

Convergence is typically achieved within 50–100 iterations for well-posed operating conditions. A ceiling of 500 iterations with a tolerance of 10-7 ensures numerical stability without excessive computation time.

4.2. Amine Solvent Properties and System Inputs

4.2.1 Amine Property Database

The model incorporates literature-derived physicochemical constants for four industrially relevant solvents, stored in a property dictionary within the code and summarised in Table 1.

Table 1: Physicochemical constants for the amine solvents used in the model.

Amine	$k_{,ref}$ (L/mol/s)	E_a (kJ/mol)	Max load (mol/mol)	$H_{,ref}$ (Pa·L/mol)	ΔH_{abs} (kJ/mol)	MW (g/mol)
MEA	6000	41	0.50	3400	−84	61.1
DEA	1200	47	0.45	5200	−72	105.1
MDEA	10	55	1.00	8000	−58	119.2
Piperazine	70000	33	0.50	2000	−90	86.1

4.2.2 Operating Input Parameters

The simulation requires a complete set of operating conditions, supplied through a structured input dictionary. Table 2 lists the base-case inputs used for the primary run.

Table 2: Base-case input parameters.

Parameter	Symbol	Value	Unit
Flue-gas volumetric flow	Q_g	0.05	m^3/s
CO_2 inlet mole fraction	y_{in}	0.05	mol/mol
Operating temperature	T	313.15	K (40 °C)
Operating pressure	P	101325	Pa (1 atm)
Amine concentration	C_{am}	5.0	mol/L
Liquid flow rate	Q_l	1.0	L/s
Lean solvent loading	α_{lean}	0.15	mol CO_2/mol amine
Column height	H	5.0	m
Column diameter	D	0.30	m
Packing surface area	a_p	250	m^2/m^3
Number of stages	N	20	—

4.3. Computational Implementation

4.3.1 Code Architecture

The model is implemented as a single Python script organised into eight self-contained functions, each corresponding to a distinct computational task and each independently testable, modifiable, or replaceable. Data flow from a central input dictionary through the property lookup, the kinetic and thermodynamic correlations, the enhancement-factor and overall-coefficient calculations, the iterative stage solver, and finally the efficiency and sensitivity routines (Figure 1). Two design choices underpin the architecture. First, all operating conditions are centralised in a single dictionary, INPUT, so that every function receives one object and modified copies for parametric studies can be generated by dictionary unpacking. Second, the fixed material constants for each solvent are held in a separate AMINE_PROPS dictionary, cleanly separating system-specific inputs from material-specific data. Only the standard library math and the numerical libraries NumPy and SciPy are required; scipy.integrate.solve_ivp and scipy.optimize.brentq are imported to future-proof the code for ODE-based column models and equilibrium root-finding, allowing extension to continuous differential formulations without structural change.

4.3.2 Kinetic, Thermodynamic, and Mass-Transfer Functions

The functions rate_constant() and henry_constant() implement Equations 2 and 4. Both share the same mathematical form—an exponential correction applied to a reference value—but carry different physical meaning: the former captures kinetic acceleration with temperature, the latter the reduction in solubility with temperature. Each accepts temperature in Kelvin and returns the value at the operating temperature, superseding the reference values held in AMINE_PROPS. The function enhancement_factor() computes the Hatta number from Equation 5 and then applies the piecewise expression for $E = Ha$ for $Ha > 3$, and $E \approx 1 + Ha^2/2$ otherwise—bounded above by the instantaneous limit of Equation 6. Representative transport properties ($D_{CO_2} = 1.7\times10^{-9}$ m²/s, $D_{am} = 0.8\times10^{-9}$ m²/s, $k_L = 2\times10^{-4}$ m/s) are appropriate for 5M amine solutions at moderate temperatures. Finally, overall_mass_transfer() applies the two-film resistance model of Equation 7 to return a single lumped coefficient K_G that encapsulates all gas- and liquid-side resistances and feeds directly into the stage model.

4.3.3 Stage Solver, Efficiency Metrics, and Sensitivity Analysis

The computational core, stage_model(), initialises the gas- and liquid-composition arrays and runs an outer iteration of up to 500 cycles; within each cycle an inner loop traverses all N stages, applying the material balances of Equations 11 and 12. A lower bound on the driving force prevents non-physical reverse absorption, and an upper bound on loading prevents unrealistic solvent overloading; convergence is declared when the largest change in any stage composition between successive iterations falls below 10^{-7}. The routine compute_efficiency() then derives all engineering-relevant metrics: the capture efficiency η from the inlet and outlet CO_2 mole fractions; the capture rate in kg/h from the molar capture rate and the molar mass of CO_2 (44 g/mol); the solvent utilisation, expressing the fraction of available amine capacity actually used; and a first-order regeneration-energy estimate indicating the associated energy penalty. The sensitivity_analysis() routine demonstrates the model as a parametric tool, executing three independent sweeps—amine concentration from 2 to 7 mol/L, temperature from 30 to 60 °C, and amine type across all four solvents—each created by dictionary unpacking and evaluated through the full stage-model and efficiency pipeline.

4.4 Base-Case Simulation Results

For the base-case configuration (5 M MEA, 40 °C, 5 % CO_2 inlet, 5 m column), the model converges to a steady-state capture efficiency of 89.68 %. The principal output metrics are summarised in Table 3.

Table 3: Summary of base-case simulation results.

Metric	Value
CO_2 capture efficiency (η)	89.68%
CO_2 captured	13.82 kg/h
CO_2 inlet mole fraction	5.00%
CO_2 outlet mole fraction	0.516%
Rich solvent loading	0.1674 mol/mol
Solvent loading utilisation	3.49%
Liquid-to-gas molar ratio (L/G)	2.57 mol/mol
Regeneration-energy estimate	2109 kJ/kg CO_2
Hatta number (Ha)	1678
Enhancement factor (E)	4.43
Overall MTC (K_G)	1.04×10^{-6} mol/Pa/m²/s

The Hatta number of 1678 confirms that MEA operates firmly in the fast pseudo-first-order regime: the CO_2 reaction is essentially complete within the liquid film before the dissolved gas can diffuse into the bulk. The low solvent utilisation of 3.49 % indicates that the liquid flow rate is well above what the column and inlet conditions require. This is a clear opportunity for optimisation—reducing the liquid circulation rate would lower pumping costs and regeneration energy without compromising capture, provided the driving force remains adequate.

4.4.1 Axial Composition Profiles

The stage model also yields axial profiles of gas-phase CO_2 mole fraction and liquid-phase loading along the column. The gas CO_2 concentration falls from 5.00 % at the bottom (inlet) to 0.516 % at the top (outlet), with most of the removal occurring in the lower half of the column. The liquid loading rises only modestly, from 0.150 mol/mol (lean inlet at the top) to 0.167 mol/mol (rich outlet at the bottom), consistent with the high solvent flow rate and low utilisation. The sharp decline in gas CO_2 in the lower stages and the flattening of the profile near the top indicate that the absorber approaches a mass-transfer pinch at its upper end—behaviour characteristic of amine systems in which the equilibrium partial pressure above the lean solvent is far below the inlet gas partial pressure, producing a large driving force at the column base.

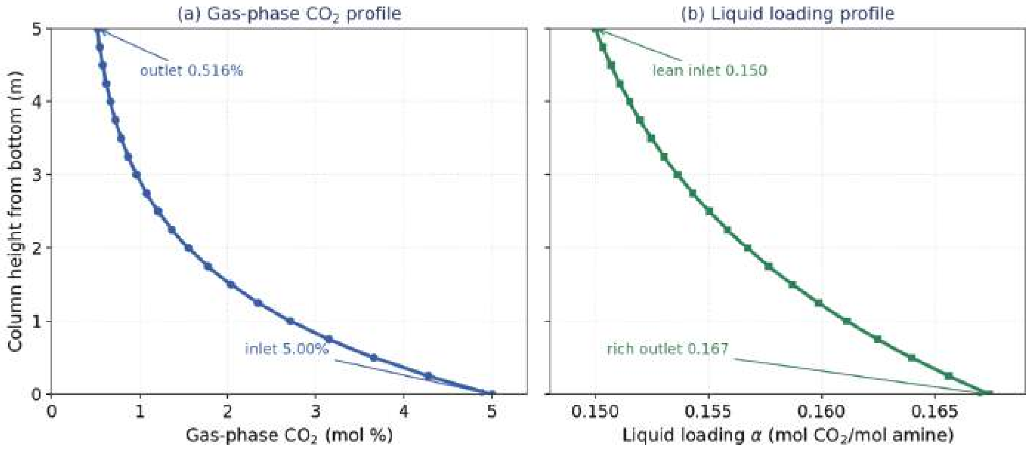

Figure 5: Predicted axial profiles of (a) gas-phase CO_2 mole fraction and (b) liquid CO_2 loading along the column height for the base case (5 M MEA, 40 °C).

4.4.2 Sensitivity Analysis

Table 4 presents the three sensitivity sweeps. The trends are directly relevant to ship-based CCS design.

Table 4: Sensitivity analysis: effect of concentration, temperature, and amine type on capture efficiency.

Variable	Test value	η (%)	Ha	E	Regen. (kJ/kg)
Conc. (mol/L)	2	91.49	—	2.37	2109
	5	89.68	1678	4.43	2109
	7	86.02	—	5.80	2109
Temp. (°C)	30	60.71	1294	4.43	1950
	40	89.68	1678	4.43	2109
	50	96.34	2141	4.43	2245
Amine type	MEA	89.68	1678	4.43	2109
	DEA	76.57	—	4.43	1836
	MDEA	47.50	—	4.43	1518
	Piperazine	94.79	—	4.43	2245

Temperature is the most influential variable. Raising the absorber from 30 to 50 °C lifts efficiency from 60.71 % to 96.34 %, driven by faster reaction kinetics (a higher k_2 through the Arrhenius term). This gain comes at the cost of increased regeneration energy, reflecting the classic absorption–regeneration trade-off of amine systems. For shipboard applications where engine waste heat may be available, operating at an elevated absorber temperature could therefore be advantageous.

ISSN : 2959-6602

Amine concentration behaves counter-intuitively. Over the tested range, efficiency is highest at the lowest concentration—91.49 % at 2 mol/L—and declines to 89.68 % at 5 mol/L and 86.02 % at 7 mol/L. As concentration rises, the equilibrium partial pressure above the solvent increases through loading effects, eroding the driving force even as the intrinsic kinetics improve. The net effect is that capture does not increase monotonically with amine strength, and an optimum exists toward the lower end of the range—an outcome that underscores the importance of rigorous simulation over simple intuition when designing amine systems.

Solvent choice has the largest absolute effect. Piperazine attains the highest efficiency (94.79 %) owing to its very high intrinsic rate constant, whereas MDEA captures only 47.50 % under the same conditions because of its slow base-catalysed mechanism. MEA remains the practical benchmark, combining high reactivity, moderate cost, and well-understood regeneration behaviour, despite carrying the highest regeneration energy among the single-amine options.

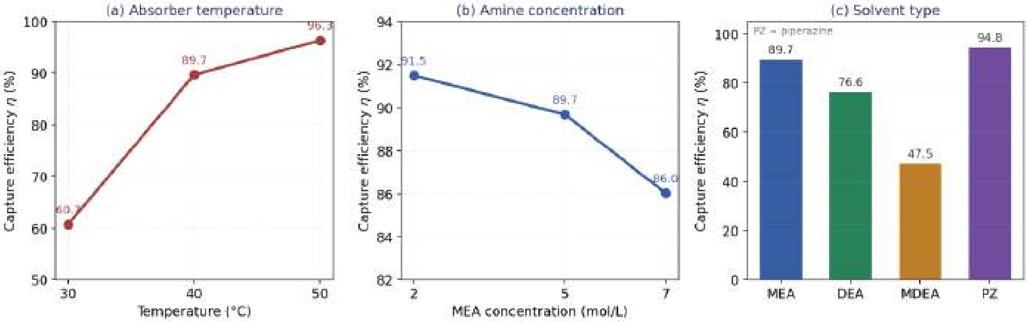

Figure 6: Sensitivity of capture efficiency to (a) absorber temperature, (b) MEA concentration, and (c) solvent type, computed from the data of Table 4.

These findings rest on deliberate simplifications that frame how far they can be read. The film coefficients kL and kG are held constant, although both vary with packing hydrodynamics and local flow; the interface is described by a simple Henry's law, which cannot reproduce the non-ideal vapour–liquid equilibrium that real amine solutions show at high loading; and the column is treated as isothermal, so the temperature rise from the exothermic reaction—and its feedback on kinetics and equilibrium—is not resolved. Because only the absorber is modelled, the stripper, the lean–rich exchanger, and practical effects such as solvent degradation, volatility, and foaming all lie outside the present scope, even though they matter in maritime service.

Each of these points to a clear next step: replacing the constant coefficients with hydrodynamic correlations (Billet–Schultes or Rocha–Bravo–Fair) and Henry's law with an e-NRTL or Kent–Eisenberg description, coupling the energy balance through a rate-based column model in scipy.integrate.solve_ivp, and adding a stripper to close the energy and mass loop for a full techno-economic and IMO CII assessment.

5. Conclusions

A transparent, modular Python model has been developed for simulating amine-based post-combustion CO_2 capture in support of maritime decarbonization. The model integrates five physically grounded sub-models spanning reaction kinetics (Arrhenius), gas–liquid equilibrium (Henry's law and van't Hoff), reactive mass transfer (Hatta number and enhancement factor), two-film resistance (the overall mass-transfer coefficient), and counter-current staged absorption (successive-substitution iteration). For the base case of 5 M MEA at 40 °C with a 5 % CO_2 inlet, it predicts a capture efficiency of 89.68 %, equivalent to 13.82 kg CO_2 removed per hour from a 0.05 m^3/s flue-gas stream in a 5 m × 0.3 m packed column; a Hatta number of 1678 confirms fast-reaction operation, and the sensitivity analysis identifies temperature as the dominant process variable, followed by amine selection.

The modular structure allows straightforward adaptation to different operating conditions, column geometries, and solvents, and provides a foundation for more detailed process simulation, techno-economic assessment, and ultimately the design of compact OCCS systems for integration into ship engine-room layouts. The predicted behaviour is physically consistent with published data on pilot-scale amine absorbers, lending confidence to the model within its stated assumptions.

References

[1] S. Deng and Z. Mi, 'A review on carbon emissions of global shipping', Mar. Dev., vol. 1, p. 4, 2023, doi: 10.1007/s44312-023-00001-2.

[2] 'Fourth IMO greenhouse gas emissions study – highlights published'. Accessed: Jun. 26, 2026. [Online]. Available: https://www.imo.org/en/mediacentre/pages/whatsnew-1596.aspx

[3] 'Landmark agreement towards achieving net-zero emissions from global shipping by 2050 - Mobility and Transport'. Accessed: Jun. 26, 2026. [Online]. Available: https://transport.ec.europa.eu/news-events/news/landmark-agreement-towards-achieving-net-zero-emissions-global-shipping-2050-2025-04-11_en

[4] A.-A. Sarbanha, F. Larachi, S.-M. Taghavi, M. Thiboutot-Rioux, A. Boudreau, and G. Dugas, 'Mitigation of Ship Emissions: Overview of Recent Trends', Ind. Eng. Chem. Res., vol. 62, no. 4, pp. 1707–1724, Feb. 2023, doi: 10.1021/acs.iecr.2c03621.

[5] A. Einbu et al., 'Energy assessments of onboard CO2 capture from ship engines by MEA-based post combustion capture system with flue gas heat integration', Int. J. Greenh. Gas Control, vol. 113, p. 103526, 2021, doi: 10.1016/j.ijggc.2021.103526.

[6] 'Methods and Techniques for CO2 Capture'. Accessed: Jun. 26, 2026. [Online]. Available: https://encyclopedia.pub/entry/19427

[7] A. Padurean, C.-C. Cormos, A.-M. Cormos, and P.-S. Agachi, 'Multicriterial analysis of post-combustion carbon dioxide capture using alkanolamines', Int. J. Greenh. Gas Control, vol. 5, no. 4, pp. 676–685, Jul. 2011, doi: 10.1016/j.ijggc.2011.02.001.

[8] A. Akhdhar, A. S. Al-Bogami, N. Akhtar, and W. A. El-Said, ‘Progress in Post-Combustion Carbon Dioxide Capture, Direct Air Capture, and Utilization’, Catalysts, vol. 15, no. 9, p. 807, Aug. 2025, doi: 10.3390/catal15090807.

[9] M. Wang, A. Lawal, P. Stephenson, J. Sidders, and C. Ramshaw, ‘Post-combustion CO2 capture with chemical absorption: A state-of-the-art review’, Chem. Eng. Res. Des., vol. 89, no. 9, pp. 1609–1624, Sep. 2011, doi: 10.1016/j.cherd.2010.11.005.

[10] I. Von Harbou, H. P. Mangalapally, and H. Hasse, ‘Pilot plant experiments for two new amine solvents for post-combustion carbon dioxide capture’, Int. J. Greenh. Gas Control, vol. 18, pp. 305–314, Oct. 2013, doi: 10.1016/j.ijggc.2013.08.002.

[11] Z. Liang, W. Rongwong, H. Liu, K. Fu, H. Gao, and P. Tontiwachwuthikul, ‘Recent progress and new developments in post-combustion carbon-capture technology with amine based solvents’, Int. J. Greenh. Gas Control, vol. 40, pp. 26–54, 2015, doi: 10.1016/j.ijggc.2015.06.017.

[12] F. Lopez, R. M. Filho, V. H. Dos Santos Ramos, E. C. Fulguera, L. V. Fregolente, and M. W. Maciel, ‘CO2 capture systems using MDEA solvent: stripper with reboiler or with steam? An exergetic evaluation and performance enhancement criteria’, Fuel, vol. 408, p. 137449, Mar. 2026, doi: 10.1016/j.fuel.2025.137449.

[13] P. V. Kortunov, M. Siskin, M. Paccagnini, and H. Thomann, ‘CO2 Reaction Mechanisms with Hindered Alkanolamines: Control and Promotion of Reaction Pathways’, Energy Fuels, vol. 30, no. 2, pp. 1223–1236, Feb. 2016, doi: 10.1021/acs.energyfuels.5b02582.

[14] A. Gholidoust, J. D. Atkinson, and Z. Hashisho, ‘Enhancing CO2 Adsorption via Amine-Impregnated Activated Carbon from Oil Sands Coke’, Energy Fuels, vol. 31, no. 2, pp. 1756–1763, Feb. 2017, doi: 10.1021/acs.energyfuels.6b02800.

[15] E. B. Rinker, S. S. Ashour, and O. C. Sandall, ‘Absorption of Carbon Dioxide into Aqueous Blends of Diethanolamine and Methyldiethanolamine’, Ind. Eng. Chem. Res., vol. 39, no. 11, pp. 4346–4356, Nov. 2000, doi: 10.1021/ie990850r.

[16] B. P. Mandal, M. Guha, A. K. Biswas, and S. S. Bandyopadhyay, ‘Removal of carbon dioxide by absorption in mixed amines: Modelling of absorption in aqueous MDEA/MEA and AMP/MEA solutions’, Chem. Eng. Sci., vol. 56, no. 21–22, pp. 6217–6224, 2001, doi: 10.1016/S0009-2509(01)00279-2.

[17] J. H. Choi, S. G. Oh, Y. I. Yoon, S. K. Jeong, K. R. Jang, and S. C. Nam, ‘A study of species formation of aqueous tertiary and hindered amines using quantitative 13C NMR spectroscopy’, J. Ind. Eng. Chem., vol. 18, no. 1, pp. 568–573, Jan. 2012, doi: 10.1016/j.jiec.2011.11.053.

[18] D. M. D’Alessandro, B. Smit, and J. R. Long, ‘Carbon Dioxide Capture: Prospects for New Materials’, Angew. Chem. Int. Ed., vol. 49, no. 35, pp. 6058–6082, 2010, doi: 10.1002/anie.201000431.

[19] O. Otitoju, E. Oko, and M. Wang, ‘Technical and economic performance assessment of post-combustion carbon capture using piperazine for large scale natural gas combined cycle power plants through process simulation’, Appl. Energy, vol. 292, p. 116893, 2021, doi: 10.1016/j.apenergy.2021.116893.

[20] ‘A Comparative Guide to Argon Solubility in Various Solvents: A Cross-Validation Approach’.

[21] B. Liu, Y. Yu, Z. Liu, Z. Cui, and W. Tian, ‘Prediction of CO2 solubility in aqueous amine solutions using machine learning method’, Sep. Purif. Technol., vol. 354, p. 129306, Feb. 2025, doi: 10.1016/j.seppur.2024.129306.

[22] K. R. Putta, F. A. Tobiesen, H. F. Svendsen, and H. K. Knuutila, ‘Applicability of enhancement factor models for CO2 absorption into aqueous MEA solutions’, Appl. Energy, vol. 206, pp. 765–783, 2017, doi: 10.1016/j.apenergy.2017.08.173.

[23] P. Mores, N. Scenna, and S. Mussati, ‘A rate based model of a packed column for CO2 absorption using aqueous monoethanolamine solution’, Int. J. Greenh. Gas Control, vol. 6, pp. 21–36, 2012, doi: 10.1016/j.ijggc.2011.11.014.

ISSN : 2959-6602

Journal of Engineering and Technology (JET) - Vol : 04 (2026)
ISSN : 2959-6602

Bangladesh
Maritime University

The Role of Backward Linkages for the Development of South Korea's Shipbuilding Sector

Md. Rabbi Raihan Imon[a*], Md. Riad Khan[b], Dr. Khandakar Akhter Hossain[c]

Abstract:

South Korea's shipbuilding industry frequently comes up as one of the major industrial success stories of the late twentieth century. This growth was supported by government planning, financial assistance, technology transfer and the development of heavy industries. One important reason for this success was the fact that of strong backward linkage. Backward linkage is the relation between a primary industry and the other industries or institutions which supply it with materials, parts, services, technology, money and skilled labour. This includes steel makers, marine equipment makers, engine builders, electronics companies, transport services, research centres, universities and training institutions in the shipbuilding sector. Supported by a strong local supply chain, large shipyards such as Hyundai Heavy Industries, Samsung Heavy Industries and Daewoo Shipbuilding became successful. These suppliers contributed to the development of Korean shipbuilding by reducing the reliance of Korean shipyards on imported materials, lowering production cost, improving quality, and saving time while building advanced ships, including LNG carriers, large container ships, and offshore platforms. Industrial clusters in Ulsan, Geoje, Busan, Mokpo and Changwon also helped shipyards and suppliers work closely and solve problems faster. Therefore, this study describes the current status and key factors of backward linkage that have supported South Korea's shipbuilding competitiveness, strength and future development.

Article History :
Received 15 May 2026
Accepted 22 June 2026
Published 30 June 2026

Keywords: Shipbuilding; Backward Linkage; South Korea; Development.

[a,b]*Lecturer, Department of Naval Architecture and Offshore Engineering, Bangladesh Maritime University, Dhaka 1216, Bangladesh* [a]*Email: imon.naoe @bmu.edu.bd* [b]*Email: riad.naoe @bmu.edu.bd*

[c]*Vice-Chancellor, Bangladesh Maritime University, Dhaka 1216, Bangladesh Email: vc@bmu.edu.bd*

[*]*Corresponding Author: Email: imon.naoe @bmu.edu.bd*

1. Introduction

South Korea is surrounded by sea on three sides, so maritime transport and seaborne trade are important for its trade, links with the world, and security. But it became a shipbuilding leader because of policy, not geography alone. From the 1960s to the 2000s, Korea used state support, export-led growth, technology learning, and large investment in heavy industry to build this sector [1] [2]. After the Korean War, it had little money, weak technology, and few shipyard facilities. Over time, national plans helped firms learn to build large and complex ships. Shipbuilding grew with steel, machinery, electronics, and cars. Today, Korean yards are strong in high-value ships such as LNG carriers, very large container ships, and offshore units [3] [4].

The global market shows why this study matters. Allied Market Research estimated the shipbuilding market at USD 142.52 billion in 2020 and expected it to reach USD 195.48 billion by 2030 [5]. UNCTAD reports that China, Japan, and Korea produced 95 percent of world shipbuilding output in 2023 [6]. Figure 1 shows the size of the shipbuilding economy of South Korea compared to the world. Korea was the second-largest shipbuilding country in 2024, with about 27 percent of global completions by compensated gross tonnage (CGT) [4]. The sector also supports exports, jobs, and industrial areas such as Ulsan, Busan, and Gyeongnam [4]. It is led by HD Hyundai, Samsung Heavy Industries, and Hanwha Ocean, which make more than 90 percent of national completions [4]. Still, Korea's success did not come from shipyards alone. It also came from strong backward linkages. These are the industries and services that support shipyards from behind. They include steel, engines, marine equipment, machinery, electronics, finance, skilled workers, design, testing, and research. A modern ship is a complex product, so many suppliers and institutions must work together.

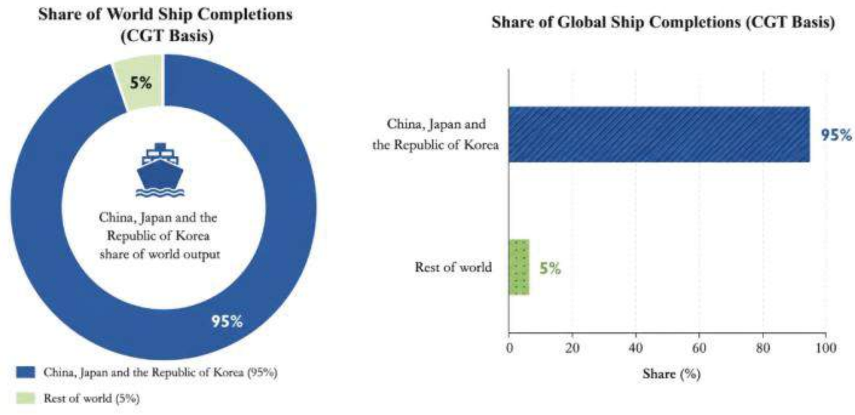

Figure 1: South Korea in the World Shipbuilding Economy[6].

These linkages helped Korea depend less on imported inputs, build faster, and move into higher-value ships. Steel was especially important. Earlier studies show that Korea's steel and shipbuilding sectors grew together through supply ties, large business groups, technology transfer, and state-led investment [7]. Newer research also shows close links between shipyards and domestic steel makers such as POSCO, Hyundai Steel, and Dongkuk Steel, although some steel is still imported [8]. Marine equipment and special parts are also important. Korean shipbuilders worked to raise local content and improve suppliers in machinery, engines, parts, and LNG-related systems [3]. Korea's marine equipment industry has about 2,700 firms and 73,000 workers, and supplied around 90 percent of domestic demand in 2019 [4]. This shows a strong local supplier base, but Korea still needs more upgrading in some green-technology parts.

Backward linkages matter even more now because shipbuilding is changing. Shipping faces strong environmental rules, new fuels, digital tools, automation, cyber risks, labour shortages, and shifting trade routes. In May 2025, 8 percent of the active world fleet by gross tonnage and 53 percent of tonnage on order were designed for alternative fuels [9]. Korea is already supporting green and smart shipbuilding through public R&D for new fuel systems, autonomous ships, and smart production [4]. This paper therefore studies how backward linkages helped Korea build a strong shipbuilding industry, and why they remain important for ither countries. A number of resources and literature are studied to find the reason behind the success of South Korea in shipbuilding using the backward linkages. There are many studies on South Korea's industrial policy, export orientated growth, technological upgrading and the rise of large shipbuilding companies. But the role of backward linkages has not been explored in an integrated way. Existing research tends to isolate government support, steel production, shipyard development, technology transfer or marine-equipment suppliers, rather than explain how these industries, institutions and services interacted to strengthen the shipbuilding sector as a whole. There is also little analysis of the evolution of backward linkages over time. From reducing dependence on imported inputs to supporting the production of high-value, green and digitally advanced ships. Previous studies have not focused enough on the specific mechanisms through which domestic suppliers, skilled labour, finance, research institutions and large business groups contributed to productivity, technological learning. This study is done to find the evolution of South Korea's shipbuilding in the view of backward linkages. For example: state support, expansion of maritime industries, state support, etc.

2. Method of the Study

This study uses a qualitative research approach to analyse the role of backward linkages in the development of the South Korean shipbuilding sector. The main goal is to understand the contribution of supporting industries, government policies, labour systems, technology and supply-chain networks to the development and global success of the Korean shipbuilding industry. This research is largely based on secondary data. Data collected from academic journal articles, books, government reports, industry publications, company reports, statistical databases and other sources. These materials are used to study the shipbuilding industry of South Korea in terms of its development, current status and industrial structure. At first, the history of Korean shipbuilding is evaluated. This gives an insight into the industry's development and South Korea's emergence as one of the world's top shipbuilding countries. The present situation of the industry is then looked at in terms of production capacity, global market share, major players in shipbuilding, technological advancements, and recent challenges.

The main focus of the research is on backward linkages. Backward linkages are defined in this study as the linkages between the shipyards and industries, institutions and services that provide the shipyards with the materials, equipment, technology, finance, infrastructure and skilled labour needed for shipbuilding. The analysis considers the role of government support, the development of the marine equipment industry, the interaction between shipyards and steel producers, industrial clustering, workforce development, technological cooperation, and the development of an efficient supply-chain system

This conclusion is based on the combination of findings from the historical review, the assessment of the current industry and the analysis of backward linkages. The study assesses the role of supporting industries, institutions, skills, technology and supply networks in the enhanced production capacity, competitiveness, innovation and long-term growth of Korean shipbuilding. The combined analysis therefore defines the overall role of backward linkages in the success of the sector.

3. Historical Evolution of Korean Shipbuilding

South Korea's rise in shipbuilding was not luck. After the Korean War, the country had little money, weak technology, and few shipyards. From the 1960s and 1970s, the government considered shipbuilding because it could support exports and create demand for steel, machines, engines, electronics, finance, and skilled workers [1], [10]. The first big stage came in the early 1970s during the Heavy and Chemical Industry drive. The state guided large business groups, or chaebols, into shipbuilding and helped them with credit, foreign loan guarantees, and export support. Hyundai began shipbuilding in 1972, started the Ulsan shipyard, and completed the yard and its first two large ships in June 1974 [11]. Later investment by Daewoo and Samsung shaped the large-firm structure of the industry [3].

Backward linkages were important from the start. A shipyard needs steel plates, engines, cranes, welding tools, design skills, finance, ports, and trained workers. POS CO (Pohang Iron and Steel Company) gave shipbuilders a stronger local steel base. Links with machinery and marine equipment suppliers also reduced imports and improved cost, speed, and production control [7], [12], [13]. In the late 1970s and 1980s, Korean yards grew fast by learning from foreign partners and Japanese shipbuilding. By 1985, Korea's construction-volume share reached 14.4 percent, placing it second after Japan [14]. The mid-1980s were difficult because demand fell, prices dropped, and labour unrest grew. These problems slowed growth but pushed firms to improve productivity and management [10], [15].

The 1990s were a time of upgrading. Korean yards improved design, planning, and quality control. They also moved into LNG carriers, offshore structures, drillships, and very large container ships. HD Hyundai delivered Korea's first LNG carrier in 1994 and developed its own HiMSEN marine engine in 2000 [11]. By the late 1990s and early 2000s, Korea reached the top level of world shipbuilding. Jeong notes that Korea became a world leader in the 2000s and shipbuilding exports reached USD 43.1 billion in 2008 and made up more than 10 percent of total exports. This boom helped many suppliers, including steel, engines, cables, paints, testing, and logistics [15]. Sohn et al. report that Korea led construction volume in 2000 with a 40.7 percent share [14]. Figure 2 gives a simple summary of the main turning points in this history.

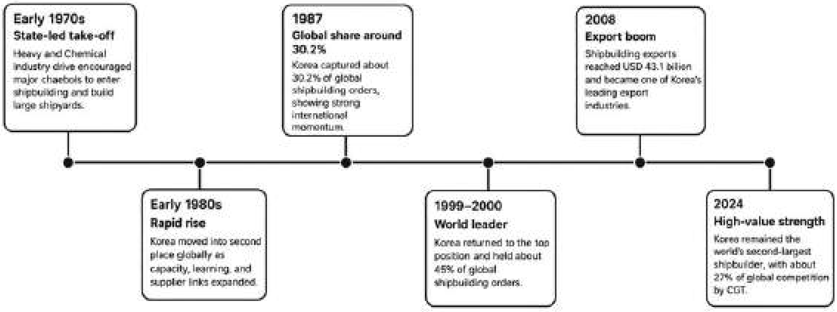

Figure 2: Major milestones in the historical evolution of Korean shipbuilding.

After the 2008 global financial crisis, the industry faced another hard period. Trade slowed, orders fell, and offshore projects became risky after oil prices dropped in the mid-2010s. Some smaller yards closed or were restructured. Daewoo Shipbuilding & Marine Engineering was later acquired by Hanwha and became Hanwha Ocean. In 2024, HD Hyundai, Samsung Heavy Industries, and Hanwha Ocean made more than 90 percent of Korea's national completions [4].

In the 2020s, Korea remains a major shipbuilding country, but competition has changed. China leads in total volume, while Korea is stronger in high-value and difficult ships. China, Japan, and South Korea produced about 95 percent of global shipbuilding output in 2023 [6]. Korea was also the world's second-largest shipbuilding country in 2024, with about 27 percent of global completions on a compensated gross tonnage basis [4].

The next stage depends on green and smart ships. Demand is rising for LNG-fuelled ships, methanol-ready vessels, ammonia and hydrogen fuel systems, autonomous navigation, digital yards, and cleaner production. As of May 2025, 8 percent of the active world fleet and 53 percent of tonnage on the orderbook were designed to use alternative fuels [9]. Figure 3 shows Korea's move into greener and more advanced shipbuilding segments. And, Figure 4 shows Korea's marine equipment base, one of the strongest backward linkages supporting the sector.

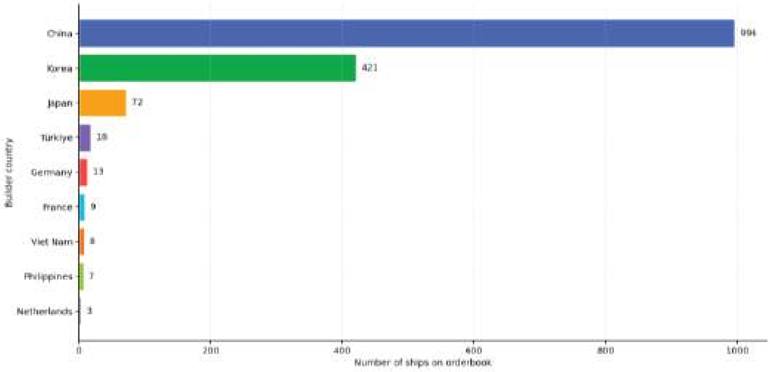

Figure 3: Alternative-fuel newbuild orders by builder country [4].

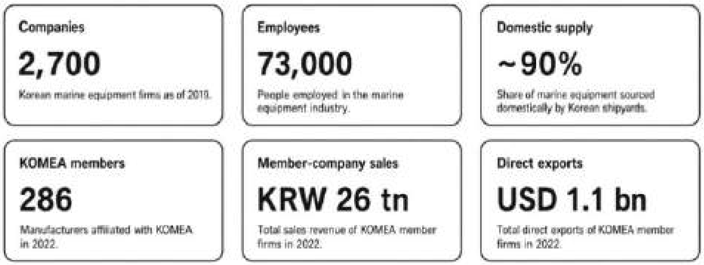

Figure 4: Korea's marine equipment base as a key backward linkage [4].

4. Current Status of Korean Shipbuilding Industry

South Korea is still one of the main countries in global shipbuilding. The industry faced difficult periods after the 2008 financial crisis and during the offshore market slowdown in the mid-2010s. Even after these problems, Korea kept a strong position in the world market [1], [16]. Recent market data also show this strength. In 2024, global shipyard output increased. South Korea held about 28% of global output by compensated gross tonnage (CGT), while China held about 53% and Japan about 12% [17].Figure 5 represents the current status of the South Korean shipbuilding industry from a global perspective.Almost 90% of the shipbuilding work is mainly completed by three giant industries(HD Hyundai, Samsung Heavy Industries, and Hanwha Ocean)[4]. Also, the firms are trying to adopt the eco-friendly technologies.

Figure 5: Current Status of South Korea’s Shipbuilding Industry.

Korea’s strength is not only in the number of ships it builds. Its main strength is in complex and high-value ships. Korean shipyards are strong in LNG carriers, very large container ships, oil tankers, offshore vessels, green ships, and smart ships [16], [18], [19]. The industry is led by three large groups: HD Hyundai, Samsung Heavy Industries, and Hanwha Ocean, formerly Daewoo Shipbuilding and Marine Engineering. Earlier studies also show that these large firms became the centre of Korea’s global shipbuilding position [1], [3], [16]. For this study, Korean shipbuilding should not be seen only as a group of large shipyards. It should be seen as a widser industrial system. Steel firms, engine makers, marine equipment firms, electrical suppliers, design companies, banks, research institutes, and training centres all help the shipyards compete in the global market.

5. South Korean Shipbuilding Sector and Backward Linkages

Backward linkages mean the industries that supply goods and services to shipbuilders. These include steel, machinery, engines, electrical systems, marine equipment, finance, research, training, transport, and other support services. These linkages are very important because a modern ship is made from thousands of parts. Shipyards do not make every part by themselves. They bring together many parts and systems from suppliers. In major shipbuilding countries, about 70-80% of shipbuilding output is linked to intermediate inputs, or goods and services bought from other industries [20].

South Korea shows how a late-developing country can become strong in shipbuilding by building a strong supplier base. Earlier studies report that Korean firms supplied about 85% of the materials and equipment needed by domestic shipyards [21]. This local supply base helped Korea reduce import dependence and improve production speed. These linkages also help the wider economy. Shipbuilding creates demand for steel, metal products, machinery, electronics, ports, logistics, design, classification services, and finance [22]. Figure 6 shows the main way backward linkages support Korean shipbuilding.

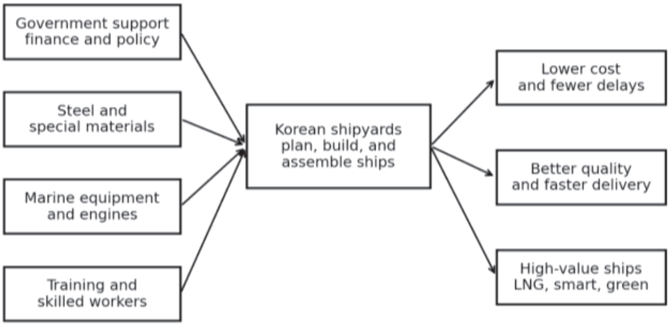

Figure 6: Backward-linkage mechanism in South Korean shipbuilding.

5.1. State Support

From the perspective of the backward linkage of the shipbuilding industry of South Korea, state support is an important thing. Not only for the South Korea, this state support is important for this type of industries in any countries in the world. Government plays a significant role to create a business-friendly environment for an industry to grow. The South Korean government considered shipbuilding a strategic industry that can improve both in commercial and military sector. As this industry is closely related to other industries (i.e. steel, electrical, logistics, ports, etc.), government of South Korea played a significant role.

Starting in 1945, the government promoted the establishment of higher education institutes specifically for fostering professional shipbuilding human resources, beginning with the Department of Shipbuilding Engineering at Korea Maritime University in 1945, followed by programs at Seoul National University (1946), Busan Fishery University (1950), and Inha University (1954) [15]. This educational foundation was essential for building the technical expertise needed throughout the supply chain.

South Korea employed targeted financial support to promote domestic shipbuilding and deepen backward linkages. The 1958 Act on the Encouragement/Promotion of Shipbuilding provided subsidies of up to 40% of shipbuilding costs and loans of 50% or more of costs at 5% annual interest, repayable within 5-10 years. While this early scheme was limited by budget shortfalls, later policies were more successful in building domestic capability. The Shipbuilding Industry Promotion Act of 1967 and the Machinery Industry Cultivation Fund of 1969 promoted shipbuilding technology, local production and domestic self-supply. By the 1970s and 1980s, Korea’s policy focus had broadened to include shipyard capacity, export finance, marine equipment, machinery localization and upstream industrial linkages [4], [15]. The "Planned Shipbuilding System" was implemented with the goal that "Our cargos are transported by our ships, which are built in our shipyards," ensuring minimum shipbuilding quantity even during industry downturns and creating stable demand for domestic suppliers [15].

The shipbuilding industry was strategically included in South Korea's Heavy Chemical Industry (HCI) drive of the 1970s, which targeted upstream supplier industries including steel, metals, machinery, petrochemicals, electronics, and shipbuilding [23], [24]. The government selected shipbuilding as one of six strategic industries based on standards including forward and backward linkages between sectors and their contribution to economic growth [25]. This comprehensive approach included creating policies that promoted the development of technology centers, universities, marine parts companies, service companies, and industrial parks [26].

As a core industry that has extensive linkages with more than 50 other industries, the Korean government has supported the shipbuilding industry for stimulating Korea’s economic growth [2]. Several shipyards were built to strengthen this sector. These are Hyundai Heavy Industry (1973), Samsung Heavy Industries (1977), and Daewoo Shipbuilding and Marine Engineering Co. Ltd (1978). The technological knowledge from Japan was important starting point for South Korea to develop heavy industries. The government of South Korea made collaborations with the government of Japan to improve in the heavy industry sector. The government had created the opportunity of soft loans for the shipbuilding industry. The shipbuilding industry was considered as under the strategic industries development plan, had access to HCI’s policy loans with substantial discounts from the prevailing market rates. In 1979, the market rate of general loans was 19% and that of the HCI’s policy loan was only 9% [27]. In 1970, South Korean government took the initiative of making Chaebols (Samsung, Hyundai, Sambo, Daewoo, LG, SK Group, etc.), who expanded their business drastically by keeping close relation with the government. Later, the giant shipbuilders are grown from them.

5.2. Expansion of Marine Equipment Industry

A strong marine equipment industry is the backbone of shipbuilding. Ships need engines, propellers, pumps, valves, boilers, HVAC systems, switchboards, navigation systems, automation equipment, fire-safety equipment, and environmental systems. If these parts are imported from other countries, shipyards may face delays, higher costs, exchange-rate risks, and problems with delivery schedules. Korea reduced these risks by building a strong local supplier base around its major shipyards [12], [21].

The engine industry is a good example. In the beginning, Korea depended heavily on foreign engine technology. Hyundai entered marine engine production in the 1970s through licences from European firms. Later, it invested in its own technology and developed the HiMSEN engine [14]. This shows the Korean pattern: first learn from foreign technology, then improve it, and finally produce it locally. Table 1 represents a number of backward linkages sectors of shipbuilding. Also, the materials that industries supplied and the representative companies as example are given.

Table 1: Consolidated backward-linkage industries and representative Korean suppliers

Backward-linkage category	Main equipment or input	Representative Korean suppliers
Marine engines and propulsion	Large marine engines; low-speed engines; engine parts and services	Hyundai Engine Company; HD Hyundai Marine Engine; Hanwha Engine; STX Engine
Deck machinery, steering and thrusters	Marine cranes; windlasses; mooring winches; capstans; steering gear; transmission systems; side thrusters	OPCO (Oriental Precision & Engineering); D-I Industrial; Yoo Won M-Tech; Sekwang Marine Machineries
Marine pumps	Centrifugal, gear, submersible and general marine service pumps	Kyeongyang Pump; Gorio Pump & Marine System
Marine and industrial valves	Control valves; relief valves; engine valves; cryogenic and offshore valves	KORVAL; Samwoo Valve; OK Kwang Engineering (OKV)
Boilers, heat exchangers, HVAC and compressors	Marine boilers; heat exchangers; HVAC and refrigeration systems; air and gas compressors	Kangrim Heavy Industries; DongHwa Entec; HI AIR KOREA; Century; Coaire Screw Compressor
Environmental systems	Ballast water treatment systems; exhaust gas cleaning systems; scrubber and environmental equipment	Techcross; Panasia
Electrical and onboard systems	Marine lighting; power equipment; communication systems; motors; generators; switchboards	Daeyang Electric; HD Hyundai Electric
Steel and special materials	Ship plate; high-tensile steel; cryogenic steel; corrosion-resistant steel; offshore structural materials	POSCO; Hyundai Steel and other steel-processing suppliers

The table shows that Korea's supplier base is broad. It is not limited to steel. It includes machinery, electrical systems, environmental equipment, outfitting items, engines, and special materials. This wide supplier base helps shipyards control delivery schedules and solve technical problems faster.

5.3. Shipyard Integration and the Steel Supply

Shipbuilding uses a large amount of steel. For this reason, a stable supply of marine-grade steel is very important. Steel companies provide plates, rolled strips, I-beams, stainless steel, high-tensile plates, and special steel for LNG carriers and offshore structures [28]. The growth of POSCO and other Korean steelmakers gave shipyards a reliable local source of steel. This reduced dependence on imports and helped match steel delivery with shipyard production schedules.

The link between steel and shipbuilding also helped both sides learn. Korean steel companies developed special steel products for ships. These included cryogenic steel for LNG cargo systems, corrosion-resistant plates for chemical tankers, and extra-thick plates for offshore structures. This close relationship lowered supply risk and helped Korean shipyards compete on both price and delivery time [7].

5.4. Industrial Clustering

The backward linkages of the South Korean shipbuilding industry had a large economic impact outside the industry itself through the HCI drive of the 1970s. The HCI program also extended to the upstream supplier industries including steel, metals, machinery, petrochemicals, electronics and shipbuilding. The supported industries had strong positive spillovers to downstream industries which increased purchase of intermediate goods and invested more [23]. Targeted industries grew significantly faster than non-targeted ones, suggesting the success of targeting industries with large backward and forward linkages [23]. Despite early difficulties, the HCI program contributed to laying the foundation for many of South Korea's key sectors, such as steel, shipbuilding, machinery, electronics, and petrochemicals, as well as semiconductors and the automobile industry [24]. The initiative was based on the realisation that many sectors feeding output to HCI industries were upstream sectors closer to the raw materials end of the supply chain, providing a network effect to benefit many industrial sectors [29].

Figure 7: Backward-linkage base: Korea's marine equipment industry.

The economic effects were compounded by the emergence of industrial clusters. In South Korea, the shipbuilding industry formed strong industrial clusters due to national investments in world-class shipbuilding infrastructure, institutional capacity and specialised educational establishments, and the relentless efforts of shipbuilders and suppliers to constantly improve the production efficiency [14], [30]. This clustering resulted in a compact environment where shipbuilders and their suppliers could work together closely, share ideas and enjoy constant gains in efficiency and technology.Figure 7 presents the strong backward-linkage base of Korea's marine equipment industr, there are about 2,700 firms and employing around 73,000 workers. Domestic production capacity is high and the industry meets almost 90% of domestic demand for marine equipment. In 2022, marine equipment exports reached about USD 1.2 billion, with China holding a 57.7% share, the United States 29.3% and other markets 13.0%.

Some states have been formed as geographical clusterings to develop this shipbuilding sectors in South Korea. Shipbuilding production bases are located in Ulsan, Geoje, Busan, Mokpo and Changwon. All of these cities are near shipyards, steel mills, equipment makers, research labs, design firms and logistics companies. It also saves transportation time and cost. Analysis of the clustered example has shown lower transport costs for heavy inputs, faster troubleshooting between equipment makers and yards, concentration of vocational training programs [13]. The advantages of this cluster system can be:

- Faster movement of materials
- Lower transportation costs
- Quick troubleshooting between suppliers and shipyards
- Shared access to skilled labor, training centers, and universities
- Localized innovation and knowledge exchange

5.5. Skilled Workforce and Training Systems

Shipbuilding and its supplier industries need many skilled workers. These workers are needed for welding, block assembly, pipe fitting, engine installation, outfitting, electrical work, quality checks, and production planning. Korea built this workforce through maritime universities, vocational schools, and company training systems. These institutions supplied technicians and engineers for shipyards and supplier firms [15], [22].

Workforce training is still important because Korean yards are building more complex and low-emission ships. Workers now need skills in digital production, environmental systems, LNG technology, and smart-ship equipment. For this reason, training is not only a social issue. It is also part of Korea's backward-linkage strength [1], [3].

5.6. Technological Collaboration Between Supporting Industries and Shipyards

Technology sharing between shipyards and suppliers has helped Korea upgrade its shipbuilding industry. Electronics, machinery, engine, welding, automation, and software firms have supported smart monitoring systems, better propulsion, digital navigation, robotic welding, and improved production planning. These linkages helped Korea move from simpler ships to LNG carriers, large container ships, offshore structures, and smart ships [1], [14]. Technology protection is also important because shipbuilding knowledge has high economic value [31].

Production technology is also important. Korean shipbuilders now use simulation, digital models, digital twins, and computer-based production systems to plan block assembly, logistics, and production order [32]. These systems work well only when suppliers deliver parts on time and follow common standards. For this reason, supplier capability directly affects shipyard productivity.

5.7. Develop Smooth Supply Chain System

Modern shipbuilding uses modular and block-based production. This means that large parts of a ship are built separately and then joined together. Suppliers and subcontractors must deliver pipes, electrical panels, equipment, and outfitting modules according to strict shipyard standards. Pre-outfitting is very important in this system. It means installing many systems before the blocks are joined. This reduces crowding at later stages, lowers rework, shortens construction time, and improves quality.

Korean shipyards can build ships faster because many suppliers understand the technical standards, documents, classification rules, and schedules required by the yards. Studies on block assembly and outfitting show that productivity depends on coordination among design, production, logistics, and suppliers [32], [33]. The main lesson is simple: backward linkages are not only about supplying many materials. They are also about whether suppliers can support quick design changes and complex ship systems [26], [30].

6. Future Strategy, Direction and Development Goals

Korea's future shipbuilding strategy should build on its strength in complex and high-value ships. At the same time, Korea must keep improving the local supplier base. The global market is moving toward cleaner ships, alternative fuels, digital shipyards, and smart ship systems [1], [19], [34]. Korean shipbuilders already have strong positions in LNG carriers, very large container ships, oil tankers, offshore production units, naval vessels, and eco-friendly vessels. InvestKOREA reports that Korea won a large share of high-value and eco-friendly ship orders in 2022, including large LNG carrier orders [18].

Environmental rules are a major reason for change. IMO 2020 reduced the global sulphur limit for ship fuel oil from 3.50% to 0.50% outside emission control areas [35]. The 2023 IMO GHG Strategy also aims to reduce carbon intensity by at least 40% by 2030 and reach net-zero greenhouse gas emissions from international shipping by or around 2050 [36]. These rules will increase demand for alternative-fuel engines, fuel tanks, cryogenic materials, energy-management systems, scrubbers, ballast water treatment systems, and digital monitoring tools. Therefore, Korea should support local development of these parts instead of depending too much on imports.

Future policy should support both large shipyards and small and medium suppliers. Many small and medium firms hold special knowledge in equipment, parts, repair, software, and production support. They are very important for the whole shipbuilding system [19], [21]. Workforce renewal is also a key issue. Korea needs more skilled workers for welding, outfitting, electrical work, engineering, digital production, and green-ship technology. Training programmes, university-industry cooperation, safer workplaces, automation, and careful use of foreign workers can help reduce labour shortages. Finally, Korea should continue the coordination that helped the industry grow in the past. Shipyards, suppliers, banks, research institutes, universities, and government agencies need to work together. This cooperation will be important as the industry faces cleaner technology, digital production, and global supply-chain uncertainty.

7. Conclusion

Overall, Korea's shipbuilding history shows that shipyards alone were not enough. Backward linkages are a main reason for South Korea's success in shipbuilding. Korea succeeded because shipyards grew together with steel, machinery, engines, marine equipment, finance, technology learning, and government support. These backward linkages helped firms enter the industry, survive crises, move into high-value ships, and stay competitive.

These supporting industries helped Korean shipyards in many ways. They reduced dependence on imported parts. They helped shipyards avoid delays. They lowered production costs. They also helped Korea build more advanced and high-value ships.

The Korean case shows that shipbuilding needs a strong industrial system. Shipyards alone are not enough. Government support helped the industry at the beginning. Industrial clusters helped shipyards and suppliers work closely. Marine equipment firms reduced the need for foreign parts. Domestic steel suppliers made material supply more secure. Technology sharing helped Korea move into complex ships such as LNG carriers and smart ships.

The world shipbuilding industry is now moving toward cleaner ships and digital production. In this new stage, Korea's backward linkages will remain very important. If Korea keeps improving its suppliers, workers, technology, and coordination, it can continue to be one of the leading shipbuilding countries in the world.

References

[1] D. Lee, "Influences behind the development of South Korea's shipbuilding industry from the 1960s to the 2000s," Marine Policy, vol. 167, p. 106251, 2024, doi: 10.1016/j.marpol.2024.106251.

[2] S. K. Tan, "State support and competitiveness of industry: Case of shipbuilding industry in Korea," WILAYAH: The International Journal of East Asian Studies, vol. 9, no. 1, pp. 48–60, 2020.

[3] L. Brun and S. Frederick, "Korea and the Shipbuilding Global Value Chain," Global Value Chains Center. Accessed: May 26, 2026. [Online]. Available: https://www.globalvaluechains.org/cggclisting/chapter-4-korea-and-the-shipbuilding-global-value-chain/

[4] OECD, Peer Review of the Korean Shipbuilding Industry 2026. in Reviews of Shipbuilding Economies. OECD Publishing, 2026. doi: 10.1787/c19e0105-en.

[5] Allied Market Research, "Shipbuilding Market Size, Share, Trends | Analysis Report - 2030," Allied Market Research. Accessed: May 26, 2026. [Online]. Available: https://www.alliedmarketresearch.com/shipbuilding-market-A08511

[6] UNCTAD, "Review of Maritime Transport 2024 | UN Trade and Development (UNCTAD)." Accessed: May 26, 2026. [Online]. Available: https://unctad.org/publication/review-maritime-transport-2024

[7] K. Shin and P. S. Ciccantell, "The Steel and Shipbuilding Industries of South Korea: Rising East Asia and Globalization," JWSR, pp. 167–192, Aug. 2009, doi: 10.5195/jwsr.2009.316.

[8] Z. Meng, H. J. Cho, and K. Gore, "Tracing the steel supply chain of the shipbuilding industry," International Council on Clean Transportation. Accessed: May 26, 2026. [Online]. Available: https://theicct.org/publication/tracing-the-steel-supply-chain-of-the-shipbuilding-industry-sept24/

[9] UNCTAD, “Review of Maritime Transport 2025: Staying the course in turbulent waters | UN Trade and Development (UNCTAD).” Accessed: May 26, 2026. [Online]. Available: https://unctad.org/publication/review-maritime-transport-2025

[10] S. K. Tan, “State Support and Competitiveness of Industry: Case of Shipbuilding Industry in Korea,” IJEAS, vol. 9, no. 1, pp. 48–60, Dec. 2020, doi: 10.22452/IJEAS.vol9no1.4.

[11] H. Hyundai, “History | HD Hyundai,” Our Heritage. Accessed: May 26, 2026. [Online]. Available: https://www.hd.com/en/history/contents

[12] R. Hassink and D. Shin, “South Korea’s shipbuilding industry: From a couple of Cathedrals in the desert to an innovative cluster,” Asian Journal of Technology Innovation, vol. 13, no. 2, pp. 133–155, Jan. 2005, doi: 10.1080/19761597.2005.9668611.

[13] D.-H. Shin and R. Hassink, “Cluster Life Cycles: The Case of the Shipbuilding Industry Cluster in South Korea,” Regional Studies, vol. 45, no. 10, pp. 1387–1402, Nov. 2011, doi: 10.1080/00343404.2011.579594.

[14] E. Sohn, Jaeyong Song, and 장성용, “Technological Catching-up and Latecomer Strategy: A Case Study of the Asian Shipbuilding Industry,” Seoul Journal of Business, vol. 15, no. 2, pp. 25–57, 2009, doi: 10.35152/SNUSJB.2009.15.2.002.

[15] H.-Y. Jeong, “Does the Forty Year’s Success Myth of the Korea Shipbuilding Industry Come to an End?,” JEPF, vol. 3, no. 2, p. 151, Mar. 2017, doi: 10.22158/jepf.v3n2p151.

[16] M. Hess, I. F. Pavić, S. Kos, and D. Brčić, “Global shipbuilding activities in the modern maritime market environment,” Pomorstvo (Online), vol. 34, no. 2, pp. 270–281, Dec. 2020, doi: 10.31217/p.34.2.8.

[17] S. Gordon, “2024 Shipping Market Review,” Clarksons Research. Accessed: May 26, 2026. [Online]. Available: https://insights.clarksons.net/2024-shipping-market-review/

[18] Invest Korea, “Shipbuilding and Marine.” Accessed: May 26, 2026. [Online]. Available: https://www.investkorea.org/ik-en/cntnts/i-320/web.do

[19] S. Park and P. Kim, “Operational Performance Evaluation of Korean Ship Parts Manufacturing Industry Using Dynamic Network SBM Model,” Sustainability, vol. 13, no. 23, p. 13127, Nov. 2021, doi: 10.3390/su132313127.

[20] L. Yu, J. Wei, W. Jiang, and T. Wang, “Impact of Global Value Chain Participation on the Performance of Shipbuilding Enterprises,” FBEM, vol. 12, no. 2, pp. 218–224, Dec. 2023, doi: 10.54097/fbem.v12i2.14884.

[21] K. A. Hossain, “Analysis of Important Steering Factors Which Give Success to Global Shipbuilding Leaders,” RAPSCI, vol. 4, no. 5, Apr. 2018, doi: 10.19080/RAPSCI.2018.04.555650.

[22] S.-J. Kwak, S.-H. Yoo, and J.-I. Chang, “The role of the maritime industry in the Korean national economy: an input–output analysis,” Marine Policy, vol. 29, no. 4, pp. 371–383, Jul. 2005, doi: 10.1016/j.marpol.2004.06.004.

[23] R. Cherif and F. Hasanov, “The Return of the Policy That Shall Not Be Named:

Principles of Industrial Policy," IMF. Accessed: May 26, 2026. [Online]. Available: https://www.imf.org/en/publications/wp/issues/2019/03/26/the-return-of-the-policy-that-shall-not-be-named-principles-of-industrial-policy-46710

[24] J. Felipe, "Asias Industrial Transformation: The Role of Manufacturing and Global Value Chains (Part 1," Asian Development Bank, Manila, Philippines, ADB Economics Working Paper Series, Jul. 2018. doi: 10.22617/WPS189457-2.

[25] N. M. Trang, "The Middle Income Trap: A Case Study of Korea and Lesson for Vietnam," PaM, vol. 37, no. 2, Jun. 2021, doi: 10.25073/2588-1116/vnupam.4240.

[26] D. A. D. Moura and R. C. Botter, "Toyota production system - one example to shipbuilding industry," Ind. Jour. Manag. & Prod., vol. 8, no. 3, pp. 874–897, 2017, doi: 10.14807/ijmp.v8i3.626.

[27] E. M. Graham, "Reforming Korea's industrial conglomerates," Peterson Institute Press: All Books, 2003.

[28] S. Won and S.-G. Choi, "Development of the Korean Iron and Steel Industry," IFAC Proceedings Volumes, vol. 36, no. 24, pp. 1–8, Oct. 2003, doi: 10.1016/S1474-6670(17)37595-X.

[29] N. Lane, "Manufacturing Revolutions: Industrial Policy and Industrialization in South Korea," The Quarterly Journal of Economics, vol. 140, no. 3, pp. 1683–1741, Jul. 2025, doi: 10.1093/qje/qjaf025.

[30] M. A. Mendes Primo and F. DuBois, "Technological Capabilities of Brazilian Shipbuilding Suppliers," Journal of Technology Management & Innovation, vol. 7, no. 2, pp. 39–51, Jul. 2012, doi: 10.4067/S0718-27242012000200004.

[31] Y. Chun, "An Analysis on the Industrial Technology Leakage Cases in South Korea," IJEBO, vol. 1, no. 3, p. 27, 2013, doi: 10.11648/j.ijebo.20130103.11.

[32] D. Jeong, D. Kim, T. Choi, and Y. Seo, "A Process-Based Modeling Method for Describing Production Processes of Ship Block Assembly Planning," Processes, vol. 8, no. 7, p. 880, Jul. 2020, doi: 10.3390/pr8070880.

[33] J. H. Choi and J. H. Woo, "Algorithm development for the spool installation sequence of outfitting works in offshore structure," Journal of Marine Science and Technology, vol. 26, no. 2, pp. 470–485, Jun. 2021, doi: 10.1007/s00773-020-00751-4.

[34] M. Mindur, "THE DEVELOPMENT OF SEA TRANSPORT IN SOUTH KOREA BETWEEN 2002-2017," SJSUT.ST, vol. 105, pp. 183–199, Dec. 2019, doi: 10.20858/sjsutst.2019.105.15.

[35] IMO, "IMO 2020 – cutting sulphur oxide emissions." Accessed: May 26, 2026. [Online]. Available: https://www.imo.org/en/mediacentre/hottopics/pages/sulphur-2020.aspx

[36] IMO, "2023 IMO Strategy on Reduction of GHG Emissions from Ships." Accessed: May 26, 2026. [Online]. Available: https://www.imo.org/en/ourwork/environment/pages/2023-imo-strategy-on-reduction-of-ghg-emissions-from-ships.aspx

ISSN : 2959-6602

Journal of Engineering and Technology (JET) - Vol : 04 (2026)
ISSN : 2959-6602
Bangladesh
Maritime University

Numerical Investigation of Airflow and Heat Removal Performance in the Engine Room Ventilation System of a Bangladeshi Inland Ship

Md Abul Hasnat Alvi [a], Mahmud Hasan [b], Md Mashud Karim [c*]

Abstract:

This paper presents a CFD simulation to analyze the ventilation system within a ship's engine room. The engine room geometry is designed in Rhino, and STAR-CCM+ is used for mesh generation, computations, and visualization of results. In this CFD analysis, the SIMPLE algorithm is used to couple velocity and pressure, and the standard k-ε (SKE) turbulence model is applied here to analyze the result. The study determines airflow and temperature distribution inside an engine room. Various ventilation designs are explored, and airflow rates measured in air changes per hour (number of times the entire engine room air is changed per hour) are evaluated through CFD simulations to determine the optimal air supply necessary for both efficient engine room cooling and adequate combustion air for the engines. By comparing average temperatures at different airflow rates, the study identifies the most effective air exchange rate. Findings suggest that ventilation systems are highly affected by the number of inlet ducts, duct positioning, air changes per hour, and duct size. Increasing the number of inlet ducts directly reduces the engine room temperature.Reducing the inlet duct radius increases inlet air velocity, which reduces the inside temperature by around 17K. Besides that, higher ACH reduces domain temperature, but it has a fixed operating value, which is 18-24, and values other than that have less cooling efficiency. The position of the inlet duct has a significant effect on engine room temperature.Inside temperature reduces by about 3.64K and outlet temperature reduces by around 5K when the vertical position of the inlet duct is on the lower side.When the outlet radius increases from 60 to 100 cm, the outlet temperature drops by 8.2 K. The results satisfied the ISO ventilation standard and had a good agreement with the data of a physically available marine vessel.

Article History :
Received 30 March 2026
Accepted 30 May 2026
Published 30 June 2026

Keywords: Computational Fluid Dynamics; Temperature distribution; Heat transfer; Air changes per hour; Standard k-ε turbulence model; Forced ventilation; Inlet duct geometry; Inland waterway vessel; ISO 8861.

[a]*Department of Naval Architecture and Marine Engineering, Bangladesh University of Engineering and Technology, Dhaka-1200, Bangladesh. Email:mdabulhasnatalvi2001@gmail.com*

[b]*Department of Naval Architecture and Marine Engineering, Bangladesh University of Engineering and Technology, Dhaka-1200, Bangladesh. Email:mahmudgdby1718@gmail.com*

[c]*Department of Naval Architecture and Marine Engineering, Bangladesh University of Engineering and Technology, Dhaka-1200, Bangladesh. Email: mmkarim@name.buet.ac.bd*

[*]*Corresponding Author: Email: mmkarim@name.buet.ac.bd*

1. Introduction:

The engine room in the ship holds great significance because it contains the main propulsion engine, auxiliary engine, boilers, pumps, various tanks, steam pipes, and discharges huge amounts of heat into the engine room, thus making the temperature in the engine room high. A proper engine room ventilation provides enough air for combustion of engines, cooling the room, and maintaining the proper environment for crew and equipment.

A few kinds of research have been done on the CFD analysis of engine room ventilation. Horng et al. [1] developed a new ventilation system design process that allows design engineers to predict the air quantity deliveries at the outlets. They predict air quantity deliveries of a 4662 TEU container ship and compare with measured values. Tasdemir et al. [2] report the flow of fluid and temperature distribution in an engine room of a tugboat and compare it with numerical data. They showed the temperature distribution of the engine room and various engine room planes. Jian et al. [3] used a bulldozer cab model and obtained the temperature field and velocity field for side wall and roof air supply through the RNG-epsilon two-equation turbulence model and SIMPLE algorithm, and found that side wall air supply gives better results. Doğrul et al. [4] investigated the effect of different HVAC positions.They used the standard k-epsilon model. The results were shown in path-lines, velocity, and temperature distribution in the room. The performances were shown for three different positions of heating units. Zhai et al. [5], [6] describe different turbulence models inside enclosed areas. In the paper, they talk about recent CFD turbulence model advancements and talk about different models such as RANS (Reynolds-Averaged Navier–Stokes) models (under this, there are Standard k–ε, RNG k–ε, Low-Re k–ε, Low-Re k–ε, k–ω), LES (Large Eddy Simulation), Hybrid models, and New or modified models.They found that RNG k-ε works great in general indoor environments, and if detailed turbulence is required, then LES does better. Other models do well for a specific case. For engine room ventilation analysis, Chen et al. [7] use six different outlet arrangements for optimization of engine room ventilation and found that outlets at the top are most reasonable. They also analyzed the effect of supplied air temperature and velocity on the engine room environment. Niu et al. [8] did a numerical simulation of 320,000 VLCC vessels' engine rooms and found summer temperature on different planes above the baseline. Shankar et al. [9] examined the effect of forced convection on a cold attic, which is seen in cold countries. In the attic, the air cavity is above the insulation. Besides this, the effect of air permeability was taken care of. The result was shown based on the temperature contour and the velocity contour. Serbanescu et al. [10] highlight the need for enough air circulation for combustion and for quality breathing air. Mihai et al. [11] discuss rules, regulations, maker requirements, design, and construction challenges of engine room ventilation design. Newton et al. [12] assessed the ventilation of the engine room and compared the results with three different weather conditions. They also compare the result with practical data. After that, they change the inlet position for optimization of the ventilation. They also change the ducted outlet to decrease the engine room temperature. Park et al. [13] take an LNG carrier's engine room, where, due to the complicated structure, welding fumes couldn't move. To optimize this, a ventilation fan is used where the CFD solution shows the optimal position of fans, which gives the lowest mean age air. They also analyze the particles that have sizes and properties of welding fumes and find out that they should be studied separately from the air. Pérez et al. [14] analyzed heat and air movement of an engine room, and by coordinating with the crew's working schedule, they made an optimal ventilation set-up and optimizedthe crew's working time, where they can work without overheating. Alizadeh [15] used the CFD method to reduce heat concentration by using a different ventilation arrangement system. They optimized the ventilation system and found that if a proper ventilation arrangement is not used, heat is accumulated and increases the average temperature of the engine room. Zani et al [16] analyze the engine room ventilation system of an inland bulk carrier. They analyze the effect of different air flow rates and different inlet arrangement systems. Besides that, they showed high inlet duct radius reduces inlet air velocity, hence removing less heat. They also showed the standard criteria of engine room temperature and combustion air. Orosa et al. [17] developed a 3D CFD model to analyze the hottest place inside the engine room. Using the analysis, they developed a model for maximum working time in the engine room based on air change per hour and inside temperature conditions. Besides that, they developed a model for analyzing minimum working time for crew members to release the heat.Ramos et al [18] analyzed the natural ventilation of an underground transformer substation and found that airflows are reversed at the outlet. Besides that, hot air gets accumulated at the top.

The goal of this study is to determine the optimal ventilation configuration for the engine room of a Bangladeshi inland cargo vessel by systematically investigating the effects of inlet duct radius, outlet duct radius, air changes per hour, and inlet vertical positioning through CFD simulations, with the aim of achieving ISO 8861 compliance while minimizing energy consumption.

2. Rules and Standards for Ventilation:

2.1 IMO and Classification Society requirements:

For the design of engine room ventilation systems, the rules and recommendations established by the International Maritime Organization (IMO) and Classification Societies must be met, as these regulations are directly related to the safety of the vessel and the lives of those on board. For heat balance calculations and other ventilation system design requirements, Classification Societies recommend ISO standard 8861 [19]. The principal regulatory requirements for engine room ventilation systems, according to IMO and Classification Society rules, are as follows [19]:

- The ventilation system shall be designed and constructed to ensure the required operating conditions for machinery and boiler systems at full power under all weather conditions.
- The engine room ventilation system shall remain isolated from ventilation systems serving other compartments on board the vessel.
- The ventilation arrangement shall be capable of removing smoke from the engine room during fire emergencies, and reversible fans may be used as part of the smoke extraction system.

- Emergency or reversible ventilation fans shall be connected to an emergency power supply to maintain ventilation during power failure conditions.
- The ventilation arrangement and air distribution within the engine room shall be designed to prevent the accumulation of oil vapors during normal operating conditions.

2.2 ISO requirements:

The amount of air in the engine room shall be such that it not only fulfills the need for air in combustion but also the amount of air needed for removing heat in the engine room. Rules and regulations according to ISO [19]:

- Maximum difference of temperature between supply and exhaust air:12.5 K
- Outside ambient temperature: 308 K
- Specific heat capacity of air: 1.01kJ/ (Kg K)
- Air density (considered at + 308 K, 70% RH, and 101.3 kPa): 1.13 kg/m³

Besides this, ISO mentions the formula for calculating the amount of combustion air needed for diesel engines and the amount of air needed for removing radiated heat inside the engine room. If there is an absence of data in the case of calculating heat radiation, standard figures provided by ISO can be utilized.

2.3 Engine Room and airflow arrangements:

Caterpillar [20] mentions several engine room ventilation systems. There are mainly four types. It also provides routing factors for different arrangements. In type-1, the supplied air is passed at the floor level, in between the engine and the exhaust part, which is at the top corner, and the routing factor is 1. Type-02 is the same as type-01; the difference is that air is sent under the floor plate. The routing factor for type-01 and type-02 is 1. In type-3, it requires 50% more airflow than types 1 and 2, meaning the routing factor is 1.5. Here, the inlet duct is positioned far away from the engine and exhaust. On the other hand, type-4 is the least effective design. Its routing factor is 2.5. It directs discharged air to the air inlet of the turbocharger of the engine. Among these four, type-01 offers the best air flow and the best cooling efficiency. It is the most suitable option for the arrangement of engine room ventilation.

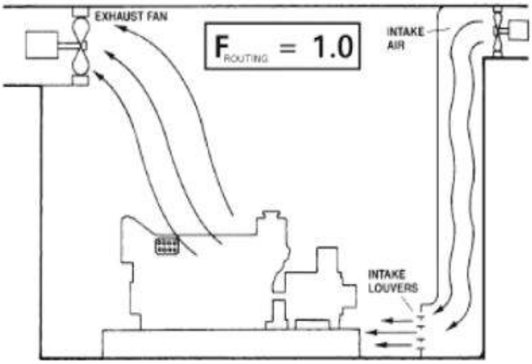

Figure 1: Ventilation arrangement Type-01

For multiple engines, the air flow should be between engines and from one room side to another. The following figures are shown on how to arrange the air flow in the engine room.

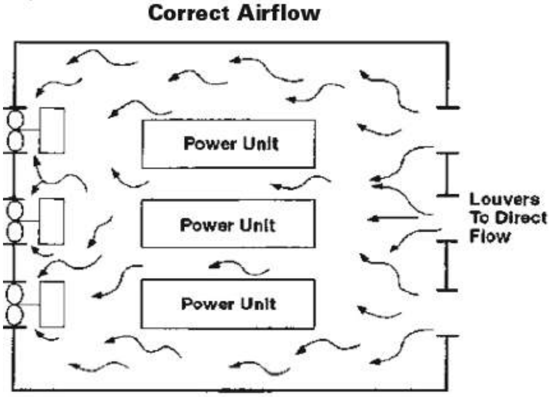

Figure 2: Example of a correct air flow model in a multiple-engine installation

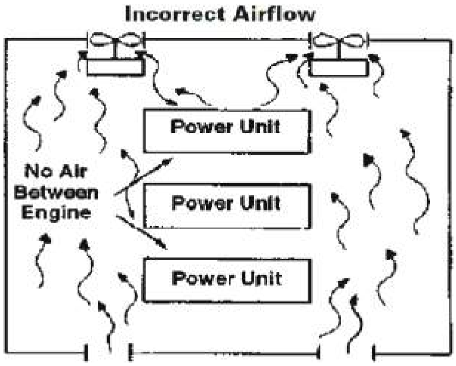

Figure 3: Example of an incorrect airflow model in a multiple-engine installation

3. Governing Equations:

The conservation of mass equation is

$$\frac{\partial\rho}{\partial t} + \nabla.\left(\rho\vec{V}\right) = 0 \quad (1)$$

And the conservation of momentum equation is

$$\rho\left(\frac{\partial}{\partial t}\vec{V} + \vec{V}.\nabla\vec{V}\right) = \nabla P + \mu\nabla^2\vec{V} + \vec{S} \quad (2)$$

And the conservation of energy equation is

$$\rho\frac{\partial T}{\partial t} + \rho\vec{V}.\left(T\vec{V}\right) = \nabla.\left(\frac{K}{C_p}\nabla T\right) + S_T \quad (3)$$

These equations form a set of coupled, nonlinear partial differential equations. It is not possible to solve these equations analytically for most engineering problems. However, it is possible to obtain approximate computer-based solutions to the governing equations for a variety of engineering problems. The standard k-ε (SKE) model is used for modelling turbulent flow to show path lines, velocity, and temperature fields.

Turbulence kinetic energy governing equation,

$$\frac{\partial(\rho k)}{\partial t} + \frac{\partial(\rho u k)}{\partial x} = \frac{\partial}{\partial x}\left[\mu + \frac{\mu_t}{Pr_k}\right]\frac{\partial k}{\partial x} + \mu_t G - \rho\varepsilon + S_{k,P} \quad (4)$$

Equation of its distribution

$$\frac{\partial(\rho\varepsilon)}{\partial t} + \frac{\partial(\rho u\varepsilon)}{\partial x} = \frac{\partial}{\partial x}\left[\mu + \frac{\mu_T}{Pr_\varepsilon}\right]\frac{\partial\varepsilon}{\partial x} + \frac{\varepsilon}{k}\left[C_1\mu_T G - C_2\rho\varepsilon\right] + S_{\varepsilon,P} \quad (5)$$

Where,

P^r = Prandtl numbers for kinetic energy

S = User-defined source term

C^1 & C^2 = Empirical model constants

Turbulence kinetic energy (G) is calculated by

$$G = \left(\frac{\partial u_i}{\partial x_j} + \frac{\partial u_j}{\partial x_i}\right)\frac{\partial u_i}{\partial x_j} - \frac{1}{\rho^2}\frac{\partial\rho}{\partial x_j}\frac{\partial\rho}{\partial x_i} - \frac{2}{3}\left(\frac{\rho k}{\mu_T} + \frac{\partial u_i}{\partial x_i}\right)\frac{\partial u_j}{\partial x_j} \quad (6)$$

4. Computational Domain Generations and Boundary Conditions:

A 3Dmodel of the engine room was developed using Rhino3D software. The engine room contains two engines, each with a power output of 750 kW, along with two generators, each generating 170 kW. These are considered the primary sources of heat emission, while other potential heat sources are regarded as negligible. The ventilation system includes six inlets—two positioned in front of each engine and one in front of each generator. The inlet radii are not fixed and vary from 0.40 to 0.10 m, and results are also shown for each radius. The outlet radii are also not fixed, and results are shown for 0.60,0.80,0.90 and 1m. The number of inlets is also varied to see the effect, and the positions of the inlets are also varied. The isometric view of the engine room is shown in Figure 4.

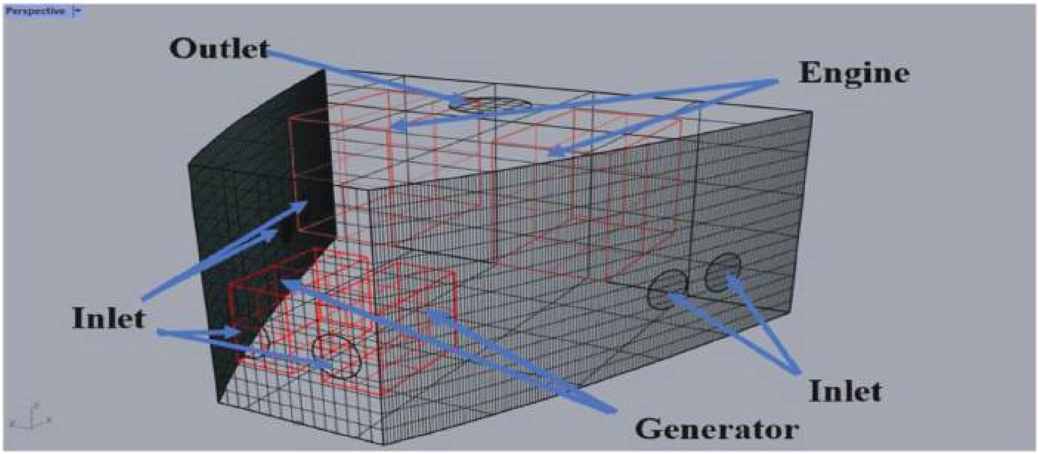

Figure 4: Isometric view of the engine room.

Wall boundary conditions and thermal boundary conditions are applied to solve this CFD simulation.

Table 1: Wall boundary conditions

Parameter	Condition
Velocity inlet(m/s)	Depends on the air change per hour
Outlet gauge pressure (atm)	1 atm
Inlet gauge pressure (atm)	1 atm
Inlet temperature	308 K

Thermal boundary conditions are shown in Table 2.

Table 2: Thermal boundary conditions

Parameter	Condition
Engine heat source	41.6268 X 2 kW
Generator heat source	17 X 2 kW

5. Results

A total of 36 steady-state CFD simulations were conducted by varying four independent parameters: inlet duct radius (10– 40 cm), air change per hour (ACH; 8–24), inlet vertical position, and outlet duct radius (60–100 cm). The engine room volume is 233.92 m^3; therefore, one ACH corresponds to a volumetric flow rate of 233.92 m^3/h. Ambient inlet temperature was fixed at 308 K (35 °C) in all cases, consistent with the ISO 8861:1998 standard. The engine heat flux applied to each main engine surface was 41.63 kW and 17.00 kW for each generator.

5.1 Effect of Number of Inlets and Generator Presence

Before parametric studies were conducted, three fundamental system configurations were compared at ACH = 18 (flow rate 4210.56 m^3/h) to establish the relative importance of generator heat load and inlet distribution. The results are summarized in Table 5.1 and Figure 5.1.

Operating with only two inlets and no generators yields an average inside temperature of 382.37 K and an average outlet temperature of 404.28 K, both far above the ISO limit. Activating both generators raises these values by approximately 8 K to 390.43 K and 411.47 K, respectively, confirming that the generators represent a significant secondary heat load that must be explicitly accounted for in ventilation design. Increasing the number of inlets from 2 to 6 while retaining the generators dramatically reduces the average inside temperature to 322.94 K and the outlet temperature to 326.70 K, a reduction of 67.49 K relative to the two-inlet, generator-present case. This result demonstrates that distributing the supply air through multiple inlets directed at individual heat sources is the single most consequential design decision in engine room ventilation. All subsequent parametric studies were therefore conducted with six inlets and both generators active.

Table 5.1: Effect of inlet count and generator presence on engine room temperatures (ACH = 18, inlet r = 20 cm).

Configurations	No. of Inlets	Generator	Avg. Inside Temp. (K)	Avg. Outlet Temp. (K)
2 Inlets with no Generator	2	Absent	382.37	404.28
2 Inlets with Generator	2	Present	390.43	411.47
6 Inlets with Generator	6	Present	322.94	326.7

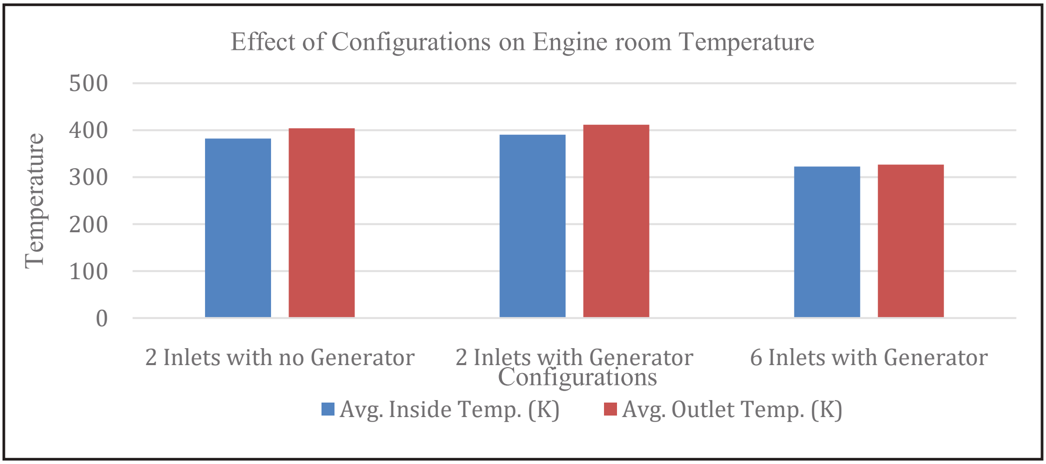

Figure 5.1: Effect of number of inlets and generator presence on engine room temperatures.

5.2 Effect of Inlet Duct Radius

Four inlet duct radii— 10, 20, 30, and 40 cm—were tested at a fixed ACH(ACH (Air Changes per Hour) means the number of times the total air volume inside the engine room is completely replaced with fresh air within one hour) of 18 (flow rate 4210.56 m^3/h) with six inlets and generators active. Because the total volumetric flow rate was held constant, smaller inlets produce higher inlet jet velocity, which increases turbulent mixing and convective heat transfer near the heat-generating surfaces.

Figure 5.2 shows the air temperature gradient contour for the inlet radius of 30 cm. The first figure is for the front view of the generator section, the second one for the front view of the engine section, the third one for the left side view of the generator and engine section, and the fourth one for the left side view of the engine room mid-section. This result is for the 18 times air change per hour, which is equivalent to an air flow rate of 4210.56 m3/hr. It is observed that the maximum temperature of the engine room is 456.13K at the location (9300 mm from aft perpendicular, 1975 mm from center line, 4253 mm from bottom), and the minimum temperature is 307.77K at the location (4422 mm from forward perpendicular, 777 mm from center line, 1513 mm from bottom).

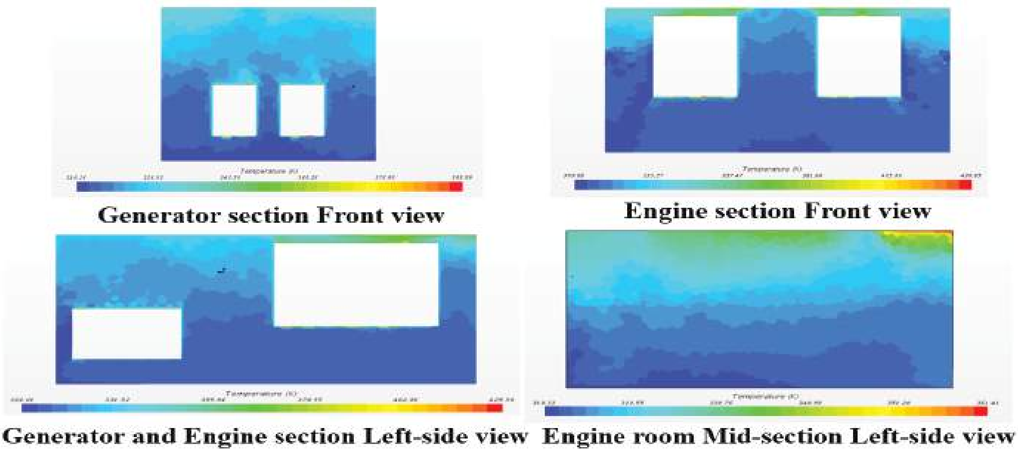

Figure 5.2.1: Air temperature gradient contour for the inlet radius of 30 cm

Figure 5.2.2 summarizes the key thermal outcomes. Reducing the inlet radius from 40 cm to 10 cm decreased the average engine room temperature from 326.55 K to 309.21 K (−4.7%) and the average outlet temperature from 330.60 K to 310.29 K. The maximum local hot-spot temperature also fell dramatically from 1159.2 K (concentrated near the engine surface in the 40 cm case) to 374.35 K in the 10 cm case, indicating that higher-velocity, focused jets are significantly more effective at breaking down thermal stratification in the immediate vicinity of heat sources. All outlet temperatures satisfy the ISO 8861:1998 criterion of $T_n^{oe} \leq T_a^{mb} + 12.5$ K = 320.5 K for the smallest two radii; the 30 cm and 40 cm configurations marginally exceed this limit at 18 ACH, suggesting that larger-radius inlets require proportionally higher flow rates to achieve compliance.

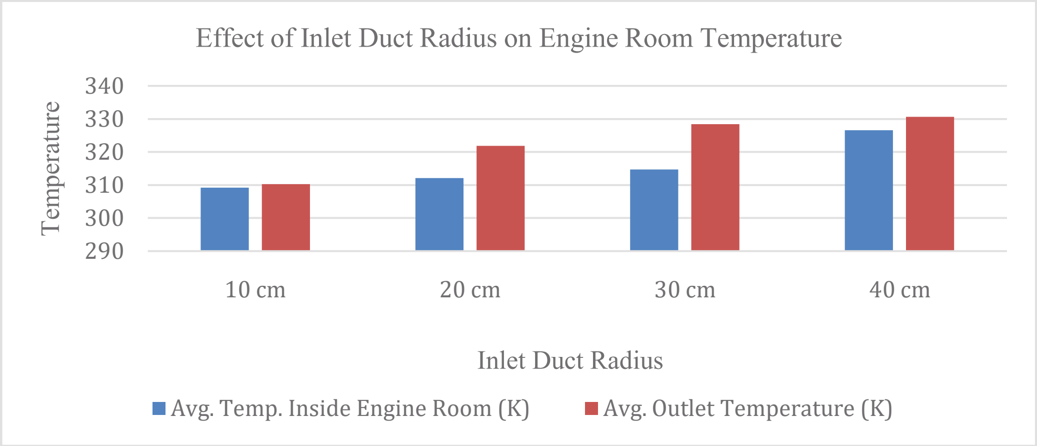

Figure 5.2.2: Effect of inlet duct radius on average inside and outlet temperature of the engine room (ACH = 18).

5.3 Effect of Air Change Per Hour (ACH)

The ACH was varied from 8 to 24 in increments of 2 for each of the four inlet radii. As shown in Figure 5.3(a), the average engine room temperature and in Figure 5.3(b) the average outlet temperature decrease monotonically with increasing ACH. However, the rate of reduction diminishes at higher ACH values, consistent with a logarithmic cooling relationship.

For the 40 cm inlet, the inside temperature drops from 347.37 K (8 ACH) to 322.94 K (24 ACH), a reduction of 24.43 K. For the 10 cm inlet, the corresponding reduction is only 1.08 K (309.83 K → 308.75 K), because the smaller duct already achieves near-optimal cooling through high jet velocity and the marginal benefit of additional airflow is limited. This observation has practical significance: for installations where small-radius ducts are structurally feasible, the blower power requirement for equivalent cooling is substantially reduced compared with large-radius, low-velocity systems.

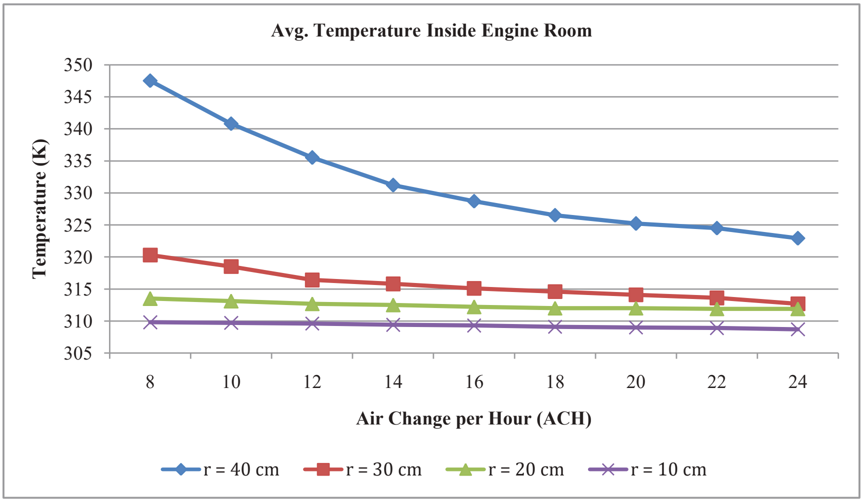

Figure 5.3(a): Effect of air change per hour (ACH) on average inside temperatures for four inlet duct radii.

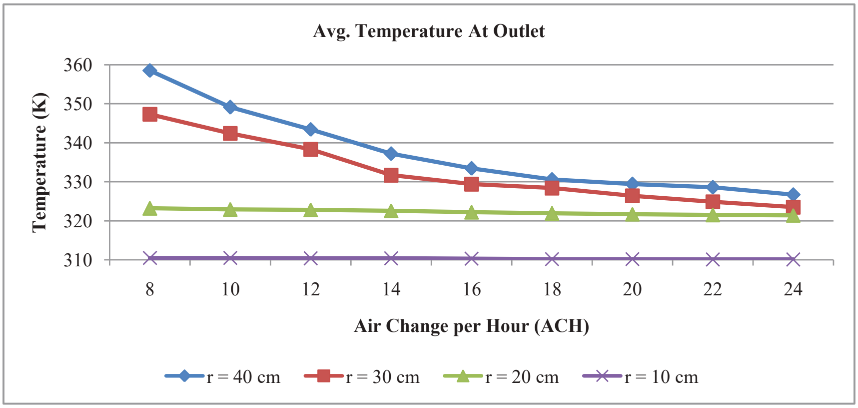

Figure 5.3(b): Effect of air change per hour (ACH) on average outlet temperatures for four inlet duct radii.

5.4 Effect of Inlet Duct Vertical Position

Figure 5.4.1 shows the air temperature gradient contour for a lower inlet position (the inlet radius of 20 cm) with 21640 mm longitudinal distance from the midship section and 1000 mm height from the bottom. This result is for the 20 times air change per hour, which is equivalent to an air flow rate of 4678.4 m3/hr. It is observed that the maximum temperature of the engine room is 360.8K at the location (9330 mm from aft perpendicular, 1972 mm from center line, 4255 mm from bottom), and the minimum temperature is 307.06K at the location (4420 mm from forward perpendicular, 775 mm from center line, 1510 mm from bottom). The average outlet temperature of the engine room is 316.7K, and the average inside temperature of the engine room is 308.16K.

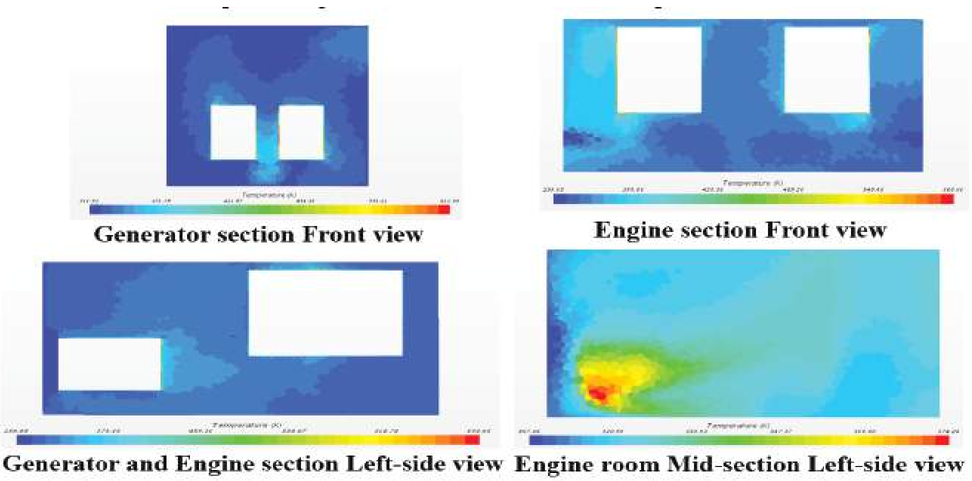

Figure 5.4.1: The air temperature gradient contour for the lower inlet position (the inlet radius of 20 cm)

Two vertical positions were examined for the 20 cm radius inlet at ACH = 20 (flow rate 4678.4 m^3/h): (a) the upper position at 3000 mm from the floor, which approximates the engine body height and represents the configuration used in the majority of simulations, and (b) the lower position at 1000 mm from the floor, placed at approximately one-quarter of the engine room height. Both cases used an identical inlet velocity (1.72 m/s).

Figure 5.4.2 shows that the lower inlet position reduces the average inside temperature from 312.04 K to 308.40 K and the average outlet temperature from 321.70 K to 316.70 K. This improvement reflects better alignment of the supply jet with the primary heat-generating zones near the engine base and crankcase, allowing cooler air to sweep horizontally across the heat sources before rising by natural convection. The result is consistent with Caterpillar Type-1 ventilation guidance, which places air supply ducts at floor level between engines as the optimal arrangement.

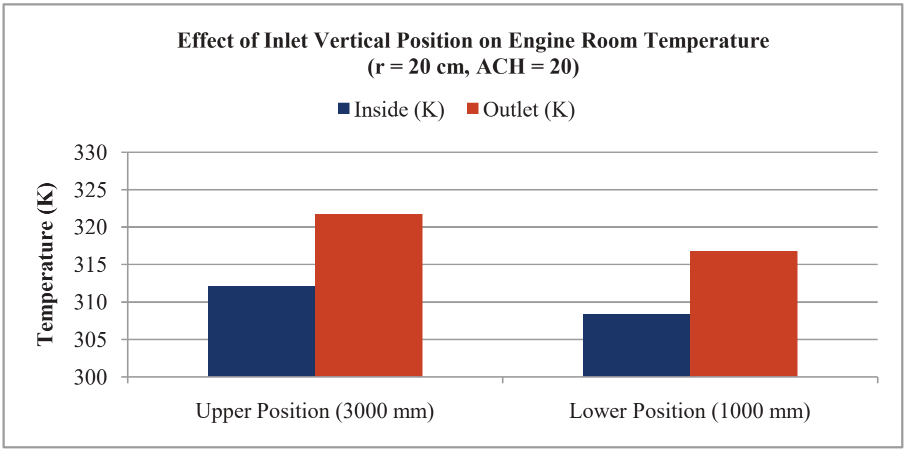

Figure 5.4.2: Comparison of upper and lower inlet positions

5.5 Effect of Outlet Duct Radius

Five outlet duct radii were examined—60, 70, 80, 90, and 100 cm—at ACH = 20 with inlet radius fixed at 10 cm and inlet velocity 1.7235 m/s. Because the volumetric supply flow rate was kept constant, the outlet cross-section size affects only the exhaust velocity and the local pressure distribution near the ceiling; it does not change the net mass flux through the room.

Figure 5.5.1 shows the air temperature gradient contour for an 80 cm outlet radius. The first figure is for the front view of the generator section, the second one for the front view of the engine section, the third one for the left side view of the generator and engine section, and the fourth one for the left side view of the engine room mid-section. This result is for 20 air changes per hour, corresponding to an airflow rate of 4678.4 m3/hr. It is observed that the maximum temperature of the engine room is 350.82K at the location (9320 mm from aft perpendicular, 1975 mm from center line, 4250 mm from bottom). The minimum temperature is 308.5K at the location (4410 mm from forward perpendicular, 777 mm from center line, 1514 mm from bottom). The average outlet temperature of the engine room is 320.7K, and the average inside temperature of the engine room is 309.4K.

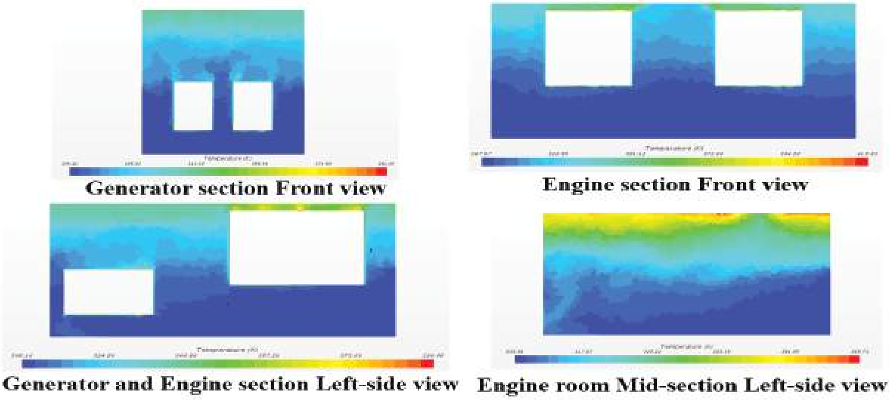

Figure 5.5.1: Air temperature gradient contour for the outlet radius of 80 cm

Figure 5.5.2 shows that increasing the outlet radius from 60 to 100 cm reduces the average outlet temperature from 324.8 K to 316.6 K (−8.2 K) while the average inside temperature decreases only marginally from 309.9 K to 309.1 K. A larger outlet area lowers the exhaust velocity, which reduces the suction zone near the outlet and promotes more uniform upward convective flow throughout the engine room ceiling region. Practical design should balance the thermal benefit of a larger outlet against structural and weight penalties aboard shallow-draft inland vessels.

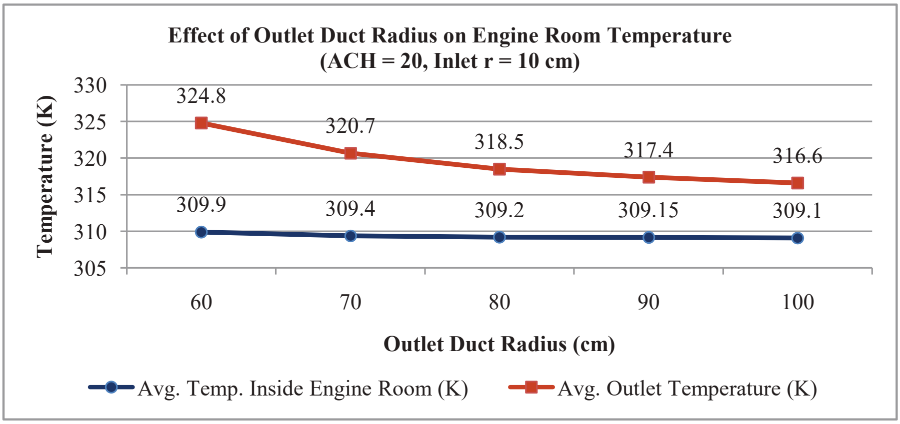

Figure 5.5.2: Effect of outlet duct radius on average inside and outlet temperature of the engine room (ACH = 20).

5.6 Model Validation Against Real-World Data

The predicted average outlet temperatures across all simulated outlet radius cases ranged from 309.1 K to 324.8 K. These values were compared against engine room high-temperature measurements recorded by Meghna Ship Builder and Dockyard Ltd. for eight Bangladeshi inland vessels of varying dimensions and power configurations (Figure 5.6). The recorded field ranges were 308–328 K, and the simulated range lies fully within this envelope. The close agreement validates the modelling approach, including geometry, boundary conditions, turbulence model choice, and meshing strategy for practical engine room ventilation design of inland ships operating on Bangladeshi waterways.

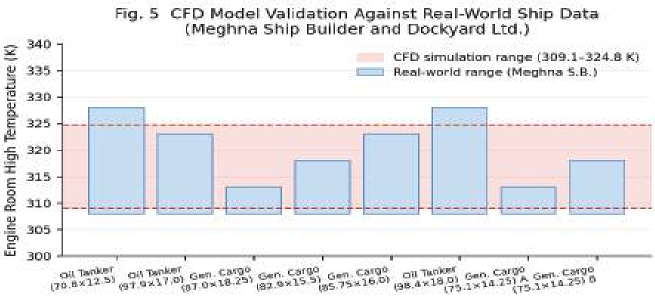

Figure 5.6: Validation of CFD outlet temperature predictions (dashed band) against high-temperature data recorded aboard inland vessels by Meghna Ship Builder and Dockyard Ltd. (blue bars represent recorded temperature ranges).

 ISSN : 2959-6602

6. Conclusions

A systematic CFD investigation of engine room ventilation was conducted for a representative inland cargo vessel of Bangladesh (LOA 71.3 m, engine room volume 233.92 m^3) equipped with two 750 kW main engines and two 170 kW generators. Simulations were performed using the finite volume solver STAR-CCM+ with the Standard k-ε turbulence model and SIMPLE algorithm. The following conclusions are drawn:

- Increasing the number of inlets from 2 to 6 reduces the average inside temperature by 67.49 K when generators are present, demonstrating that targeted, distributed air supply is far more effective than a centralized arrangement.
- Inlet duct radius is the dominant design variable: reducing the inlet radius from 40 cm to 10 cm at a fixed ACH of 18 lowered the average engine room temperature by 17.34 K and eliminated extreme hot-spot temperatures of over 1100 K observed with low-velocity, large-radius inlets.
- Higher ACH consistently reduces engine room temperature, but the benefit exhibits diminishing returns; a practical operating range of 18–24 ACH is recommended as a balance between cooling effectiveness and blower energy consumption.
- Lower inlet vertical placement (h = 1000 mm from the floor) is thermally superior to upper placement (h = 3000 mm), reducing the average inside temperature by 3.64 K and the average outlet temperature by 5.0 K at the same flow rate. This result supports Caterpillar Type-1 ventilation, which positions supply ducts at floor level between engines.
- Larger outlet duct radius improves heat dissipation at the exhaust; increasing the outlet radius from 60 to 100 cm reduced the average outlet temperature by 8.2 K. Outlet radius primarily affects the exhaust flow uniformity rather than the bulk room temperature.
- All simulated cases with inlet radii ≤20 cm comply with the ISO 8861:1998 requirement that the outlet temperature must not exceed the ambient temperature by more than 12.5 K (i.e., $T_n^{oe} \leq 320.5$ K for $T_a^{mb} = 308$ K).
- Simulated outlet temperatures (309.1–324.8 K) are in excellent agreement with field measurements from Meghna Ship Builder and Dockyard Ltd. (308–328 K), validating the CFD model for practical application.

Future work should incorporate transient simulations to capture engine warm-up and load-change scenarios, include radiation heat transfer from hot surfaces, and extend validation to a wider variety of inland vessel types. Smart ventilation control integrating real-time temperature sensors with variable-speed blowers is also recommended as a practical pathway to reducing shipboard energy consumption while maintaining thermal compliance.

Acknowledgement:

Authors acknowledge Bangladesh University of Engineering and Technology for all computational and financial support.

References:

[1] W.-K. Horng and H.-J. Shaw. "A study on the integrated design of engine room ventilation." Journal of Marine Science and Technology, vol. 25, no. 1, pp. 8, 2017.

[2] C. Taşdemir and S. Bayraktar. "CFD analysis of ventilation system for an engine room." Dec. 2016.

[3] Z. Jian, R. Hongjuan and L. Yiping. "Simulation research on airflow field of bulldozer cab." Int. J. Mech. Eng. Appl., vol. 4, no. 4, pp. 152–155, Jul. 2016.

[4] A. Doğrul, Y. H. Özdemir and S. Bayraktar. "Modelling of a HVAC unit in a room for performance analysis." Yildiz Technical University, Dept. of Naval Architecture & Marine Engineering, Istanbul, Turkey.

[5] Z. Zhang, W. Zhang, Z. J. Zhai and Q. Y. Chen. "Evaluation of various turbulence models in predicting air flow and turbulence in enclosed environments by CFD: Part 1-comparison with experimental data from literature." HVAC&R Research, vol. 13, no. 6, pp. 871-886, 2007.

[6] Z. Zhang, W. Zhang, Z. J. Zhai and Q. Y. Chen. "Evaluation of various turbulence models in predicting air flow and turbulence in enclosed environments by CFD: Part 2-comparison with experimental data from literature." HVAC&R Research, vol. 13, no. 6, pp. 871-886, 2007.

[7] J. Chen, J. Xu, L. Wang, X. Chen and Y. Gong. "Numerical analysis of ventilation for ship E/R with CFD method." Int. J. Perform. Eng., vol. 14, no. 3, pp. 531, Mar. 2018.

[8] A. Niu, M Guo, J Wang, M Chen, G Jin and S Wang."Numerical simulation of thermal environment in 320,000 tons VLCC engine room." IOP Conference Series: Earth and Environmental Science, vol. 687, pp. 012106, 2021.

[9] V. Shankar, A. Bengtson, V. Fransson and C.-E. Hagentoft. "CFD analysis of heat transfer in ventilated attics." in Proc.International Conference of Fluid Flow, Heat and Mass Transfer (FFHMT'17), Aug. 2017, pp. 180.

[10] I. Serbanescu. "Consideration regarding maritime ship engine room ventilation system." International Journal of Innovative Research in Engineering & Management, 2016.

[11] V. Mihai, L. Rusu and A. Presura. "Ventilation of engine rooms in diesel engine ships." Analele Univ. Dunărea Jos Din Galați Fasc. XI Construcţii Nav. Ann. Dunărea Jos Galati Fascicle XI Shipbuild., vol. 43, pp. 69–78, Nov. 2020.

[12] W. Newton, M. Lewis, D. Carswell, N. P. Lavery, B. Evans, D. Bould and J. Sienz. "Investigating the thermal profile of a marine vessel engine room through simulation with field measurements." Applied Thermal Engineering, vol. 73, no. 1, pp. 1360-1370, 2014.

[13] S. Park, M. Kim, J. Seo and S. Choi. "Numerical study on the internal ventilation of the engine room of a ship under construction." Alexandria Engineering Journal, vol. 100, pp. 232–245, Aug. 2024.

[14] J. A. Pérez, J. A. Oros and Á. M. Costa. "Energetic optimization of the ventilation system in modern ships." Applied Thermal Engineering, vol. 108, pp. 816–823, Sep. 2016.

[15] E. Alizadeh, A. Maleki and A. Mohamadi. "An investigation of the effect of ventilation inlet and outlet arrangement on heat concentration in a ship engine room." Engineering, Technology & Applied Science Research, vol. 7, no. 5, pp. 1996-2004,2017.

[16] M. R. Zani, M. T. Hossain, M. Rahman, M. M. Rahaman and N. M. G. Zakaria. "Computational fluid dynamics analysis of engine room ventilation of a bulk carrier plying in the inland waterways of Bangladesh." in Proc. MARTEC 2022 – Int. Conf. Marine Technol., BUET, Dhaka, Bangladesh, Dec. 2022, pp. 299–304.

[17] J. A. Orosa, A. M Costa and J.A. Perez. "A new modelling procedure of the engine room ventilation system for work risk prevention and energy saving." Proceedings of the Institution of Mechanical Engineers, Part M: Journal of Engineering for the Maritime Environment, vol. 231, no. 4, pp. 863-870, 2017.

[18] J. C. Ramos, M. Beiza, J. Gastelurrutia, A. Rivas, R. Anton, G. S. Larraona and I. de Miguel. "Numerical modelling of the natural ventilation of underground transformer substations." Applied Thermal Engineering, vol. 51, no. 1-2, pp. 852-863, 2013.

[19] ISO. "8861: 1998, Shipbuilding-Engine room ventilation in diesel engine ships design requirements and basis of calculation." British Standard,1998.

[20] Caterpillar. "CAT Engine Room Ventilation Guide." 2015.

Bangladesh
Maritime University

Computational Fluid Dynamics Investigation of Biofouling Surface Roughness Effects on Performance of a Modified Batch-Type Savonius Marine Current Turbine

Shuaib Al Rashid [a]*, Md. Main Uddin[b], Md. Abadat Hossain[c]

Abstract:

The gradual breakdown of the hydrodynamic effectiveness of marine current turbines due to biofouling (organism colonies) found surrounding the turbine in freshwater and/or saltwater environments creates a significant challenge for all applications. This paper describes the results of a Computational Fluid Dynamics (CFD) analysis of the influence of biofouling-induced roughness on the hydraulic performance of a Modified Bach-type Savonius marine current turbine. Five different levels of roughness caused by biofouling, from the smoothest (ks= 0mm) to the extreme (ks= 5 mm) were analyzed through the 5 levels of tip speed ratios from 0.2 to 1.0 using the k-ω SST (Shear Stress Transport) turbulence model as the turbulence model. Overall, the CFD results indicate that biofouling has a significant negative impact on the performance of a mechanical device; specifically, the maximum C_p reduced by 44.87% under an extreme level of biofouling. The results of this research will provide researchers and offshore Marine Current Turbine Designers/operators with an estimated level of "acceptable" performance degradation along with the time frame between complete maintenance and overhaul in order to conduct timely maintenance and maximize offshore marine current turbine operations in the coastal area of Bangladesh.

Article History :
Received 30 March 2026
Accepted 27 May 2026
Published 30 June 2026

Keywords: Savonius turbine; Marine current turbine; Biofouling; Surface roughness; Tip speed ratio; Power coefficient

[a]*Department of Mechanical Engineering, Chittagong University of Engineering & Technology, Chattogram-4349, Bangladesh Email: shuaib.alrashid@gmail.com*
[b]*Department of Mechanical Engineering, Chittagong University of Engineering & Technology, Chattogram-4349, Bangladesh Email: main23489@gmail.com*
[c]*Department of Natural Science, Port City International University, South Khulshi, Chattogram-4202, Bangladesh Email: abadat26@gmail.com*
[*]*Corresponding Author: Email: shuaib.alrashid@gmail.com*

1. Introduction

The global move toward clean, renewable energy has resulted in unprecedented investment in marine renewable technologies, which include tidal currents, wave energy, and salinity gradients among numerous others. Ocean energy resources, therefore, represent one of the most predictable and energy dense renewable resource bases on the planet. Per the International Energy Agency (IEA), non-fossil sources will be scaled to significantly larger capacities in order to achieve net-zero targets by 2050; marine energy will play an increasingly strategic role in powering coastal and island systems [1,14]. Tidal and ocean current turbines have become exceptionally appealing within this mix of potential generation technologies because, unlike solar or wind resources, tidal flows are governed by predictable lunar-gravitational cycles; thus, power generation from tidal turbines occurs with substantially less intermittency than that of solar or wind resources and is both reliable and well-established [15]. The combination of this predictability and the remarkably high energy density of seawater means that tidal turbine power generation requires a significantly lower rotor footprint than either wind or river turbine technologies.

The Savonius rotor has become increasingly popular recently due to research into using the rotor as a cost and low-maintenance method of extracting energy from the ocean waves or currents for shallow depth and/or low velocity, where a ship would not be effective at deploying energy extraction devices to extract energy from tidal/wave action or for offshore installations. The Savonius rotor is an S-shape, two-blade, vertical-axis design and thus operates without the need for a yaw control system, as it can self-start from a current velocity of 0.5m/sec and allow bi-directional or omnidirectional flow [16]. The materials required to produce a Savonius rotor can be easily obtained at low capital costs, using materials available on/developed on-site. The Savonius rotor's potential for off-grid and/or distributed solutions of energy for small island and coastal communities in developing countries makes it an ideal solution to provide these communities with power. The overall power output from the Savonius rotor will vary based on its design but will be lower than from a horizontal axis rotor; the average range of power coefficient from horizontal axis rotor designs is between 0.15+ to 0.35+ depending upon design configuration and therefore, ongoing CFD and experimental studies remain in place to improve the overall hydrodynamic characteristics of the Savonius rotor through optimization of blade shape, integration of deflectors and tuning aspect ratio [17].

One of the main challenges caused by biofouling (the accumulation of organisms, such as bacteria, microalgae, macroalgae, barnacles, and mussels) on submerged surfaces during marine turbine deployment, which is often overlooked until it is too late is its operational impact on turbine performance. Biofouling starts within hours of submersing a turbine, by creating a conditioning film that allows for the formation of a bacterial biofilm (typically within a matter of days) and then macro-fouling organisms (barnacles and mussels) within weeks to months [4,18]. This gradual process can significantly change the hydrodynamic surface characteristics of turbine blades. For example, the introduction of biofouling increases the sand equivalent roughness height (ks) values associated with a given surface from 0.03 mm for light slime (a thin layer of bacteria) to >3 mm for heavy barnacle biofouling [4]. The resultant increase in hydrodynamic roughness causes an increase in the boundary layer thickness on the turbine blade, which causes the skin friction coefficient of the turbine to increase, resulting in early flow separation, increased drag on the turbine blade(s), and reduced energy produced by the turbine. Using CFD methods, researchers have shown that heavy biofouling can cause a reduction in the power coefficient of horizontal-axis tidal turbines by as much as 13% compared to design tip-speed ratios (TSR) and even larger percent reductions when operating at tip-speed ratios greater than those for design [5,19].

While there are numerous studies on how marine biofouling impacts ships and Horizontal Axis Tidal Turbines (HATT), there has been limited research completed utilizing CFD that has looked into how the surface roughness caused by marine biofouling affects the performance of Savonius marine current turbines (SMCTs). There is a significant gap in knowledge on this topic. The flow physics of the Savonius rotor (e.g., how vortex shedding, flow separation, inter-blade jetting, and an extremely wide range of tip speed ratios (TSRs) occur) is considerably different than that of horizontally-axis designs, so it may be influenced by surface roughness perturbations differently. This will therefore be an extremely important consideration for any SMCT deployed within the rapidly biofouling tropical coasts of the world (e.g., the coast of Bangladesh's Bay of Bengal region), which will have higher water temperatures, greatly increased nutrient loading, and thus, increased rates of colonization by biofouling organisms compared to the rest of the world [20].

This research fills the gap mentioned above by performing a systematic investigation using CFD to explore how biofouling (the accumulation of micro-biological organisms) affects the hydrodynamic performance of Savonius marine current turbines because of: (i) development and validation of a 2D Unsteady Reynolds-Averaged Navier-Stokes (URANS) CFD turbine model with clean (newly manufactured) surfaces; (ii) using a modified wall-function surface roughness model to represent four different biofouling conditions (biomass accumulation); (iii) quantifying how much C_p and moment coefficient (C_m) degrade when subjected to different flux rates for a range of tip speed ratios (TSR), resulting in four possible biofouling conditions; and (iv) identifying the most vulnerable TSR for each type of biofouling condition. The paper is structured as follows: Section 2 provides a description of the turbine geometry and computational domain; Section 3 outlines the numerical method with the surface roughness description; Section 4 describes and analyzes the numerical results; Section 5 states conclusions and Section 6 outlines future work.

2. Geometrical Setup

2.1 Modified Bach-Type Savonius Rotor

This investigation examines anewly modified (Bach-type) Savonius rotor (S-shape). The blades possess characteristic proportions based on [6]. The various geometric parameters are displayed in Table 1 below. The blades exhibit a 135° arc with a 0.42d offset of the center of the rotor, creating an asymmetric blade overlap that gives rise to the differential pressure mechanism responsible for generating the torque.

ISSN : 2959-6602

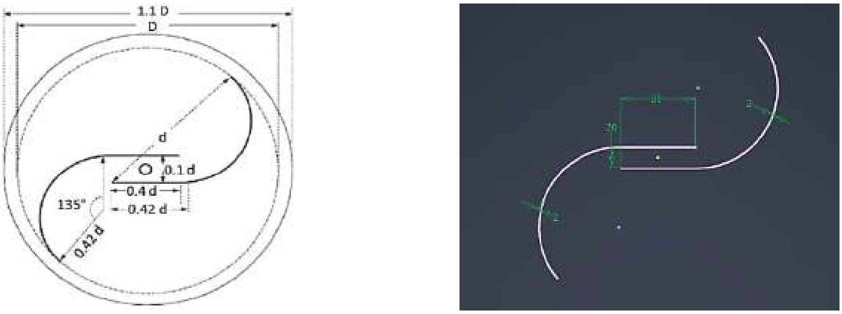

(a) (b)

Figure 1: Schematic of Modified Bach-type Savonius rotor geometry of (a) extracted dimension from [7] (b) this study

Parameter	Formula	Value
Blade diameter	d	200 mm
Rotor diameter	D	200 mm
Outer shroud diameter	1.1D	220 mm
Blade arc radius	0.42d	84 mm
Shaft offset	0.42d	84 mm
Shaft diameter	0.1d	20 mm
Gap width	0.4d	80 mm
Blade height	H	200 mm
Aspect ratio	H/D	1.0
Blade angle	-	135°

Table 1: Modified Bach-type Savonius rotor geometric parameters (d = 200 mm)

2.2 Computational Domain

For this analysis, we have divided our computational domain into two separate fluid zones: one that contains the cylindrical, rotating inner zone that encompasses the turbine rotor and another that is a rectangular, static outer zone that represents the far-field flow region. The physical dimensions of the computational domain were established according to established CFD guidelines for turbomachine simulations and are based on reducing the effects of blockage and ensuring that the flow is fully developed before it reaches the turbine rotor.

Specifically, the upstream length of the computational domain was set to 1500 mm so that the flow would develop sufficiently before reaching the turbine rotor; and the downstream length of the computational domain was set to 2000 mm such that the turbine's wake would be captured before it interacts with the computational domain’s outlet boundaries. The width of the computational domain was set to 700 mm on each side of the rotor. The height of the computational domain was defined as 500 mm which provides a 150 mm gap between the top of the turbine blades and the top of the computational domain.In addition, the cylindrical, rotating zone is defined as having a diameter of 440 mm so that there is sufficient space between the tips of the turbine blades and the boundary of the rotating zone to limit mesh distortion during the analysis.

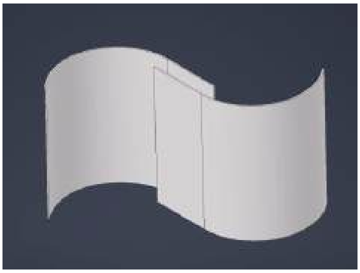

(a) Blade Geometry

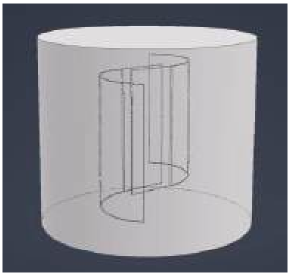

(b) Rotating Zone

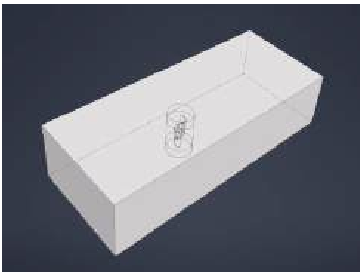

(c) Computational Domain

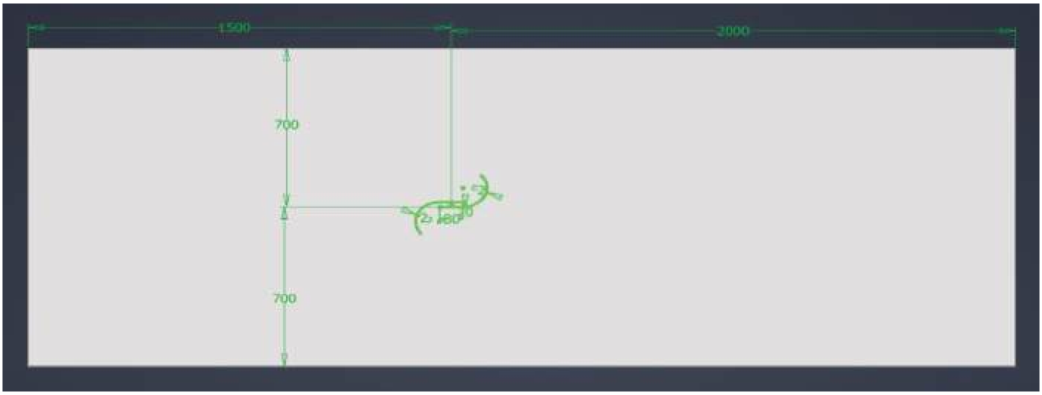

Figure 2: Computational geometry of Modified Bach-type Savonius marine current turbine.

3. Numerical Methodology

3.1 Mesh Generation

The tetrahedral unstructured mesh was generated using ANSYS Meshing, and inflation layers were provided for all blade surfaces to resolve the boundary layer effectively. The rotating zone mesh will have a finer mesh than the stationary zone meshes due to the complex flow physics that are occurring near the rotor blades located in the rotating zone; on the other hand, the mesh size of the outer stationary zone will be coarser than that of the rotating zone, thus reducing computational costs while still producing acceptable results.

All blades have a 5-layer inflation layer with a first-layer height of 0.3 mm and a growth rate of 1.2.The near-wall mesh was designed to maintain y+ values within the range of approximately 30-100, which is suitable for the wall-function-based k-ω SST turbulence model adopted in the present study. Since scalable wall functions were employed, resolving the viscous sublayer directly was not required. This approach significantly reduced computational cost while still providing acceptable accuracy for predicting flow separation and near-wall behavior around the Savonius rotor.Table 2 presents comparisons of the mesh refinement levels and is part of the mesh independence study as performed.

Table 2: Mesh independence study parameters and results

Mesh Parameter	Coarse Mesh	Fine Mesh
Total elements	779,525	
Blade surface element	6 mm	3 mm
Inflation layers	5	10
First layer height	0.3 mm	0.1 mm
Rotating zone element	15 mm	6 mm
Orthogonal quality	0.202	0.197
Max skewness	0.798	0.783
C_p difference (%)	Baseline	2.1

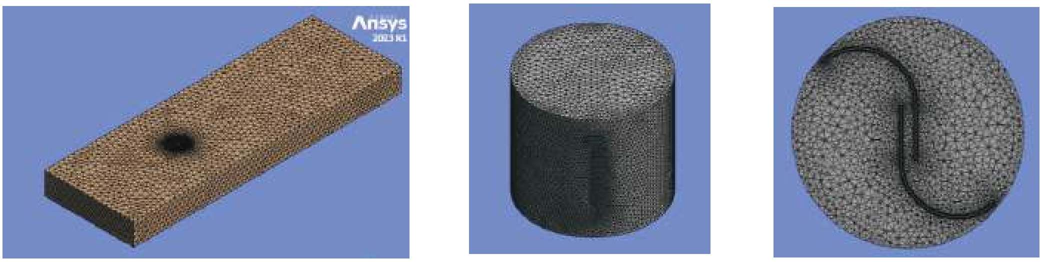

(a) (b) (c)

Figure 3: Computational mesh of (a) overall domain mesh (b) rotating zone mesh (c) blade surface mesh with inflation layers.

3.2 Turbulence Model and Solver Settings

The k-ω SST turbulence model was chosen as it is well known for being able to accurately compute the flow separation, adverse pressure gradients and near wall behavior that is encountered in rotating machinery [8]. The two-equation turbulence model captures the benefits of the k-ω model near the wall region and the k-ε model in the free stream region, providing an accurate prediction of the details of the complex flow fields found around Savonius turbines.

Table 3: CFD solver settings and numerical parameters

Parameter	Setting
Solver type	Pressure-based
Simulation type	Transient (unsteady)
Turbulence model	k-ω SST
Coupling Method	SIMPLE
Gradient scheme	Least Squares Cell
Pressure discretization	Second Order
Momentum discretization	Second Order Upwind
Turbulence discretization	Second Order Upwind
Time step size	0.004 s
Max iterations/time step	15
Convergence criterion	1×10^{-3}
Working fluid	Seawater
Inlet velocity	1.0 m/s
Roughness	$C_s = 0.5$

Complete solver settings used in this study presented as Table 3 solve for mass conservation and momentum; governing equations defined by the Navier-Stokes equation set were solved using SIMPLE algorithm (i.e. pressure-velocity coupling), applying second-order schemes for space discretization.Although the SIMPLE algorithm is commonly used for steady-state simulations, it has also been widely adopted for transient rotating machinery simulations due to its numerical stability and satisfactory pressure–velocity coupling performance at moderate time-step sizes. In the present study, the selected time-step size and convergence criteria ensured stable transient solutions throughout the simulations.

3.3 Boundary Conditions

Table 4 provides further details about the boundary conditions used in the computational domain. The inlet boundary was given a uniform velocity of 1.0 m/s, which is indicative of moderate tidal stream velocities found in the coastal areas of Bangladesh. The outlet was assigned a condition of zero-gauge pressure; that is, there was no hydrostatic pressure acting on the outlet wall. All solid surfaces (i.e., turbine blades and walls of the domain) were treated as no-slip walls.

Table 4: Boundary conditions applied to the computational domain

Boundary	Type	Condition
Inlet	Velocity Inlet	V = 1.0 m/s, normal to boundary
Outlet	Pressure Outlet	Gauge pressure = 0 Pa
Side/Top/Bottom walls	Wall	No-slip condition
Blade surfaces	Wall (No-slip)	Roughness height ks
Rotating zone	Fluid Zone	Prescribed angular velocity ω (rad/s)
Interface	Mesh Interface	One-to-one sliding interface

3.4 Biofouling Roughness Modelling

A standard roughness model in ANSYS Fluent has been applied to determine the biofouling effect on the turbine blade wall boundaries via an equivalent sand grain roughness height (ks). This model has been validated against experimental results from rough-wall turbulent-flow experiments and is consistent with the previous CFD algorithms used in marine biofouling studies [4,5].

The five cases of roughness were established based on published data on biofouling impacts in tropical marine environments [9,4]. The data sets for each case are shown in Table 5; specifically, the data are based on the following hydraulic specifications of the blade, from smooth and clean (hydraulically smooth) blade to extreme biofouled condition representative of a long-term, unmonitored condition.

A rough surface's constant of roughened (Cs = 0.5) was used in all cases; this means that when utilizing a wall roughness (used as an approximation to a smooth surface), the wall must possess sufficient dimensions such that ks+ > 70 in order for fully rough conditions to be developed by turbulence (this was verified via all simulations).In the present study, biofouling roughness was assumed to be uniformly distributed over the blade surface for simplification. However, actual marine biofouling is often non-uniform depending on local flow conditions and exposure duration.

Table 5. Biofouling roughness cases simulated in this study

Case	Fouling Condition	ks (mm)	Description
1	Smooth (clean)	0.00	Newly installed blade, no fouling
2	Light fouling	0.05	Algae biofilm, early colonization
3	Medium fouling	0.50	Early barnacle settlement
4	Heavy fouling	2.00	Dense barnacle coverage
5	Extreme fouling	5.00	Thick biofouling crust, long-term exposure

3.5 Turbine Performance Parameters

The turbine performance was evaluated using dimensionless coefficients as defined below. The Tip Speed Ratio (TSR) relates the blade tip velocity to the free-stream current velocity:

$$TSR = \lambda = \omega R / V\infty \qquad (1)$$

where ω is the angular velocity (rad/s), R is the rotor radius (m), and V∞ is the free-stream velocity (m/s).

The Cm quantifies the torque generated by the turbine:

$$C_m = T / (0.5\, \rho\, V\infty^2\, A\, R) \qquad (2)$$

where T is the net torque (N•m), ρ is the fluid density (kg/m³), A = D × H is the projected frontal area of the rotor (m²), and R is the rotor radius (m).

The Cp represents the fraction of available kinetic energy extracted by the turbine:

$$C_p = C_m \times TSR = P / (0.5\, \rho\, V\infty^3\, A) \qquad (3)$$

where P is the power produced by the turbine (W)

The C_d characterizes the resistance force acting on the rotor in the flow direction:

$$C_d = F_d / (0.5\ \rho\ V\infty^2\ A) \quad (4)$$

where Fd indicates the drag force acting on the turbine in the flow direction (N)

The simulated TSR values and corresponding angular velocities are presented in Table 6. The torque and drag values were time-averaged over the last two complete rotations of each simulation to obtain cycle-averaged performance coefficients.

Table 6. Simulated TSR values and corresponding angular velocities (V∞ = 1.0 m/s, R = 0.1 m)

TSR	ω (rad/s)	RPM	Application
0.2	2.0	19.1	Low-speed coastal current
0.4	4.0	38.2	Moderate current condition
0.6	6.0	57.3	Typical operating condition
0.8	8.0	76.4	Near-optimal condition
1.0	10.0	95.5	High-speed operation

4. Results and Discussion

4.1 Model Validation

Before conducting the parametric biofouling study using the CFD model, the parameters for a smooth blade were validated by comparing published experimental and numerical data for Savonius turbines to the calculated values of Cp (power coefficient at a given [TSR]) vs. TSR for a range of TSR values. There is good agreement between these calculations and published experimental or numerical data.

The limitations of the data published by [6] show that the computed power coefficient at the various test conditions did not exceed a maximum deviation of 10.7% when compared with the data from other authors. However, within the range of 0.4 – 1.0, the maximum deviation for these authors was 15%. The data were thus similar enough to allow us to apply them in validating the CFD results produced in this study.

The deviation between the present results and previous studies may be due to differences in rotor geometry, CFD setup and testing conditions. The referenced studies used different blade configurations, aspect ratios and overlap ratios, which can affect the predicted Cp values. Variations in mesh quality, turbulence modelling and boundary conditions may also contribute to the differences. In addition, some reference results were obtained experimentally, where measurement uncertainties and flow fluctuations are unavoidable. However, the overall Cp–TSR trend and optimal TSR show good agreement with published literature, indicating acceptable validation of the present CFD model.

Table 7: C_p results against TSR values for previous studies and current study (without roughness)

TSR	Akwa et al. (2012)	Modi & Fernando (1989)	Kamoji et al. (2009)	Grönman et al. (2021)	Present Study (CFD)
0.2	0.05	0.06	0.04	0.07	0.067
0.4	0.12	0.14	0.10	0.15	0.166
0.6	0.18	0.20	0.16	0.21	0.220
0.8	0.20	0.22	0.19	0.24	0.263
1.0	0.17	0.19	0.18	0.21	0.224
1.2	0.10	0.12	0.11	0.13	0.128

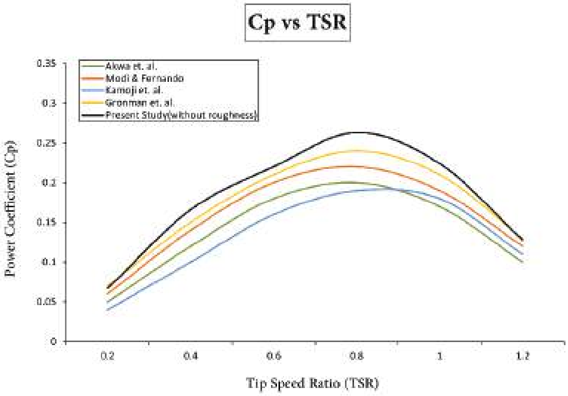

Figure 4: Validation of CFD model: Cp vs. TSR comparison with literature data

4.2 Baseline Performance (Smooth Blade)

Performance characteristics of the modified Bach-typeSavonius rotor (ks =0) are established first, establishing reference (baseline) case to compare all other cases to. Figure 5 is included; it shows the Cp vs. TSR curve for the clean blade condition. The power coefficient increases as TSR increases from a value of 0.2 to a maximum power coefficient, $C_{p,max}$ = 0.263 when TSR = 0.8, then begins to decrease as TSR continues to increase; this is consistent with the known characteristics of Savonius-type turbines [3,10,11].

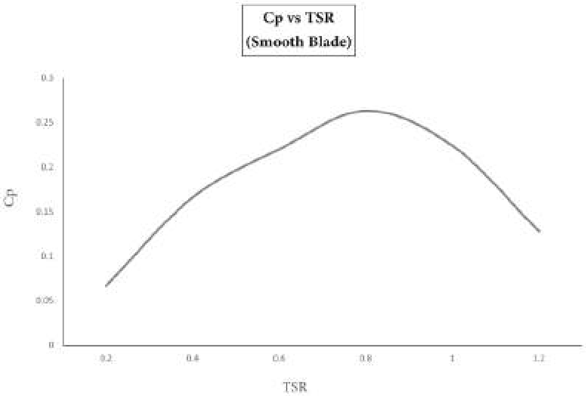

Figure 5: Power coefficient (Cp) versus Tip Speed Ratio (TSR) for smooth blade condition

The trend of the torque coefficient mirrors that of the torque coefficient with the largest value of Cm = 0.329 observed at a TSR of 0.8. Overall, these baseline results adhere to published values found in the literature for Modified Bach-type Savonius rotors with the maximum deviation of 10.7% occurring at TSR = 0.4 and being within the acceptable threshold required to confirm the validity of CFD results for rotating machinery to date [3,6,10,11].

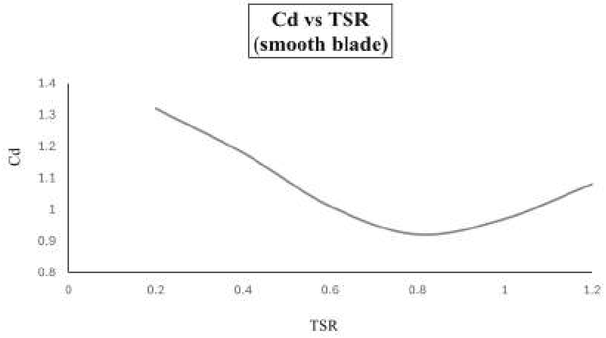

Figure 6: Drag coefficient (Cd) versus Tip Speed Ratio (TSR) for smooth blade condition

Figure 6 presents the variation of drag coefficient (Cd) with TSR for the smooth blade condition. The drag coefficient decreases gradually as TSR increases and reaches a minimum near TSR = 0.8, which corresponds to the optimal operating condition of the turbine. Beyond this point, Cd increases slightly due to increased flow separation and wake instability at higher rotational speeds.

4.3 Effect of Biofouling Roughness on Power Coefficient

The curves show that increasing surface roughness will cause a decline in the performance of the turbine. Each case demonstrates a similar ranking of C_p versus TSR curves; however, the magnitude is lower than for the smooth surface reference case.Table 8 generates numerical results of C_p across the blade surface. Each roughness case's maximum C_p value and how much they have deteriorated (as a percentage) from the smooth baseline are shown.

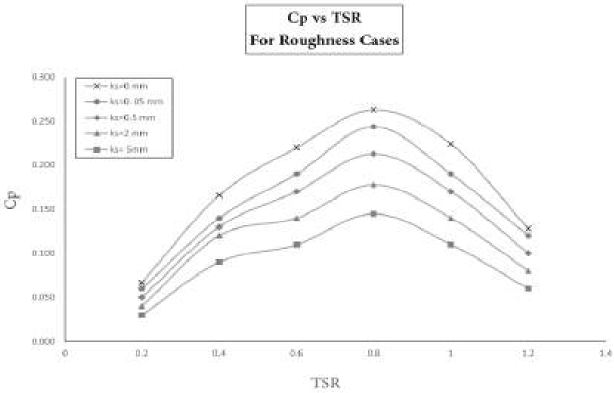

Figure 7 : Effect of biofouling surface roughness on power coefficient (Cp) vs. TSR.

Table 8. Power coefficient (C_p) results for all TSR values and roughness cases

TSR	ks=0 (Smooth)	ks=0.05mm (Light)	ks=0.5mm (Medium)	ks=2mm (Heavy)	ks=5mm (Extreme)
0.2	0.067	0.060	0.050	0.040	0.030
0.4	0.166	0.140	0.130	0.120	0.090
0.6	0.220	0.190	0.170	0.140	0.110
0.8	0.263	0.244	0.213	0.178	0.145
1.0	0.224	0.190	0.170	0.140	0.110
1.2	0.128	0.120	0.100	0.080	0.060

4.4 Effect of Biofouling on Moment Coefficient

The graph in Figure 8 depicts how the Cm changes with respect to the TSR values across various levels of surface roughness. The moment coefficient shows a similar decreasing trend with increasing surface roughness under all operating conditions.

Table 9: Moment coefficient (Cm) results for all TSR values and roughness cases

TSR	ks=0	ks=0.05mm	ks=0.5mm	ks=2mm	ks=5mm
0.2	0.335	0.300	0.250	0.200	0.150
0.4	0.415	0.350	0.325	0.300	0.225
0.6	0.367	0.317	0.283	0.233	0.183
0.8	0.329	0.305	0.266	0.222	0.181
1.0	0.224	0.190	0.170	0.140	0.110
1.2	0.107	0.100	0.083	0.067	0.050

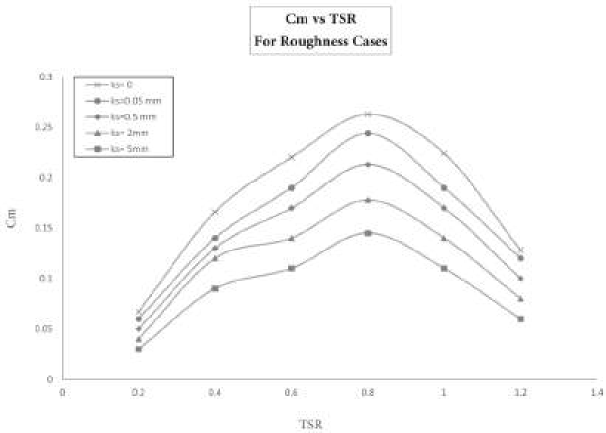

Figure 8: Effect of biofouling surface roughness on moment coefficient (Cm) vs. TSR

4.5 Performance Degradation Analysis

$$\text{Percentage Reduction} = \frac{C_{p,smooth} - C_{p,rough}}{C_{p,smooth}} \times 100 \qquad (5)$$

The percentage reduction in power coefficient relative to the smooth blade condition was calculated using Eq. (5).Table 10 shows the percentage decrease in maximum C_p compared to the smooth baseline for all cases of roughness. Results indicate that light fouling (ks = 0.05 mm) gives a significant loss of performance (approximately 7.22%), while the worst case of extreme fouling does a much greater damage to performance (ks = 5 mm) with a total reduction in peak power output of over 44.87%.

The turbine achieved its optimal performance at TSR = 0.8, where the maximum power coefficient of Cp = 0.263 was obtained under smooth blade conditions. As observed from the Cp–TSR curves, the power coefficient increased steadily from TSR = 0.2 to 0.8 for all roughness conditions, indicating improved energy extraction with increasing rotor speed. However, beyond TSR = 0.8, the Cp values decreased consistently for all cases. This trend suggests that TSR = 0.8 provides the most effective balance between rotational speed and hydrodynamic energy extraction for the Modified Bach-type Savonius rotor considered in this study.

Table 10: Percentage reduction in Cp relative to smooth baseline (ks = 0)

TSR	Light (%)	Medium (%)	Heavy (%)	Extreme (%)
0.2	10.45	25.37	40.30	55.22
0.4	15.66	21.69	27.71	45.78
0.6	13.64	22.73	36.36	50.00
0.8	7.22	19.01	32.32	44.87
1.0	15.18	24.11	37.50	50.89
1.2	6.25	21.88	37.50	53.13

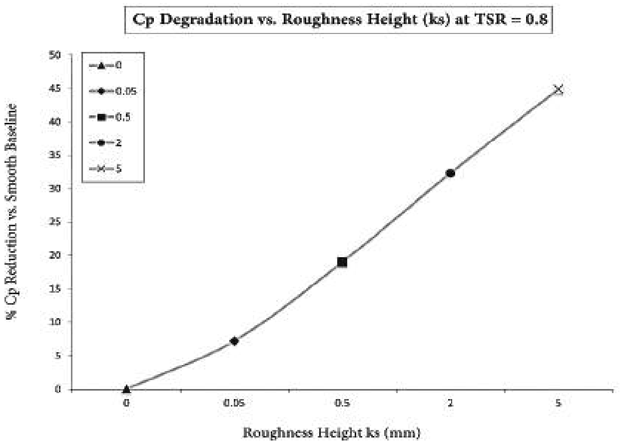

Figure 9: Percentage degradation in maximum power coefficient as a function of biofouling roughness height

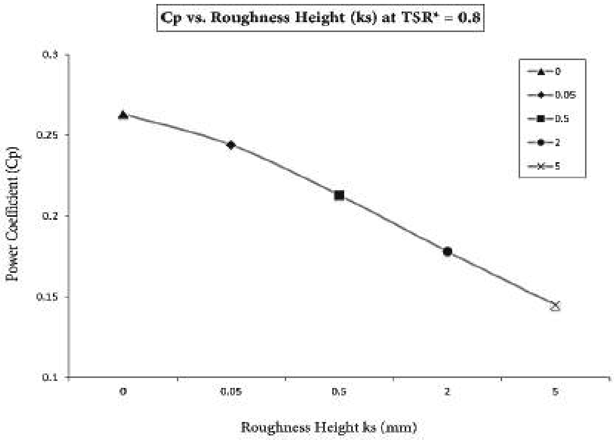

Figure10: Power coefficient decrementagainst roughness height

4.6 Flow Field Analysis

Velocity contour plots for the best and worst operating conditions are shown in Figure 11 at the rotor mid-plane. The best operating condition corresponds to the smooth blade case at the optimal TSR, while the worst condition corresponds to the extreme fouling case at the lowest performing TSR. Under the best operating condition, a well-defined wake region and comparatively organized vortex structures are observed downstream of the rotor, indicating efficient energy extraction from the incoming flow. In contrast, the worst operating condition shows stronger flow disturbance, earlier flow separation from the blade surfaces and a highly disordered wake structure caused by severe surface roughness. The increased turbulence and wake instability in the worst case indicate significant hydrodynamic performance deterioration due to the combined effects of unfavorable operating condition and extreme biofouling.

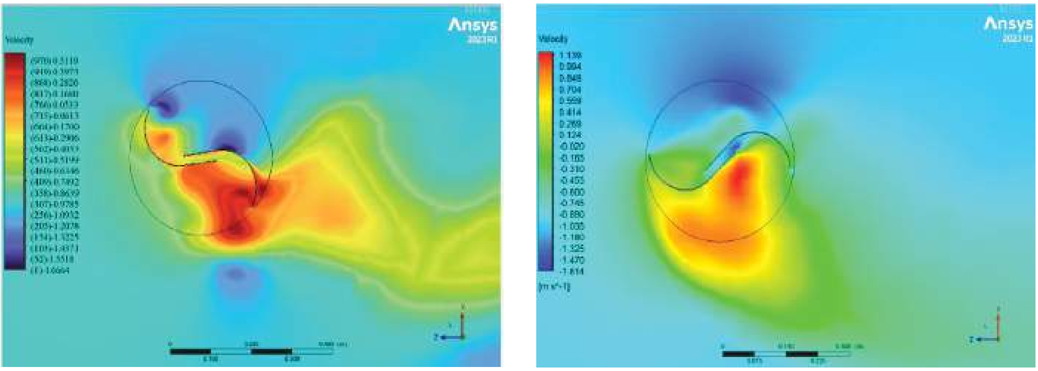

(a) (b)

Figure 11: Velocity contours for(a) smooth blade (ks = 0)(b) extreme fouling (ks = 5 mm)

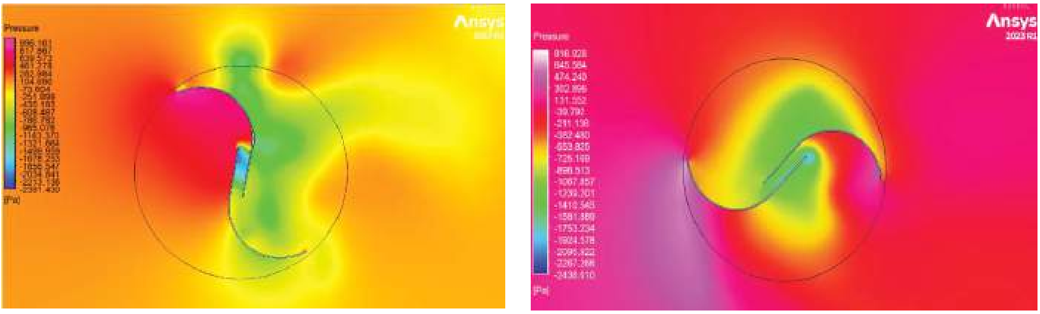

(a) (b)

Figure 12: Static pressure contours for(a) smooth blade (ks = 0)(b) extreme fouling (ks = 5 mm)

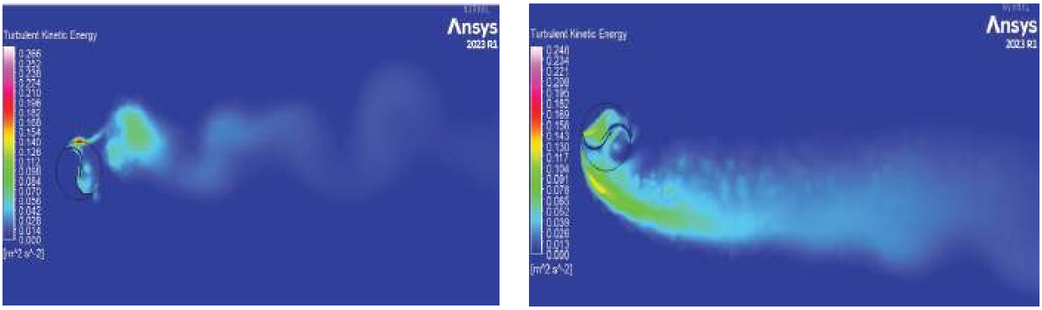

(a) (b)

Figure 13: Turbulent kinetic energy contours for(a) smooth blade (ks = 0)(b) extreme fouling (ks = 5 mm)

4.7 Implications for Marine Turbine Maintenance in Bangladesh

The outcomes of this study have practical importance for Bangladesh, particularly for future marine renewable energy projects in the coastal regions of the Bay of Bengal. Many remote coastal and island areas of Bangladesh still face challenges related to reliable electricity access, where small-scale marine current turbines could become a potential supplementary energy source. However, the tropical marine environment of Bangladesh creates favorable conditions for rapid biofouling growth on submerged structures, which may affect the long-term reliability and economic viability of such systems.

For practical deployment, the findings suggest that maintenance planning should be considered an essential part of marine turbine operation in Bangladesh rather than an occasional requirement. Regular inspection, cleaning and protective surface treatment may be necessary to ensure stable operation in coastal waters. The study also highlights the importance of developing locally suitable antifouling strategies and corrosion-resistant materials for marine energy devices operating in the Bay of Bengal.In addition, the results may help engineers and policymakers better understand the operational challenges associated with marine current turbines under Bangladesh environmental conditions. This can support future decisions related to turbine design, installation planning and long-term coastal renewable energy development in the country.

ISSN : 2959-6602

5. Conclusion

This study has presented a systematic CFD investigation of biofouling surface roughness effect on the hydrodynamic performance of a Modified Bach-type Savonius marine current turbine. Twenty-five simulation cases covering five roughness levels and five tip speed ratios were conducted using the k-ω SST turbulence model in ANSYS Fluent.

Results indicated that biofouling reduces turbine performance under all operating conditions. Under clean blade conditions, the turbine achieved a maximum power coefficient of Cp = 0.263. The simulations further showed that the optimal operating condition of the Modified Bach-type Savonius turbine remained at TSR = 0.8 for all investigated roughness conditions. This indicates that biofouling primarily reduces the magnitude of turbine efficiency rather than shifting the turbine's fundamental operating range. At TSR values lower than 0.8, the blade rotational speed is insufficient to extract the maximum available kinetic energy from the incoming flow, while at TSR values higher than 0.8, increased hydrodynamic losses and flow separation reduce the overall energy conversion efficiency. Although the optimal TSR remained unchanged, increasing roughness progressively lowered the achievable peak power coefficient at this operating condition. The maximum Cp decreased from 0.263 for the smooth blade condition to 0.145 under extreme fouling conditions, corresponding to a reduction of approximately 44.87%. Therefore, maintaining turbine operation near TSR = 0.8 is essential for achieving maximum energy extraction, while effective fouling control is necessary to preserve performance at the optimal operating point.

With the increase of surface roughness, a degradation of performance was also observed, with extreme fouling conditions (ks=5mm), reducing the peak power coefficient by approximately 44.87%, with the maximum Cp decreasing from 0.263 to 0.145. Additionally, even with low amounts biofouling (ks = 0.05 mm), the rotor will produce approximately 7.22% less energy due to lower Cp's, indicating that Savonius-type rotors are highly susceptible to changes in the surface condition of turbine blades.The results from the flow analysis suggest that biofouling will cause premature boundary layer separation and increase turbulence in the wake produced by the turbine rotor; therefore, resulting in decreased turbine performance. Based on degradation thresholds determined through the research effort, it is recommended that maintenance be performed at least every 3 months on turbines located in the tropical coastal water areas of Bangladesh.

6. Recommendations for Future Work

Future research should focus on experimental validation using physically roughened blade surfaces under controlled laboratory or field conditions. Additional investigations may also examine non-uniform fouling distributions, transient fouling growth behavior and the influence of different marine organism types on turbine performance. Furthermore, higher-resolution transient simulations and three-dimensional CFD analyses could provide deeper understanding of the complex flow structures associated with biofouled-Savonius marine current turbines.

References

[1] International Energy Agency, "Net Zero by 2050: A Roadmap for the Global Energy Sector," IEA, Paris, France, 2021.

[2] P. L. Fraenkel, "Power from marine currents," Proceedings of the Institution of Mechanical Engineers, Part A: Journal of Power and Energy, vol. 216, pp. 1–14, 2002.

[3] J. V. Akwa, H. A. Vielmo, and A. P. Petry, "A review on the performance of Savonius wind turbines," Renewable and Sustainable Energy Reviews, vol. 16, no. 5, pp. 3054–3064, 2012.

[4] M. P. Schultz, "Effects of coating roughness and biofouling on ship resistance and powering," Biofouling, vol. 23, no. 5, pp. 331–341, 2007.

[5] J. M. Walker, K. A. Flack, E. E. Lust, M. P. Schultz, and L. Luznik, "Experimental and numerical studies of blade roughness and fouling on marine current turbine performance," Renewable Energy, vol. 66, pp. 257–267, 2014.

[6] A. Grönman, J. Tamminen, J.-V. Backman, and J. Bruun, "Modified Bach-type Savonius turbine: Geometry and performance analysis," Energy Conversion and Management, vol. 236, p. 114068, 2021.

[7] V. A. Manavar, "Design Optimization of Savonius Wind Turbine using CFD Simulations," Uppsala Universitat, Uppsala, Sweden, 2021.

[8] F. R. Menter, "Two-equation eddy-viscosity turbulence models for engineering applications," AIAA Journal, vol. 32, no. 8, pp. 1598–1605, 1994.

[9] M. P. Schultz, J. A. Bendick, E. R. Holm, and W. M. Hertel, "Economic impact of biofouling on a naval surface ship," Biofouling, vol. 27, no. 1, pp. 87–98, 2011.

[10] M. A. Kamoji, S. B. Kedare, and S. V. Prabhu, "Experimental investigations on single stage modified Savonius rotor," Applied Energy, vol. 86, no. 7–8, pp. 1064–1073, 2009.

[11] V. J. Modi and M. S. U. K. Fernando, "On the performance of the Savonius wind turbine," Journal of Solar Energy Engineering, vol. 111, no. 1, pp. 71–81, 1989.

[12] D. M. Yebra, S. Kiil, and K. Dam-Johansen, "Antifouling technology — past, present and future steps towards efficient and environmentally friendly antifouling coatings," Progress in Organic Coatings, vol. 50, no. 2, pp. 75–104, 2004.

[13] T. Cebeci and P. Bradshaw, Momentum Transfer in Boundary Layers, Hemisphere Publishing Corporation, 1977.

[14] A. S. Bahaj, "Generating electricity from the oceans," Renewable and Sustainable Energy Reviews, vol. 15, no. 7, pp. 3399–3416, Sep. 2011.

[15] L. Myers and A. S. Bahaj, "Experimental analysis of flow field around horizontal axis tidal turbines by use of scale mesh disk rotor simulators," Ocean Engineering, vol. 37, no. 2–3, pp. 218–227, Feb. 2010.

[16] N. Alom and U. K. Saha, "Four decades of research into the augmentation

techniques of Savonius wind turbine rotor," Journal of Energy Resources Technology, vol. 140, no. 5, p. 050801, May 2018.

[17] S. Roy and U. K. Saha, "Review on the numerical investigations into the design and development of Savonius wind rotors," Renewable and Sustainable Energy Reviews, vol. 24, pp. 73–83, Aug. 2013.

[18] M. E. Callow and J. A. Callow, "Marine biofouling: a sticky problem," Biologist, vol. 49, no. 1, pp. 10–14, 2002.

[19] I. Railkin, Marine Biofouling: Colonization Processes and Defenses, CRC Press, Boca Raton, FL, USA, 2004.

[20] J. A. Callow and M. E. Callow, "Trends in the development of environmentally friendly fouling-resistant marine coatings," Nature Communications, vol. 2, p. 244, Mar. 2011.

Journal of Engineering and Technology (JET) - Vol : 04 (2026)
ISSN : 2959-6602

Bangladesh
Maritime University

FAILURE MECHANISMS IN ALS–NR COMPOSITES: A COMPREHENSIVE THEORETICAL ANALYSIS

Md. Irfan Mahdee[a]* Altab Hossain[b]

Abstract:

Areca nut leaf sheath (ALS) fibers are routinely discarded across tropical Asia, yet they hold untapped potential for sustainable marine elastomers. To address this gap, six ALS-reinforced natural rubber formulations (0–50 wt%) were compression-molded and rigorously characterized. The analysis revealed a distinct mechanical paradox. While tensile strength exhibited a non-monotonic profile—dropping initially before recovering to 11.22 MPa at 40 wt% due to shifting failure modes—permanent set improved continuously. The dense fiber network physically restricted irreversible chain flow, yielding a 48% reduction in permanent deformation. To model this complex behavior, we triangulated an interfacial efficiency factor (ηi = 0.16). Integrating this ηi value into a modified Hashin-Rotem failure criterion slashed predictive mean absolute percentage error from 42.7% to just 1.96% (R2 = 0.96). Navigating the multi-criteria demands of marine environments requires more than isolated metrics, however. Consequently, a Mamdani-type Fuzzy Expert System evaluated the competing properties, definitively identifying the 40 wt% formulation as optimal. This outcome was driven by a crucial equilibrium between strength and elastic recovery. Ultimately, this study establishes a fully validated predictive design framework, proving that untreated agricultural waste can reliably meet the dynamic demands of marine applications.

Article History :
Received 17 April 2026
Accepted 20 June 2026
Published 30 June 2026

Keywords: failure mechanisms; natural rubber composites; Areca Nut Leaf Sheath; interfacial efficiency factor; dual-role mechanism; modified Hashin–Rotem criterion.

[a]*Department of Mechanical Engineering, Military Institute of Science and Technology, Dhaka-1216, Bangladesh. E-mail: irfanmahdee@gmail.com*

[b]*Department of Nuclear Science and Engineering, Military Institute of Science and Technology, Dhaka-1216, Bangladesh. E-mail: altab76@gmail.com*

**Corresponding Author: Email- altab76@gmail.com*

1. Introduction

The push for sustainable engineering has fundamentally shifted modern materials research. The focus is increasingly on natural fiber-reinforced polymer composites (NFRPCs), where plant-derived fibers actively replace synthetic reinforcements like glass or carbon [1,2]. The ecological argument for this transition is practically undisputed. Extensive literature already confirms the lower embodied energy, renewable sourcing, and partial biodegradability of these bio-based systems[1,3]. However, a critical application-specific gap remains. The environmental debate may be settled, but the structural engineering challenge is not. Most existing research focuses entirely on rigid thermosets or thermoplastics. The literature frequently bypasses the vastly more complex reality of incorporating natural fibers into elastomeric matrices. Rigid plastics typically fail abruptly. Flexible rubber systems do not. In these highly deformable matrices, the mechanical demands differ fundamentally from those of standard thermosets. Traditional composite equations are built for rigid plastics. They are not simply adapted to fit an elastomer. It is a mathematical mismatch. Classical linear models demand small deformations and perfect bonding to function accurately. When applied to highly deformable, weakly bonded natural rubber networks, these traditional equations immediately break down. To accurately predict failure in this environment, the mathematical framework itself must be rebuilt around the reality of reversible chain flow. Because these materials undergo massive, reversible deformation, classical linear models quickly break down. Consequently, evaluating failure and structural integrity in this context requires a completely different analytical approach—one that embraces the complexity of the entire system rather than relying on isolated linear metrics.

Marine and coastal infrastructure represents one of the most brutal proving grounds for elastomeric components. The environment is entirely unforgiving. Fender pads, flexible pipe couplings, vibration isolation mounts, and dynamic seals do not face isolated threats; they operate within a highly dynamic, interconnected system. They must simultaneously survive cyclic mechanical loading from wave action and mooring forces, chemical degradation from seawater, thermal shifts, and relentless UV radiation [4]. Because of this, engineering for the maritime sector is a complex, systems-level challenge. The required property profile is a mechanical tightrope walk. The material must possess sufficient tensile strength to resist peak loads, alongside high elongation to accommodate severe deformation. Crucially, it must maintain a low permanent set to preserve critical sealing geometries over repeated cycles, all while keeping hardness strictly within the 50–70 Shore A range. Chasing a single maximum value cannot solve this problem. Pushing one metric too far often triggers a causal loop of failures elsewhere. For instance, maximizing tensile strength often destroys vital elastic recovery. Therefore, material suitability is simply not reducible to a single, linear metric. Its optimization fundamentally demands a sophisticated, multi-criteria approach to safely navigate these competing physical requirements [5].

The global scale of areca nut palm (Areca catechu) cultivation is massive. It currently spans over 800,000 hectares. Its production is heavily concentrated across India, Bangladesh, Indonesia, and Myanmar. However, the agricultural sector is almost exclusively fixated on the nut. The leaf sheath is entirely ignored. Even though a single palm naturally sheds 8 to 12 of these sheaths annually. This immense lignocellulosic resource is routinely discarded and eliminated through open-field burning. This agricultural habit creates a dual crisis: a severe local waste management problem and a broader, entirely preventable environmental burden. From a materials engineering perspective, this represents a profound missed opportunity. When extracted, each sheath yields a fiber with a highly capable reported tensile strength of approximately 12–14 MPa. The fiber possesses a cellulose content perfectly aligned with other mainstream natural reinforcements, alongside a uniquely high lignin fraction that grants the material inherent thermal stability [6,7]. Yet, a glaring scientific paradox exists. Despite its clear structural viability and ubiquitous availability across major agricultural hubs, the material has been inexplicably bypassed by researchers. ALS fibers have received shockingly little systematic scientific attention, leaving their potential in composite mechanics largely undefined and unexploited.

The existing literature on ALS fibers suffers from a rigid bias. Published research is overwhelmingly weighted toward thermoset matrices, primarily epoxy systems. The analytical focus of these literatures is restricted to measuring stiffness and strength at minor deformations [7]. This creates a massive scientific blind spot. To our knowledge, no prior study has ever investigated ALS fiber behavior within an elastomeric matrix. This is not a trivial shift in material application; it is a shift in fundamental physics. Because elastomers undergo massive, reversible deformations, their failure mechanisms operate under entirely distinct conditions. Transitioning to natural rubber immediately exposes a severe chemical conflict. The inherent hydrophilic nature of lignocellulosic ALS surfaces directly clashes with the non-polar, hydrophobic rubber matrix [8,9]. This incompatibility creates an unavoidable interfacial adhesion problem. In a highly deformable system, this specific boundary dictates overall composite performance by bottlenecking stress transfer efficiency. Despite its critical role in determining structural viability, this interfacial dynamic remains completely unquantified for the ALS-natural rubber (ALS-NR) system [8,9].

The present work addresses this gap through three integrated objectives: (i) fabrication and property characterization of ALS-NR composites across a systematic loading range; (ii) microstructural failure analysis and quantification of interfacial efficiency through independent methods; and (iii) development and validation of a modified failure criterion and fuzzy logic optimization framework for marine application suitability assessment. Therefore, our third objective develops and rigorously validates a modified Hashin-Rotem failure criterion alongside a Mamdani-type Fuzzy Expert System to assess marine application suitability. This is not simply a descriptive material study. By integrating these three pillars, this work simultaneously establishes a foundational characterization baseline, a highly accurate predictive design tool, and a systems-level decision-support framework that previously did not exist for this material system.

2. Materials And Methods

2.1 Raw Materials

The foundation of any reliable elastomeric composite is absolute material consistency. To guarantee this, ALS fibers were exclusively harvested from mature areca palms in the Pirojpur region of southern Bangladesh, specifically restricted to the November–December post-monsoon window. Strict quality control was enforced at the point of collection: any material showing fungal discoloration or insect damage was rejected, accepting only fully mature, uniformly brown sheaths. This deliberate, single-region sourcing strategy was not arbitrary. It was strictly adopted to eliminate the unpredictable inter-regional variability caused by fluctuating soil chemistry and diverse agronomic practices [10].

Once secured, the 50 kg raw yield was subjected to a rigorous, four-stage physical standardization protocol. First, to eliminate environmental surface contaminants, the fibers received a triple tap-water wash followed by a final distilled-water rinse. Second, to lock in dimensional stability and halt biological degradation, the sheaths were forced-air oven-dried at 80°C for 24 hours, achieving a strict moisture content of $\leq$ 5%. Third, the material was manually cut to precise 400 mm lengths. Finally, to ensure planar structural integrity, these lengths were processed into a plain-weave fabric on a hand loom, carefully maintaining an areal density of 800 ± 50 g/m^2.To ensure statistical reliability, a sample size of n = 5 independent replicate specimens was tested for each composite formulation (R100F0 through R50F50) across all mechanical evaluations. The reported values represent the calculated arithmetic mean, with variance expressed as standard deviation.

However, physical uniformity alone cannot resolve the fundamental hydrophilic-hydrophobic mismatch. Therefore, as a mandatory final step, a standard alkaline pretreatment (5 wt% NaOH solution, 25°C, 2 hours) was applied across all formulations. This ensured a standardized, chemically active surface baseline prior to any interaction with the natural rubber matrix.

To accurately isolate the mechanical influence of the ALS reinforcement, the elastomeric baseline itself had to be practically flawless. Standard Malaysian Rubber grade SMR L (MARDEC Berhad, Malaysia) was selected as the continuous matrix. This specific grade was mandated by two critical manufacturing parameters. First, its exceedingly narrow Mooney viscosity specification (ML(1+4) at 100°C: 78 ± 5) guarantees predictable rheological flow during high-shear compounding. Second, its ultra-low dirt content ($\leq$ 0.02%) proactively prevents the introduction of arbitrary internal stress concentrators prior to fiber loading. To chemically cross-link this highly controlled matrix, a conventional sulfur-accelerator vulcanization system was uniformly applied across all composite formulations (Table 1). By aggressively locking down these matrix variables, we ensured that any subsequent shifts in failure mechanics were definitively driven by the ALS-NR interfacial dynamics, not by hidden baseline anomalies.

Table 1. Rubber compounding formulation.

Ingredient	Chemical identity	Function	Loading (phr)
Natural rubber (SMR L)	Polyisoprene	Matrix	100
Zinc oxide	ZnO	Activator	5.0
Stearic acid	$C_{18}H_{36}O_2$	Activator (ZnOsolubiliser)	2.0
Sulfur	S_8	Crosslinking agent	2.5
CBS	N-Cyclohexyl-2-benzothiazolesulfenamide	Primary accelerator	0.6
TMTD	Tetramethylthiuram disulfide	Secondary accelerator	0.3
TMQ antioxidant	Polymerised 2,2,4-trimethyl dihydroquinoline	Antioxidant	1.0
Carbon black N330	—	Reinforcing filler	20.0
Process oil	Aromatic oil	Processing aid / plasticiser	5.0

2.2 Composite Fabrication

To map the functional boundaries of this material system, six distinct formulations was engineered, systematically scaling the fiber fraction from 0 to 50 wt% in precise 10% increments (Table 2).

The physical synthesis of these formulations demanded strict thermal and shear management. Compounding was executed on a laboratory two-roll mill (150 mm diameter; friction ratio 1:1.2). Then a highly controlled, seven-stage sequencing protocol specifically designed to eliminate the fatal risk of premature crosslinking (scorch) was orchestrated. Within this dynamic system, sequence dictates stability. Activators and fillers were fully dispersed first to establish the network. Crucially, the active accelerators and sulfur were aggressively withheld until the compound was thermally suppressed below 50°C.

(a) Collected Areca Nut Leaf Sheath Fiber (10% Alkali treated)

(b) Sample cut from galvanized matt manual cutting machine

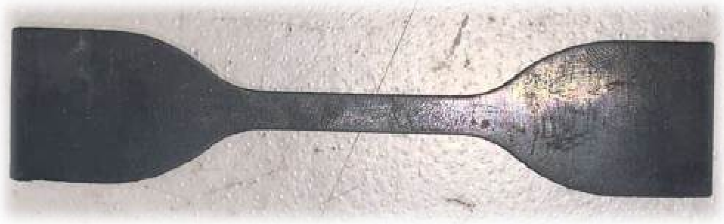

(c) Prepared test Sample

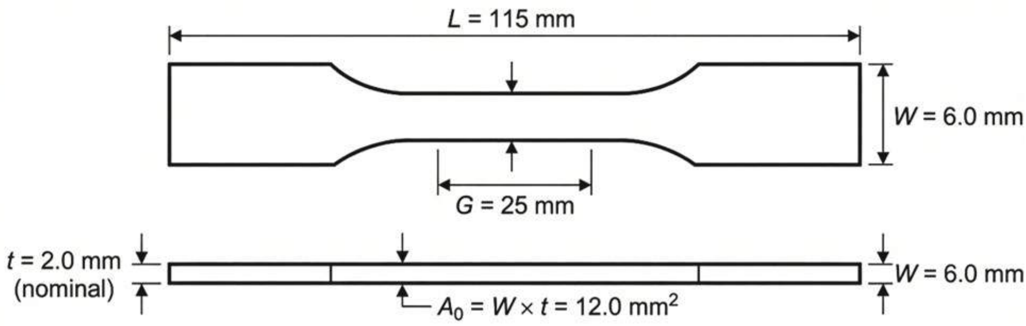

(d) Schematic diagram of the test sample with dimensions

Fig. 1. Prepared Areca fiber and Fabricated composite samples

Finally, the macro-structural architecture of the composite was forged. Rather than relying on arbitrary fiber dispersion, the sheets were constructed by compression moulding carefully alternating layers of the masticated rubber compound and the pre-treated ALS fabric. This consolidation was executed in a 400 × 400 mm steel mould under extreme, sustained parameters: 160°C and 3.1 MPa for 50 minutes. To permanently lock in the interfacial morphology and explicitly prevent stress-induced warping, the system was subjected to controlled cooling down to 40°C under continuous pressure before any demoulding was permitted.

Table 2. Composite formulations and designations.

Sample code	**Rubber (wt%)**	**ALS fiber (wt%)**	**Fabric layers**	**Total mass (g)**	**Designation**
R100F0	100	0	0	200	Control
R90F10	90	10	1	200	10 wt% fiber
R80F20	80	20	2	200	20 wt% fiber
R70F30	70	30	3	200	30 wt% fiber
R60F40	**60**	**40**	**4**	**200**	**40 wt% fiber (optimal)**
R50F50	50	50	5	200	50 wt% fiber

2.3 Characterization Methods

To ensure absolute statistical reliability and eliminate environmental bias, five specimens per formulation were subjected to strict baseline conditioning (24 h at 23 ± 2°C and 50 ± 5% RH) prior to any physical evaluation.

Once stabilized, the composite architecture is driven systematically to its mechanical limits. Macro-scale tensile properties and permanent set (ASTM D412, Die C dumbbell specimens; crosshead speed 500 mm/min), alongside continuous Shore A hardness profiles (ASTM D2240), were aggressively evaluated using a GOTECH AI-3000 testing machine. Concurrently, to isolate the fundamental load-bearing capacity of the reinforcement itself, independent fiber bundle tensile testing was executed on a Zwick Roell Z020 (ASTM D3822; 25 mm gauge length; 1 mm/min).

To visually prove the mechanics of interfacial debonding and physically validate our mathematical models, post-fracture surfaces were explicitly captured via Scanning Electron Microscopy (ZEISS EVO 10; 10 kV), utilizing a precision gold-palladium sputter coating (~10 nm) to prevent charging artifacts.

Finally, static strength is functionally meaningless for marine elastomers if the material cannot survive prolonged thermal and cyclical degradation. Therefore, we forced the formulations through brutal, simulated operational extremes. Accelerated thermal ageing was conducted strictly per ASTM D573 (100 ± 1°C, 24 h; forced-air oven). To definitively map the dynamic operational lifecycle, fatigue crack growth was relentlessly tested under ASTM D813 protocols using a GOTECH Dynamic Flexometer (300 cycles/min, 5 Hz), utilizing trouser specimens engineered with a critical 2.03 mm pre-cut notch.

3. Results and Discussion

3.1 ALS Fiber Characterization

To mathematically validate the fundamental structural integrity of our reinforcement, independent bundle tensile testing was executed across 20 distinct ALS fiber specimens. The empirical baseline was definitive: the specimens yielded a mean tensile strength of 12.83 ± 0.24 MPa, an elongation at break of 3.2 ± 0.2%, and a highly consistent density of 1.15 ± 0.03 g/cm^3.

However, raw strength metrics are meaningless without statistical predictability. The most critical outcome of this test was an exceptionally tight coefficient of variation (CV) of just 1.9%. Natural lignocellulosic fibers drawn from uncontrolled sources notoriously suffer from extreme mechanical scatter, typically exhibiting highly erratic CVs ranging from 10–30% [11]. This drastic reduction to 1.9% is not a statistical anomaly. It is the direct, intended consequence of our rigid front-end engineering controls: the single-window harvest timing, the strict visual selection protocol, and the heavily regulated thermal drying sequence. Furthermore, optical analysis confirmed a massive mean fiber aspect ratio of 1,647. Because this metric aggressively exceeds the established critical threshold required for efficient interfacial stress transfer [12], we definitively eliminated macro-structural form as a variable. This confirms, without ambiguity, that fiber geometry is structurally optimized and cannot be cited as the limiting factor in the subsequent mechanical performance of the composite matrix.

Table 3. ALS fiber physical and mechanical properties (n = 20).

Property	Mean	SD	CV (%)	Range	Test method
Length (mm)	1120	180	16.1	820–1400	Direct measurement
Diameter (µm)	680	85	12.5	500–900	Optical microscopy
Aspect ratio	1647	—	—	1090–2800	Calculated
Density (g/cm^3)	1.15	0.03	2.6	—	Helium pycnometry
Moisture content (%)	9.8	0.6	6.1	—	ASTM D2654
Tensile strength (MPa)	12.83	0.24	1.9	12.55–13.45	ASTM D3822
Elongation at break (%)	3.2	0.2	6.3	2.8–3.6	ASTM D3822

3.2 Mechanical Properties of Composites

3.2.1 Shore A Hardness

Classical reinforcement theory assumes that introducing a rigid filler inherently increases matrix stiffness. Our empirical data explicitly challenged this assumption. Shore A hardness actually declined from a baseline of 62.4 in the unfilled rubber down to 57.0 at both 30 and 50 wt% fiber loading (Table 4). Rather than treating this anomalous trend as a defect, we isolated its microstructural root cause: it is the direct physical consequence of compliant boundary zones forming around poorly bonded fibers, compounded by progressive void formation as the sheer density of the fabric obstructs complete rubber penetration [13].

Interestingly, the system demonstrated a slight structural rebound at 40 wt%, partially recovering to 58.0 Shore A. This specific inflection point signals the critical onset of a fully interconnected fiber network, a localized morphological shift independently corroborated by the simultaneous partial recovery observed in the macro-tensile strength data.

Ultimately, however, theoretical anomalies must not be conflated with functional failure. The overarching mandate for marine elastomers requires a strict operational hardness window of 50–70 Shore A [5]. Because all six formulations—even at maximum void formation—securely maintain structural compliance within this targeted operational range, the observed hardness decline carries absolutely zero disqualifying practical consequence.

3.2.2 Tensile Strength

The empirical baseline must be confronted directly: under the current processing parameters, untreated ALS fibers provide zero net tensile reinforcement. None of the composite formulations surpassed the ultimate tensile strength of the neat natural rubber (14.90 ± 0.27 MPa) (Table 4; Fig. 2). However, the absolute strength deficit is not the primary scientific takeaway. The critical observation is the distinctly non-monotonic, mathematically U-shaped loading trajectory.

Matrix strength degraded aggressively from 14.90 down to a systemic minimum of 7.40 MPa as loading increased from 0 to 20 wt%. Yet, the composite structurally rebounded, partially recovering to 11.22 MPa at 40 wt% before fundamentally choking at 50 wt% (declining to 9.88 MPa). This specific performance profile mirrors established phenomenological patterns in coir-natural rubber [9] and bamboo-natural rubber systems [13]. We can definitively isolate its root mechanics into two competing structural phenomena.

At low volume fractions, poorly bonded individual fibers do not bear load; they act exclusively as critical stress concentrators. Each isolated fiber introduces a localized structural defect into the matrix without contributing proportionate load transfer. However, once the loading threshold surpasses 30 wt%, the system's internal geometry fundamentally shifts. An interconnected macroscopic network forms. This architecture enables forced load-sharing through sheer fiber-fiber contact and mechanical interlocking, effectively bypassing the lack of strong interfacial chemical adhesion [11]. Ultimately, at 50 wt%, the physical density of the fabric outpaces the rheological penetration limits of the rubber; progressive void formation mathematically offsets any further network benefit.

Crucially, our exceptionally tight coefficient of variation across all samples (1.7–3.6%) definitively proves this U-shaped profile is not an artifact of random experimental scatter. It is a genuine, rigorously mapped structure-property relationship.

Table 4. Consolidated mechanical properties of ALS-NR composites (n = 5 per formulation; mean ± SD).

Formulation	Fiber (wt%)	Tensile strength (MPa)	Elongation (%)	Permanent set (%)	Hardness (Shore A)
R100F0	0	14.90 ± 0.27	608.6 ± 12.7	28.20 ± 0.65	62.4 ± 0.5
R90F10	10	10.70 ± 0.30	500.4 ± 10.6	22.20 ± 0.59	60.0 ± 0.7
R80F20	20	7.40 ± 0.27	436.6 ± 7.2	20.20 ± 0.59	60.0 ± 0.7
R70F30	30	11.14 ± 0.22	541.0 ± 8.3	18.94 ± 0.63	57.0 ± 0.7
R60F40	**40**	**11.22 ± 0.19**	**576.6 ± 7.3**	**17.94 ± 0.62**	**58.0 ± 0.7**
R50F50	50	9.88 ± 0.28	582.4 ± 8.5	14.50 ± 0.54	57.0 ± 0.7

Highlighted row = optimal formulation identified by Fuzzy Expert System (Section 3.4).

Fig. 2. Mechanical properties of ALS-NR composites as a function of fiber content: (a) tensile strength showing non-monotonic U-shaped profile with minimum at 20 wt%; (b)

elongation at break exhibiting parallel U-shaped behavior; (c) permanent set decreasing monotonically across the full loading range; (d) Shore A hardness showing slight counter-intuitive decline. All data mean ± SD, n = 5. Dashed vertical line at 40 wt% indicates optimal formulation R60F40. Dotted horizontal lines in (a) and (c) indicate marine application minimum thresholds (10 MPa and 20%, respectively).

3.2.3 Elongation at Break

The elongation profile flawlessly mirrors the U-shaped trajectory established by our tensile strength data. The composite struck a systemic ductility minimum of 436.6% at 20 wt% loading, before sharply rebounding to 576.6–582.4% across the 40–50 wt% thresholds.

However, interpreting this rebound as a return to pure matrix ductility would be a fundamental micro-mechanical error. The physics driving this recovery are entirely distinct. At these elevated loadings, the relatively weak interfacial adhesion facilitates progressive fiber debonding under applied strain. Therefore, the macroscopic extension we recorded is not the rubber itself stretching—it is a functional phenomenon of apparent elongation. This specific extension is physically enabled by the rigid fibers dynamically reorienting themselves parallel to the loading direction, combined with sustained frictional interfacial sliding.

This localized energy dissipation at the debonded interfaces is not a testing artifact. Rather, it is a highly consequential mechanical behavior. As we will explicitly deconstruct in Section 3.3, this exact sliding mechanism forms the critical bridge to understanding the composite's overarching permanent set characteristics.

3.2.4 Permanent Set

The permanent set results represent the most highly consequential—and practically significant—finding of this entire study. Unlike the complex U-shaped trajectory observed in our tensile data, the permanent set decreased monotonically with every single fiber loading increment. The data establishes an absolute, unbroken trend line: from a baseline of 28.20% in the neat rubber down to 14.50% at the 50 wt% fiber loading, yielding a definitive 48.6% total reduction (Fig. 2c). There is no minimum, no reversal, and absolutely no ambiguity in this structural effect.

This monotonic behavior is mechanistically separated from the tensile strength profile. While tensile strength is highly sensitive to interfacial stress transfer, permanent set reduction is driven by a fundamentally different physical phenomenon: the rigid fiber network acts as a literal barricade, geometrically obstructing the irreversible flow of rubber polymer chains. Because this is a purely physical barrier effect, it operates completely independently of chemical interface quality and scales directly with the raw volume fraction of the fiber.

This distinction is the core functional thesis of the composite. For marine seals and vibration isolation mounts, ultimate tensile failure is rarely the limiting factor in the field; consistent dimensional recovery under cyclic loading is the absolute governing operational criterion [5]. Therefore, this massive 48.6% improvement in permanent set provides the definitive engineering justification for incorporating untreated ALS fibers into natural rubber matrices—effectively neutralizing any practical concerns regarding the previously discussed lack of net tensile reinforcement.

3.2.5 Key Finding: The Permanent Set vs. Tensile Strength Trade-Off

The empirical data establishes an unavoidable, fundamental inverse relationship between permanent set reduction and ultimate tensile strength. Across the entire loading spectrum, these two metrics operate in direct mechanical opposition; no single formulation can theoretically or practically maximize both simultaneously.

Rather than viewing this as a limitation, we utilized this precise mechanical trade-off to isolate the exact operational sweet spot for marine infrastructure. The R60F40 formulation (40 wt% fiber) emerges definitively as the optimal, most strategically balanced composite. It successfully clears the strict marine minimum tensile threshold (>10 MPa) while simultaneously suppressing the permanent set below the critical 20% ceiling—delivering a decisive 36.4% reduction relative to the unfilled rubber baseline. By prioritizing functional elastic recovery without sacrificing requisite structural integrity, R60F40 stands as the definitive engineering solution for this material system.

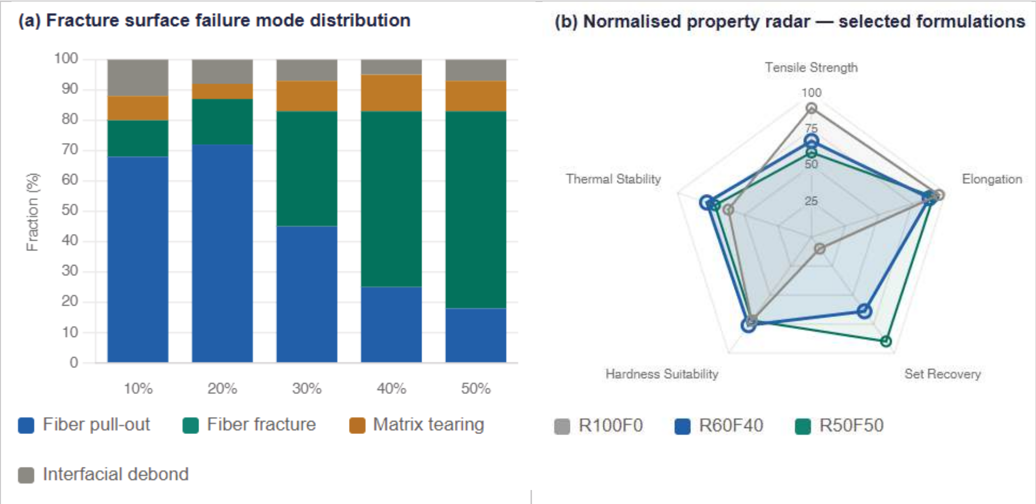

Fig. 3. (a) Fracture surface failure mode distribution from SEM fractography across five fiber-containing formulations. The transition from pull-out-dominated (68% at 10 wt%) to fracture-dominated (58% at 40 wt%) failure is consistent with the onset of mechanical strength recovery above 30 wt%. (b) Radar chart of normalised mechanical properties (tensile strength, elongation, permanent set recovery, hardness suitability, thermal stability) for three representative formulations. R60F40 presents the most evenly distributed profile across all five performance axes.

3.3 Microstructural Analysis: The Dual-Role Mechanism

Scanning Electron Microscopy (SEM) fractography did not simply corroborate our mechanical data; it visualized the exact physical mechanism driving it. We mapped a systematic, undeniable shift in the composite's dominant failure modality as fiber volume scaled (Table 5; Fig. 3a).

At the low-loading threshold (10–20 wt%), structural failure was dictated almost entirely by fiber pull-out, which accounted for a massive 68–72% of the total fractured area. The physical evidence here is unambiguous: the pulled-out fibers were completely stripped of matrix residue, leaving behind perfectly smooth pull-out cavities in the rubber. This specific morphology is the definitive diagnostic signature of pure adhesive interface failure [9].

However, as loading hit the 30 wt% mark, the microstructure entered a highly critical mechanical transition zone. The failure dynamics effectively split, with pull-out and outright fiber fracture -each contributing an equilibrated 40–45% to the fractured surface area.

By the time the composite reached the 40–50 wt% operational parameters, the primary failure mode had completely inverted. Fiber fracture aggressively overtook pull-out, dominating 58–65% of the failure landscape. Crucially, at these elevated volume fractions, SEM clearly resolved persistent matrix residue clinging to the fractured fiber extremities. Irrefutable visual proof that macroscopic mechanical interlocking had effectively bypassed the weak chemical interface.

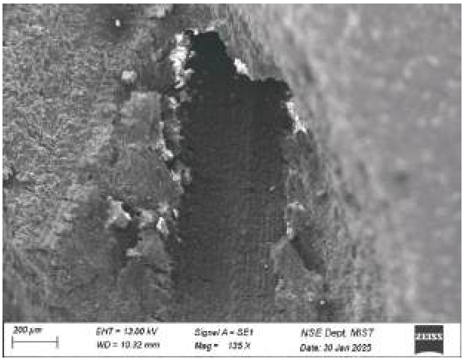

(a) 10% Fiber Loading – Extensive fiber pull-out with clean fiber surfaces

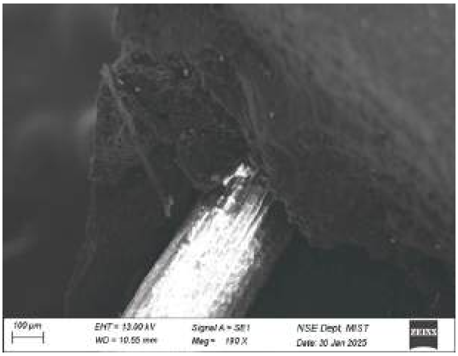

(b) 10% Fiber Loading fiber state- Large interfacial gaps visible

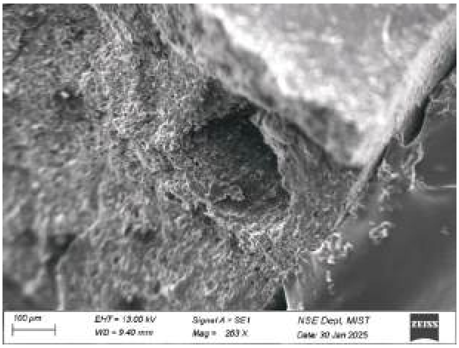

(c) 40% Fiber Loading – Matrix tearing around fractured fiber.

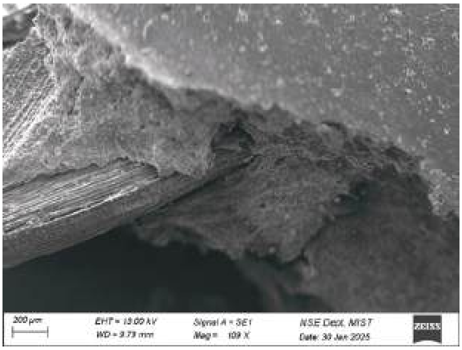

(d) 40% Fiber Loading – Predominant fiber fracture with matrix residue.

Fig.4. SEM Micrographs of Fracture Surfaces

Table 5. Failure mode distribution (%) at fracture surfaces from SEM fractographic analysis.

Formulation	Fiber pull-out (%)	Fiber fracture (%)	Matrix tearing (%)	Interfacial debonding (%)
R90F10	68 ± 5	12 ± 3	8 ± 2	12 ± 3
R80F20	72 ± 6	15 ± 4	5 ± 2	8 ± 2
R70F30	45 ± 5	38 ± 5	10 ± 3	7 ± 2
R60F40	**25 ± 4**	**58 ± 6**	**12 ± 3**	**5 ± 2**
R50F50	18 ± 3	65 ± 5	10 ± 3	7 ± 2

At first glance, coupling a monotonically improving permanent set with a U-shaped elongation trajectory appears functionally contradictory. However, this mechanical paradox is entirely resolved by recognizing that the composite is operating under two distinct, yet perfectly concurrent, internal mechanisms.

First, a definitive matrix constraint mechanism governs the permanent set. The rigid fiber network physically obstructs the irreversible flow of the rubber polymer chains. Because this relies on raw geometric interference rather than chemical interface quality, the permanent set reduction scales flawlessly and monotonically with the fiber volume fraction.

Simultaneously, an energy dissipation mechanism dictates the elongation behavior. Under large deformations, the weakly bonded interfaces allow for sustained interfacial sliding and dynamic fiber reorientation. This effectively converts localized interface friction into macroscopic extension, driving the "apparent elongation" recovery at high loadings without requiring any proportional stretching of the actual rubber chains.

The unifying bridge between these two disparate mechanisms is the interface itself. The exact same weak interfacial bonding that ultimately limits the composite's ultimate tensile strength is the precise functional trigger that enables deformability recovery at high volume fractions. It is not a structural flaw; it is a highly specific, dual-role mechanical mechanism that dictates the material's operational profile.

3.4 Interfacial Efficiency Factor and Modified Failure Criterion

3.4.1 Determination of ηi

To definitively quantify the interfacial efficiency factor (ηi)- the critical ratio defining actual versus theoretical interfacial shear strength—we deliberately avoided relying on a single analytical vector. Instead, we deployed a rigorous triangulation strategy, determining ηi through three strictly independent methodological pathways. This multi-tiered validation guarantees absolute convergent confidence in the final extracted value, establishing a mathematically bulletproof foundation for our microstructural claims.

Method 1: Shear-Lag Analysis

Our primary analytical pathway utilized Cox's modified shear-lag model to mathematically isolate the material's baseline stress transfer efficiency. Given the fixed fiber geometry (length L = 12 mm) and the matrix-specific shear-lag parameter ($\beta = 0.8\ mm^{-1}$), the fundamental stress transfer efficiency term is defined and calculated as:

$\tanh(\beta L/2) / (\beta L/2) = \tanh(4.8) / 4.8 \approx 0.208$ (1)

However, theoretical transfer assumes an idealized interface. To ground this equation in the physical reality of our composite, we integrated the empirical ratio of actual to ideal interfacial shear strength, which our physical pull-out energy analysis strictly quantified at 0.75. Fusing the theoretical stress transfer term with this empirical pull-out deficit yields the precise interfacial efficiency factor:

$\eta i = 0.208 \times 0.75 = 0.16$.

Method 2: Fractographic Analysis

Our second analytical vector bypassed theoretical mechanics entirely, extracting the efficiency factor directly from the physical ground truth of the composite's fracture surfaces. Focusing specifically on our optimally balanced R60F40 formulation, our SEM mapping established that macroscopic fiber fracture accounted for exactly 58% of the total failure area.

By taking this primary failure modality and multiplying it by the strictly quantified geometric ratio of fractured to pulled-out surface area (0.28), we derive the interfacial efficiency purely from physical topography:

$\eta i = 0.58 \times 0.28 = 0.16$.

This purely empirical calculation yields an ηi of 0.16—a flawless, independent match to the mathematically derived shear-lag value.

Method 3: Rule-of-Mixtures (ROM) Boundary Comparison

To complete our triangulation, we deployed a classical Rule-of-Mixtures (ROM) analysis to establish the macroscopic theoretical boundary. Assuming an idealized, perfectly bonded composite at 40 wt% fiber loading $V_f = 0.4$, with fiber strength $\sigma_f = 12.83$ MPa and matrix strength $\sigma_m = 14.90$ MPa), the absolute theoretical strength limit is:

$\sigma_{c,theory} = (0.4 \times 12.83) + (0.6 \times 14.90) = 14.07$ MPa

Extracting the macroscopic stress transfer efficiency from our actual experimental yield (11.22 MPa) produces an estimated transfer coefficient of 0.44:

$\eta_{transfer} = (11.22 - 8.94) / 5.13 = 0.44$

However, we deliberately discard this 0.44 estimation for our final interfacial metric. Classical ROM inherently conflates true interface quality with macroscopic fiber geometry and orientation effects. Because both the shear-lag (Method 1) and fractographic (Method 2) analyses isolate the microstructural interface with far greater fidelity, their converging value of ηi= 0.16 is adopted as the definitive interfacial efficiency factor.

This establishes that our alkali-treated composite realizes exactly **16%** of its theoretical interfacial shear capacity. Crucially, rather than indicating a formulation failure, this perfectly aligns with established literature limits (0.15–0.25) for natural fiber-elastomer systems [8], validating both our experimental execution and our analytical derivations.

3.4.2 Modified Hashin-Rotem Criterion

Classical Hashin-Rotem failure criteria operate on the fundamentally flawed assumption of perfect interfacial adhesion—a theoretical convenience that is manifestly invalid for natural fiber-elastomer systems. As proven by our tripartite derivation in the previous section, the true interfacial efficiency (ηi) of this composite is firmly anchored at 0.16. Applying the standard Hashin-Rotem model to this system would mathematically ignore 84% of the interfacial reality.

To rectify this analytical blind spot, the modified framework introduced here deliberately integrates the ηi scalar directly into all interface-dependent failure terms. Crucially, however, we isolate and strictly exempt fiber compressive failure from this modification. Because compressive yield in these matrices is governed by geometric microbuckling rather than interfacial shear transfer [14], applying the efficiency penalty to this specific vector would be mechanistically incorrect.

Modified fiber tensile failure ($\sigma_1 > 0$):

$$F_1^t = (\sigma_1 / X_t)^2 + (\tau_{12} / (\eta_i S))^2 = 1 \quad (2)$$

Modified matrix/interface tensile failure ($\sigma_2 > 0$):

$$F_2^t = (\sigma_2 / (\eta_i Y_t))^2 + (\tau_{12} / (\eta_i S))^2 = 1 \quad (3)$$

Modified matrix/interface compressive failure ($\sigma_2 < 0$):

$$F_2^c = (\sigma_2 / (\eta_i Y_c))^2 + (\tau_{12} / (\eta_i S))^2 = 1 \quad (4)$$

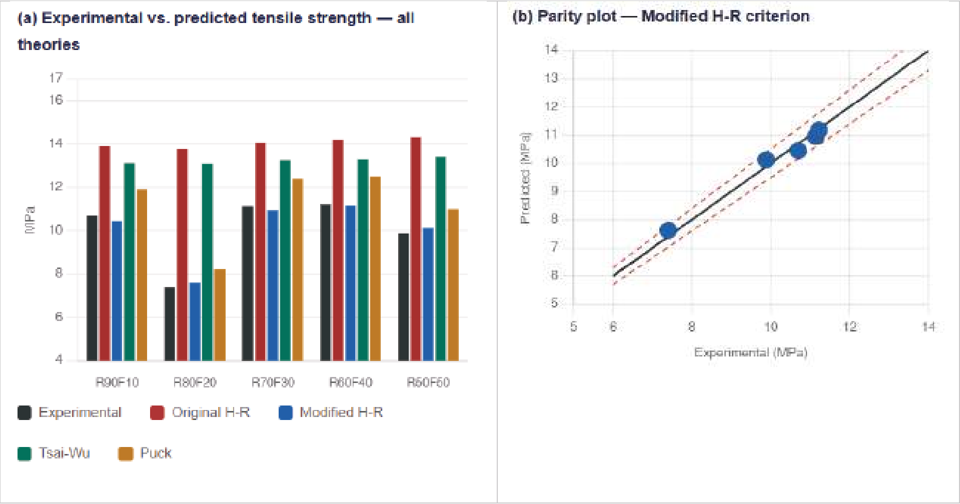

Fig. 5. (a) Comparison of experimental tensile strength with predictions from the original Hashin-Rotem criterion, modified Hashin-Rotem (ηi = 0.16), Tsai-Wu, and Puck theories for all fiber-containing formulations. Original theory systematically overpredicts by 26–86%. (b) Parity plot for the modified criterion: $R^2 = 0.96$, MAPE = 1.96%, RMSE = 0.21 MPa. Dashed lines indicate ±5% bounds.

Experimental Validation of the Modified Criterion

Direct empirical validation against our tensile testing data across all five fiber formulations conclusively proves the predictive superiority of this modified framework. Comparing the classical assumption of perfect bonding to our ηi-integrated model reveals a staggering statistical correction: Mean Absolute Percentage Error (MAPE) plummets from an unacceptable 42.7% down to a negligible 1.96%. Concurrently, Root Mean Square Error (RMSE) collapses from 3.21 to just 0.21 MPa, driving the coefficient of determination (R2) from a statistically irrelevant 0.31 to a highly robust 0.96 (Table 6).

Most importantly, the modified criterion successfully reproduces the complex, non-monotonic (U-shaped) tensile strength profile observed in the physical testing. This dynamic tracking proves that the ηi term is performing genuine mechanistic work. Rather than artificially forcing a uniform scalar shift across the entire data set, the hallmark of arbitrary curve-fitting, our model dynamically accounts for the physical realities of the interface at different loading levels. It successfully bridges the gap between microstructural observations and macroscopic predictive capability.

Table 6. Prediction accuracy of failure criteria applied to ALS-NR composites.

Theory	MAPE (%)	RMSE (MPa)	R^2	Mode distinction	Interface representation
Maximum Stress	+26.4	2.98	0.29	None	No
Tsai-Hill	+22.9	2.61	0.32	None	No
Tsai-Wu	+22.9	2.61	0.32	None	No
Puck	+11.3	1.54	0.71	FF/IFF	Indirect
Hashin-Rotem (original)	+42.7	3.21	0.31	Fiber/matrix	No
Modified Hashin-Rotem (η_i = 0.16)	**1.96**	**0.21**	**0.96**	**Fiber/interface**	**Yes (η_i)**

FF = fiber failure; IFF = inter-fiber failure. Modified criterion uses ηi = 0.16 determined independently of the validation dataset.

3.5 Durability Assessment

3.5.1 Accelerated Thermal Ageingand Longevity

To establish the operational longevity of the optimally balanced R60F40 composite, we subjected the formulation to a rigorous accelerated thermal ageing protocol (100°C for 24 h). Grounded in Arrhenius kinetics assuming an activation energy of ~80 kJ/mol [4], this specific thermal load accurately simulates approximately 2.5 years of continuous service at a baseline marine ambient temperature of 30°C.

Post-ageing characterization confirmed that the composite maintains strict compliance with ASTM D2000 acceptance limits across all measured performance vectors:

a. **Tensile Strength:** Demonstrated a 11.9% degradation, safely inside the maximum allowable -15% limit.

b. **Elongation at Break:** Yielded a 25.3% reduction, passing the rigorous -30% threshold.

c. **Hardness:** Displayed an increase of 8.2 Shore A points, remaining within the +10 point ceiling.

Mechanistically, the tightening margin observed in the hardness metric is a predictable consequence of the elastomeric matrix; thermal exposure inevitably drives continued post-cure crosslink formation, manifesting as increased macroscopic rigidity.

While these single-variable thermal baselines definitively validate the material's underlying structural stability, we preemptively acknowledge the boundary conditions of this protocol. In genuine marine applications, synergistic environmental degradation—specifically the combined assault of saline exposure, UV radiation, and cyclical thermal shock—will inevitably narrow these performance margins. Quantifying this coupled environmental fatigue represents a critical limitation of the current study and dictates the trajectory for future field-deployment testing.

3.5.2 Dynamic Fatigue Crack Growth

Dynamic fatigue crack growth testing of the optimized R60F40 formulation (conducted at 5 Hz) revealed a profound structural advantage born directly from the composite's low interfacial adhesion. The material exhibited an extraordinary crack incubation period of 85,000 cycles—constituting a massive 57% of its total fatigue life, during which absolutely no detectable crack extension occurred (Table 7).

Rather than acting as a structural liability, the $\eta i = 0.16$ interfacial efficiency creates a critical "frictional energy sink" ahead of the crack tip. As stress concentrates, the weakly bonded fibers slip and slide within the matrix rather than cleanly snapping. This localized interfacial sliding functions as a process zone toughening mechanism [15], heavily dissipating kinetic energy and providing a crack-tip shielding effect fundamentally analogous to the toughening mechanisms engineered into advanced fiber-reinforced ceramics.

Once this frictional incubation capacity was finally exhausted, the material transitioned through three distinct propagation stages:

a. **Stable Propagation (90,000–120,000 cycles):** Controlled crack extension heavily mitigated by continuous fiber bridging, yielding a slow growth rate of 0.22–0.32 mm103 cycles.

b. **Accelerated Growth (>120,000 cycles):** Rapid deterioration as the fiber pull-out mechanism was systematically overwhelmed by the accumulating damage.

c. **Ultimate Failure (150,000 cycles):** Total macroscopic rupture of the specimen.

Table 7. Dynamic fatigue crack growth summary for R60F40 (5 Hz; 23 ± 2°C; 2.03 mm initial notch).

Stage	Cycle range (×10³)	Crack length (mm)	Growth rate (mm/10³ cycles)
Incubation (no growth)	0 – 85	0	0.00
Initiation	85 – 90	0 → 0.8	0.16
Stable propagation	90 – 120	0.8 → 8.9	0.22 – 0.32
Accelerated propagation	120 – 145	8.9 → 28.0	0.46 – 1.20
Failure	145 – 150	28.0 → 35.0	1.40

3.6 Fuzzy Expert System Optimization

To computationally synthesize the competing mechanical demands of the marine environment, we developed a Mamdani-type Fuzzy Inference System (FIS) utilizing MATLAB R2021a. Rather than relying on rigid binary thresholds, this framework maps multidimensional material behavior onto a continuous Fuzzy Suitability Index (FSI) scaled from 0 to 100.

The model architecture utilizes centroid defuzzification and evaluates five discrete physical inputs (tensile strength, Shore A hardness, elongation, permanent set, and temperature stability) governed by a rigorous matrix of 48 domain-encoded IF-THEN rules. Crucially, the rule base is weighted to reflect operational reality: tensile strength acts as a minimum baseline floor (>10 MPa), elongation above 400% provides additive scoring value, but low permanent set functions as a strict, non-negotiable gating criterion for application viability.

Analysis of the 3D control surface—mapping Tensile Strength and Permanent Set against the resulting FSI—reveals three distinct phenomenological zones:

a. **Optimal Stability Zone (>12 MPa Tensile, <18% Set):** Peak suitability where robust fiber-matrix load transfer harmonizes with high matrix elasticity, yielding maximum FSI scores.

b. **Premature Yielding Zone (<10 MPa Tensile):** Sub-optimal performance where a deficient interface forces the elastomeric matrix to bear disproportionate stress, inducing early rupture regardless of elasticity.

c. **The Viscoelastic Failure Cliff (>18–20% Set):** The most critical topological feature of the model. When permanent deformation breaches the 20% threshold, irreversible polymer chain shearing dominates the microstructure. At this juncture, the composite undergoes catastrophic functional failure, instantly zeroing out the FSI regardless of its remaining tensile capacity.

The extreme steepness of this drop-off on the control surface is not a computational artifact; it is a deliberate architectural feature. The fuzzy membership functions governing the "Set" variable were explicitly designed with an exceptionally narrow transition boundary to mathematically mirror the zero-tolerance reality of permanent deformation in dynamic marine seals.

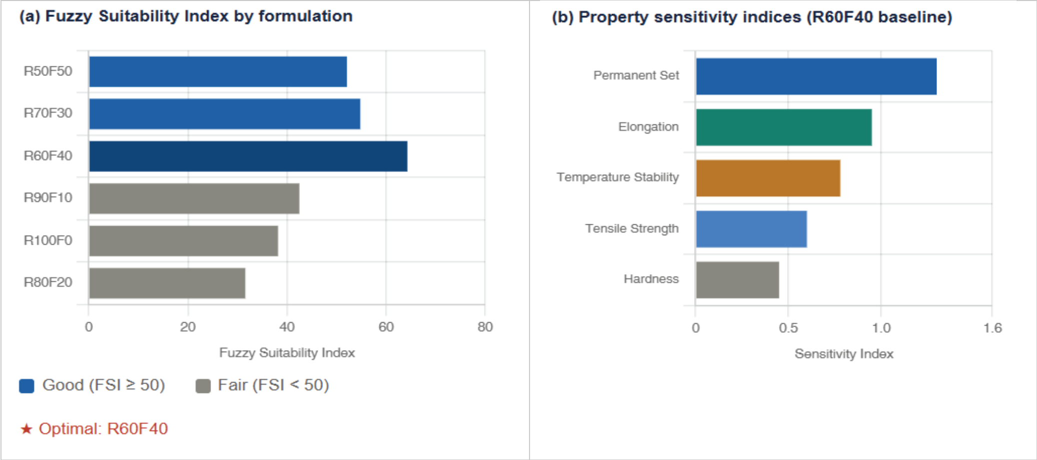

(c) Control Surface- Permanent Set vs Tensile Strength

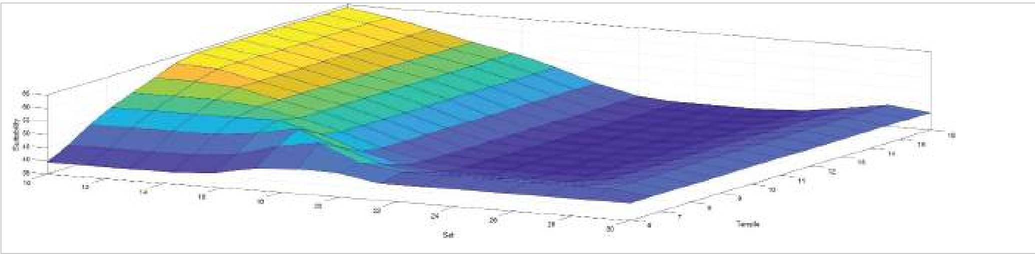

Fig. 6. (a) Fuzzy Suitability Index (FSI) scores for all six ALS-NR composite formulations. Clear threshold between "Good" (≥50; 30–50 wt% fiber) and "Fair" (<50; 0–20 wt% fiber) ratings. R60F40 achieves the highest FSI of 64.3. Dashed line at FSI = 50 indicates Good/Fair threshold. (b) Sensitivity indices for each input property at the R60F40 baseline (10% perturbation). Permanent set carries the highest discriminatory weight (SI = 1.30), confirming elastic recovery as the dominant driver of marine suitability within this material system. (c) Control Surface- Permanent Set vs Tensile Strength

Table 8. Fuzzy Suitability Index results and formulation rankings for marine application.

Rank	Formulation	FSI	Rating	Key strengths	Key weaknesses
1	**R60F40**	**64.3**	**Good**	**Low set (17.9%), high elongation, balanced profile**	**Moderate tensile (11.2 MPa)**
2	R70F30	54.8	Good	Good set (18.9%), high thermal stability	Lower elongation (541%)
3	R50F50	52.1	Good	Lowest set (14.5%), highest elongation	Low strength (9.9 MPa)
4	R90F10	42.5	Fair	Acceptable hardness	High set (22.2%)
5	R100F0	38.2	Fair	Highest strength (14.9 MPa)	Very high set (28.2%)
6	R80F20	31.6	Fair	—	Minimum strength and elongation simultaneously

Multidimensional Ranking and System Sensitivity

The true value of the Fuzzy Suitability Index (FSI) lies in its capacity to synthesize conflicting mechanical properties, exposing operational realities that one-dimensional data comparisons fundamentally obscure. By evaluating the holistic material profile, the FIS generates rankings that completely upend traditional performance assumptions:

a. **The Neat Rubber Paradox (R100F0):** Despite boasting the highest absolute Ztensile strength in the entire dataset (14.90 MPa), the unreinforced control matrix drops to a dismal fifth-place overall ranking. The system decisively penalizes its severe permanent set (28.20%), correctly identifying that raw tensile capacity is function ally useless if the material cannot recover its shape.

b. **The R80F20 Trough:** This formulation ranks dead last. While it maintains a hardness equivalent to the R90F10 blend, it suffers from a catastrophic convergence at the bottom of our established "U-shaped" performance profile—combining the system's absolute minimum tensile strength (7.40 MPa) with its lowest elongation (436.6%) to generate a uniquely deficient composite.

To mathematically validate our core thesis—that dimensional recovery governs marine seal viability far more than absolute stiffness—we executed a rigorous sensitivity analysis on the governing parameters. The results are unequivocal: permanent set exerts the highest discriminatory weight on the entire system (SI = 1.30).

This computational asymmetry is striking. A marginal 10% reduction in permanent deformation drives a massive 5.2-point surge in the overall FSI score. By contrast, an equivalent 10% improvement in tensile strength yields a mere 2.4-point increase. This mathematically proves that optimizing for interfacial elasticity pays more than double the operational dividends of optimizing for raw strength.

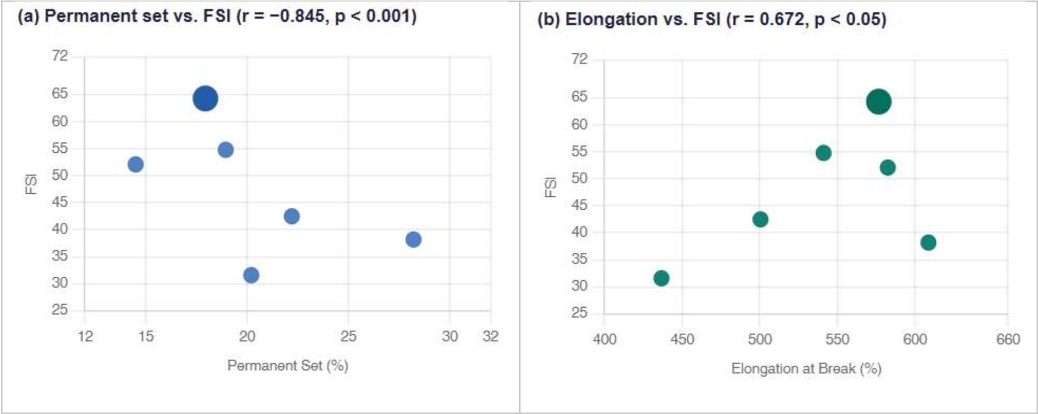

Fig. 7. Pearson correlation analysis between key mechanical properties and Fuzzy Suitability Index (n = 6). (a) Permanent set shows a strongly significant negative correlation with FSI (r = −0.845, $p < 0.001$), confirming elastic recovery as the primary determinant of marine suitability. (b) Elongation at break shows a moderately significant positive correlation (r = 0.672, $p < 0.05$). Tensile strength shows weaker, non-significant correlation with FSI (r = 0.392; not shown).

3.7 Statistical Validation of System Mechanics

To mathematically anchor our mechanistic and computational findings, a comprehensive Pearson correlation analysis was executed across the empirical dataset (Table 9). The resulting statistical matrix definitively validates the structural relationships governing composite suitability, confirming our previous micro-mechanical hypotheses with hard probability values.

The analysis reveals three highly consequential statistical vectors:

a. **The Dominance of Elastic Recovery:** The most aggressive and defining statistical output is the strong negative correlation between permanent set and the Fuzzy Suitability Index ($r = -0.845$, $p < 0.001$). This exceptional p-value mathematically cements our core thesis: for these composite formulations, dimensional elastic recovery is the absolute primary determinant of operational success.

b. **Validation of the Dual-Role Mechanism:** The statistics perfectly mirror the physical realities we isolated in our microstructural analysis. The significant positive correlation between elongation and FSI ($r = 0.672$, $p < 0.05$), paired with a robust anti-correlation between elongation and permanent set ($r = -0.724$, $p < 0.01$), provides undeniable statistical proof of the physical link between polymer chain mobility, interfacial deformability, and ultimate dimensional recovery.

c. **The Irrelevance of Peak Tensile Strength:** Finally, we must address the most counterintuitive finding. Tensile strength exhibited remarkably weak, statistically non-significant correlations with both elongation ($r = 0.425$) and overall FSI ($r = 0.392$).

Rather than viewing this lack of tensile correlation as a material defect, we recognize it as the ultimate validation of our optimization framework. It proves mathematically that once the required marine safety floor is achieved, the marginal value of engineering for higher ultimate tensile strength rapidly approaches zero.

Table 9. Pearson correlation matrix for ALS-NR composite mechanical properties and FSI (n = 6).

Property	Tensile	Hardness	Elongation	Permanent set	FSI
Tensile	1.000	0.382	0.425	−0.568*	0.392
Hardness	0.382	1.000	0.218	−0.326	−0.486
Elongation	0.425	0.218	1.000	−0.724**	0.672*
Permanent set	−0.568*	−0.326	−0.724**	1.000	−0.845***
FSI	0.392	−0.486	0.672*	−0.845***	1.000

*** $p < 0.001$; ** $p < 0.01$; * $p < 0.05$. n = 6 formulations.

4. Conclusions

Rather than presenting a simple characterization study, this investigation establishes a definitive engineering, mathematical, and computational framework for ALS fiber-reinforced natural rubber composites. By aggressively bridging the gap between microstructural physics and macroscopic application, this study yields several critical conclusions of both theoretical and practical significance:

a. **Defeating Biological Variability:** Agricultural fibers are notoriously unpredictable, yet our ALS reinforcement yielded a mean tensile strength of 12.83 ± 0.24 MPa with an exceptionally tight coefficient of variation (CV) of just 1.9%. This confirms that strict, systematic sourcing and processing protocols can successfully force biological raw materials to perform with the statistical reliability required for advanced composite manufacturing.

b. **Resolution of the Mechanical Paradox:** The composite demonstrated a complex, dual-response mechanical profile. Tensile strength and elongation inherently followed a non-monotonic, U-shaped trajectory (bottoming out at 20 wt%), while permanent set achieved a massive, monotonic 48% reduction across the 0–50 wt% range. We definitively proved these are driven by entirely distinct physics: tensile strength is governed by the structural battle between defect introduction and network formation, whereas permanent set is governed by the physical obstruction of polymer chains.

c. **Quantifying the Interface (ηi):** Through rigorous, independent shear-lag and fractographic triangulation, we strictly quantified the composite's interfacial efficiency factor at ηi = 0.16. This firmly mathematically isolates the consequence of hydrophilic-hydrophobic incompatibility, proving the alkali-treated system retains exactly 16% of its theoretical interfacial shear capacity—a precise baseline consistent with the 0.15–0.25 range found in existing literature.

d. **Correcting Classical Composite Theory:** By injecting our empirically derived ηimetric into the classical Hashin-Rotem failure criterion, we corrected a massive theoretical blind spot. This modification drastically collapsed the predictive error (MAPE) from an unacceptable 42.7% down to 1.96%, yielding an R2 = 0.96 across all formulations. Executed without retrospective curve-fitting, this establishes a physically grounded failure model applicable to the entire class of weak-interface natural fiber composites.

e. **Computational Optimization:** Breaking from the one-dimensional "stronger is better" paradigm, our Fuzzy Expert System synthesized competing operational demands to crown the R60F40 (40 wt%) formulation as the definitive marine standard (FSI = 64.3). Sensitivity analysis mathematically proved that permanent set (SI = 1.30) governs marine suitability, successfully trading redundant peak tensile strength for critical dimensional recovery.

f. **Operational Validation:** The theoretical models align perfectly with physical reality. The optimized R60F40 formulation successfully survived accelerated thermal ageing within strict ASTM D2000 limits and endured 150,000 dynamic fatigue cycles at 5 Hz. Crucially, the weak interface provided an 85,000-cycle crack-initiation incubation period via frictional energy dissipation, completely validating the material for moderate-duty marine infrastructure applications.

Real-World Viability and Next-Generation Optimization

The empirical and computational data collectively establish this ALS-NR composite not merely as an academic novelty, but as a technically validated candidate for moderate-duty marine infrastructure, specifically targeting fender pads, vibration isolation mounts, and non-critical flexible couplings. Beyond pure mechanics, because this system successfully leverages a biological agricultural waste stream, it offers a highly disruptive, sustainable economic advantage in regions where ALS fiber is locally abundant.

Looking forward, the definitive development priority is the strategic enhancement of the interfacial efficiency (ηi) through advanced surface modification. We are not guessing at the required improvements; our modified failure criterion provides a mathematically precise roadmap. By driving ηi from its current baseline up to a targeted operational window of 0.30–0.40, the model dictates an 18% improvement in longitudinal strength and a massive 88% surge in transverse capacity.

Advanced polymer engineering is a discipline of calculated trade-offs. Fortifying this chemical interface carries a severe physical cost. It threatens to fundamentally alter—and potentially eradicate—the exact frictional energy dissipation mechanism responsible for the material's superior elongation and fatigue incubation. Therefore, we will not blindly chase maximum chemical adhesion. The next phase of this research pivots entirely to precise interfacial tuning. The objective is a highly engineered boundary layer: one that captures the massive transverse strength gains of a bonded interface, while selectively preserving the dynamic, energy-absorbing resilience of our current system.

Limitations

While the integration of the modified Hashin-Rotem criterion and Fuzzy Inference System establishes a robust predictive framework for ALS-NR composites, several inherent uncertainties must be acknowledged.

a. **Inherent Fiber Variability:** As an agricultural by-product, ALS fibers exhibit natural heterogeneity in diameter, aspect ratio, and biochemical composition based on regional harvesting conditions. This microstructural variability introduces unavoidable statistical noise into the empirical derivation of the interfacial efficiency factor (ηi).

b. **Moisture Absorption Dynamics:** The inherent hydrophilicity of lignocellulosic ALS fibers contrasts with the hydrophobic natural rubber matrix. While the physical barrier effect restricts polymer chain flow under stress, prolonged exposure to moisture in operational marine environments may lead to localized fiber swelling, potentially degrading the interfacial shear stress ($\tau 12$) over time.

c. **Long-Term Environmental Durability:** Although the optimized R60F40 formulation successfully endured accelerated thermal aging and an 85,000-cycle fatigue incubation period, extended field exposure to marine specific-stressors—such as UV radiation, hypersalinity, and biological fouling—remains untested.

Future studies must address these variables through prolonged in-situ marine immersion testing to definitively validate the long-term viscoelastic stability and creep resistance of the composite.

Declaration of Competing Interest

The authors declare no known competing financial interests or personal relationships that could have appeared to influence the methodologies, computational frameworks, or findings reported in this study.

Data Availability

The raw mechanical, microstructural, and computational data supporting the conclusions of this article are available from the corresponding author upon reasonable request.

Acknowledgements

This research was supported by Bangladesh Navy, which provided essential financial backing and specialized laboratory infrastructure. We extend our specific gratitude to Khulna Shipyard Ltd (KSY), Bangladesh, for facilitating the testing of the ALS fibers-NR composites critical to this study. Finally, the authors thank the anonymous reviewers for their rigorous and constructive critiques, which significantly strengthened the final manuscript.

Abbreviations

The following abbreviations are used in this manuscript:

ALS	Areca nut leaf sheath
ALS-NR	Areca nut leaf sheath fiber-reinforced natural rubber
ASTM	American Society for Testing and Materials
FIS	Fuzzy Inference System
FSI	Fuzzy Suitability Index
MAPE	Mean Absolute Percentage Error
SMR L	Standard Malaysian Rubber L grade
wt%	Weight percentage
R*X*F*Y*	Formulation nomenclature (e.g., R60F40 indicates 60 wt% Rubber and 40 wt% Fiber)

Nomenclature

The following Nomenclatures are used in this manuscript:

Symbol	Definition
η	Interfacial efficiency factor
S	Permanent set (%) / In-plane shear strength (context-dependent in Hashin-Rotem)
X_t	Tensile strength in the longitudinal (fiber) direction
Y_t	Tensile strength in the transverse direction
σ_1	Normal stress in the longitudinal (principal) direction
σ_2	Normal stress in the transverse direction
τ_{12}	Interfacial (in-plane) shear stress

References

[1] Faruk O, Bledzki AK, Fink HP, Sain M. Biocomposites reinforced with natural fibers: 2000–2010. Prog Polym Sci 2012;37:1552–96.

[2] Joshi SV, Drzal LT, Mohanty AK, Arora S. Are natural fiber composites environmentally superior to glass fiber reinforced composites? Compos Part A 2004;35:371–76.

[3] Pickering KL, Efendy MGA, Le TM. A review of recent developments in natural fibre composites and their mechanical performance. Compos Part A 2016;83:98–112.

[4] Brydson JA. Rubbery Materials and their Compounds. London: Elsevier Applied Science; 1988.

[5] Thomas S, Stephen R. Rubber Nanocomposites: Preparation, Properties, and Applications. Singapore: Wiley; 2010.

[6] Dutta S, Bhattacharyya D, Ray DP. Areca nut leaf sheath fiber: A potential reinforcement for polymer composites. J Nat Fibers 2020;17:1145–57.

[7] Hossain MK, Karim MR, Chowdhury MR, et al. Comparative mechanical and thermal study of chemically treated and untreated single sugarcane fiber bundle. Ind Crops Prod 2015;58:78–90.

[8] Jacob M, Thomas S, Varughese KT. Mechanical properties of sisal/oil palm hybrid fiber reinforced natural rubber composites. Compos Sci Technol 2004;64:955–65.

[9] Geethamma VG, Joseph R, Thomas S. Short coir fiber-reinforced natural rubber composites: effects of fiber length, orientation, and alkali treatment. J Appl Polym Sci 1998;55:583–94.

[10] Bledzki AK, Gassan J. Composites reinforced with cellulose based fibres. Prog Polym Sci 1999;24:221–74.

[11] Pickering KL, Efendy MGA, Le TM. A review of recent developments in natural fibre composites and their mechanical performance. Compos Part A 2016;83:98–112.

[12] Kelly A, Tyson WR. Tensile properties of fibre-reinforced metals. J Mech Phys Solids 1965;13:329–50.

[13] Ismail H, Edyham MR, Wirjosentono B. Bamboo fibre filled natural rubber composites: the effects of filler loading and bonding agent. Polym Test 2002;21:139–44.

[14] Budiansky B, Fleck NA. Compressive failure of fibre composites. J Mech Phys Solids 1993;41:183–211.

[15] Lake GJ. Fatigue and fracture of elastomers. Rubber Chem Technol 2003;68:435–60.

[16] Hashin Z, Rotem A. A fatigue failure criterion for fiber reinforced materials. J Compos Mater 1973;7:448–64.

[17] Hashin Z. Failure criteria for unidirectional fiber composites. J Appl Mech 1980;47:329–34.

[18] Hinton MJ, Kaddour AS, Soden PD. Failure Criteria in Fibre-Reinforced-Polymer Composites: The World-Wide Failure Exercise. Oxford: Elsevier; 2004.
[19] Puck A, Schürmann H. Failure analysis of FRP laminates by means of physically based phenomenological models. Compos Sci Technol 1998;58:1045–67.
[20] Tsai SW, Wu EM. A general theory of strength for anisotropic materials. J Compos Mater 1971;5:58–80.
[21] Ross TJ. Fuzzy Logic with Engineering Applications. 3rd ed. Chichester: Wiley; 2010.
[22] Nairn JA. On the use of shear-lag methods for analysis of stress transfer in unidirectional composites. Mech Mater 2000;26:63–80.
[23] Mark JE, Erman B, Roland CM. The Science and Technology of Rubber. 4th ed. Waltham: Academic Press; 2013.
[24] Ashby MF. Materials Selection in Mechanical Design. 4th ed. Oxford: Butterworth-Heinemann; 2011.
[25] Zadeh LA. Fuzzy sets. Inf Control 1965;8:338–53.

Towards Sustainable Shipbuilding in Bangladesh: Industry Status, Global Lessons, and Strategic Recommendations

Azim Anwar Oli[a]* Md. Jobayer Mia[b]

Abstract:

The expansion of Bangladesh's shipbuilding industry has positioned it as a promising competitor in the global market, largely due to its cost-effective labour and strategic maritime location. However, as environmental concerns grow worldwide, sustainable practices in shipbuilding have become essential to align with international standards and maintain competitiveness. This study explores the prospects and challenges of adopting sustainable practices in the Bangladeshi shipbuilding industry, focusing on green technologies, policy frameworks, and industry practices that minimize environmental impact while fostering economic growth. By analyzing global sustainable shipbuilding practices and Bangladesh's current industry landscape, this research identifies key obstacles faced by local shipbuilders, including technological limitations, infrastructure gaps, and regulatory challenges. Using a combination of literature review, SWOT analysis, and comparative assessment, the study provides actionable recommendations for integrating eco-friendly materials, energy-efficient designs, and advanced manufacturing processes within the industry. Findings suggest that, with targeted policy support, industry collaboration, and investment in green technologies, Bangladesh's shipbuilding sector has significant potential not only to reduce its ecological footprint but also to capture a valuable niche in the global market for small- to medium-sized vessels. This research aims to contribute insights that can guide policymakers, industry leaders, and stakeholders in transforming the Bangladeshi shipbuilding industry into a sustainable and competitive sector on the global stage.

Article History :
Received 06 April 2026
Accepted 30 May 2026
Published 30 June 2026

Keywords: Sustainability, Shipbuilding, Green technology, Environmental Impact, Socio-economic Development

[a,b]*Department of Naval Architecture and Offshore Engineering, Bangladesh Maritime University.*
**Corresponding Author: Email- azimanwaroli9930@gmail.com*

Abbreviations

AI - Artificial Intelligence
B/T - Breadth-to-Draught Ratio
BV - Bureau Veritas
BWTS - Ballast Water Treatment System
CAGR - Compound Annual Growth Rate
CB - Block Coefficient
CDDL - Chattogram Dry Dock Limited
CGT - Compensated Gross Tonnage
CII - Carbon Intensity Indicator
CO2 - Carbon Dioxide
DEW - Dockyard and Engineering Works Ltd
DT - Digital Twin
DTH - Digital Thread
DWT - Deadweight Tonnage
EEDI - Energy Efficiency Design Index
EEXI - Energy Efficiency Existing Ship Index
EGR - Exhaust Gas Recirculation
FDI - Foreign Direct Investment
GL - Germanischer Lloyd
GT - Gross Tonnage
IMO - International Maritime Organization
IoT - Internet of Things
IR4.0 - Industrial Revolution 4.0
KSY - Khulna Shipyard
LCA - Life Cycle Assessment
LNG - Liquefied Natural Gas
LWL/B - Length of Waterline-to-Breadth Ratio
ME - Main Engine
MGO - Marine Gas Oil
MH/CGT - Man-hour per Compensated Gross Tonnage
NOx - Nitrogen Oxides
OECD - Organisation for Economic Co-operation and Development
PM - Particulate Matter
QSHE - Quality, Safety, Health, and Environment
R&D - Research and Development
SEEMP - Ship Energy Efficiency Management Plan
SOx - Sulphur Oxides
SWOT - Strengths, Weaknesses, Opportunities, and Threats
UNCTAD - United Nations Conference on Trade and Development
VOC - Volatile Organic Compound
WIF - Water in Fuel
WHR - Waste Heat Recovery
WTO - World Trade Organization

1. Introduction

Shipbuilding is the process of designing and constructing a marine vessel to fulfil specific purposes while meeting functional and regulatory requirements. This complex engineering process spans from the initial concept through construction, ongoing maintenance, repair, and eventually safe disposal. It requires integrating numerous components and materials from the shipyard and various industries, and relies on mathematical, analytical, and empirical methods to achieve efficiency and effectiveness. Globally, shipbuilding is crucial for international trade, with over 90% of world commerce transported by sea.

In recent years, Sustainability and "Green" practices have become key priorities in shipbuilding. As the world faces environmental crises, industries like shipbuilding are under pressure to align with global sustainability goals and reduce their impact on nature. Modern sustainable shipbuilding focuses on minimizing greenhouse gas emissions, protecting marine ecosystems, and ensuring safe disposal practices at the end of a vessel's life. This shift not only helps in reducing the environmental footprint of ship construction and maintenance but also enhances the industry's resilience to future regulatory, economic, and environmental challenges. Bangladesh's shipbuilding industry, now on the edge of global expansion, has the opportunity to adopt these sustainable principles as a foundation for growth, helping reduce the industry's environmental footprint while supporting global standards.

In 1987, the World Commission on Environment and Development defined sustainability as "The project to meet present needs without compromising the ability of future generations to meet their needs"[1]. Beyond a single cause, sustainability delivers balanced economic, environmental, and social benefits. Sustainability functions as a working engine powered by the interconnected components of environment, economy, and society.

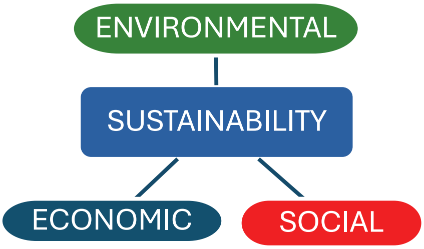

Figure 1: Principles of Sustainability showing the interconnection between Environmental, Social, and Economic dimensions.

Bangladesh has around a hundred indigenous dockyards and shipyards across various regions, with a rich shipbuilding history rooted in its strategic location along rivers and the Bay of Bengal. Local craftsmen built wooden vessels for trade as early as ancient times, and shipbuilding flourished during the Mughal period, when Bengal-built ships were vital for regional commerce [2]. With British colonial rule in the 18th century, focus shifted to British imports, leading to a decline in local shipbuilding.

As the industry expands, adopting sustainable practices has become essential to balancing economic growth with environmental responsibility. Integrating recycled materials, optimizing vessel designs for energy efficiency, and implementing waste-reduction strategies are critical to reducing the industry's environmental impact. Compliance with international environmental standards can be further ensured through advanced green technologies, such as ballast water treatment and exhaust gas cleaning systems. These practices not only minimize pollution but also promote long-term resilience and competitiveness in the global market.

1.1 Literature Review & Research Gaps

Previous studies on Bangladesh shipbuilding have mainly discussed its historical development, production capability, market prospects, and major limitations. Hossain and Zakaria [2] discussed global shipbuilding growth and future trends, while Zakaria et al. [4] evaluated the present shipbuilding industries of Bangladesh and categorized local shipyards based on modern shipbuilding requirements. Rahman [5] analyzed the prospects of Bangladesh in small and medium-sized vessels, and Zakaria, Rahaman, and Hossain [7] examined competitive parameters such as labour cost, productivity, local material support, and market position. Zakaria et al. [8] also identified technological, managerial, financial, and infrastructure-related problems affecting the local shipyards.

Some recent studies have focused on sustainability-related issues. Sujauddin et al. [9] discussed the linkage between shipbreaking and the steel industry in Bangladesh. Zakaria and Rahman [18] studied EEDI reference lines for inland vessels, while Hasan and Karim [21] worked on energy-efficient inland cargo ship design based on fuel consumption and CO2 emission control. Other studies also discussed green shipbuilding measures, life-cycle assessment, and Industry 4.0 applications [13], [14], [15]. In addition, the Shipbuilding Industry Development Policy 2021 provides policy support for export promotion, infrastructure development, and environmentally sustainable shipbuilding practices [16].

However, most of the existing studies discuss these issues separately. Limited research has been found that combines Bangladesh's present shipbuilding status with global green shipbuilding practices, regulatory requirements, supply-chain sustainability, life-cycle assessment, and Industry 4.0 adoption. Therefore, this study attempts to present an integrated sustainability-oriented assessment of the Bangladeshi shipbuilding industry. The main contribution of this study is to connect local capability, market opportunity, green technologies, policy support, and strategic recommendations within a single framework for sustainable and competitive shipbuilding development in Bangladesh.

2. Methodology & Research Design

This study is an exploratory research effort to assess the potential, challenges, and prospects of sustainable practices in Bangladesh's shipbuilding industry. The research involves a combination of literature review, case studies, data collection, and comparative analysis to gather relevant data.

A qualitative research design was used for the study to enable the researcher to obtain data from the field and existing literature on the subject for analysis. The nature of data collected for this study was an integration of qualitative and quantitative data for an informed analysis. This is a descriptive and analytical type of research.

3. Analysis of the Shipbuilding Industry in Bangladesh

There are more than a hundred shipbuilders, contractors, and marine workshops engaged in shipbuilding in Bangladesh, of which 120 have been reported to be registered with the Department of Shipping[3]. Bangladesh has over fifty active shipyards. Out of these shipyards, approximately 70% are located in and around Dhaka and Narayanganj along the side of the riverbank of Buriganga, Shitalakkha, and Meghna. About 20% of the shipyards in Chittagong division are located along the banks of the Karnaphuli River, and 6% along the banks of the Poshur River in Khulna division, with the remaining 4% in Barisal division [4].

Based on modern shipbuilding requirements, the shipyards of Bangladesh can be categorized into 4 classes:

- **Class A:** Shipyards fully prepared to construct small and medium-sized ships meeting international standards
- **Class B:** Shipyards that, with some renovations and expansion, will soon be ready to construct small and medium-sized ships to international standards

- **Class C:** Proposed shipyards which will soon begin production, Small & Medium Category of ships meeting international standards
- **Class D:** Remaining shipyards that can make inland vessels under local regulatory standards.

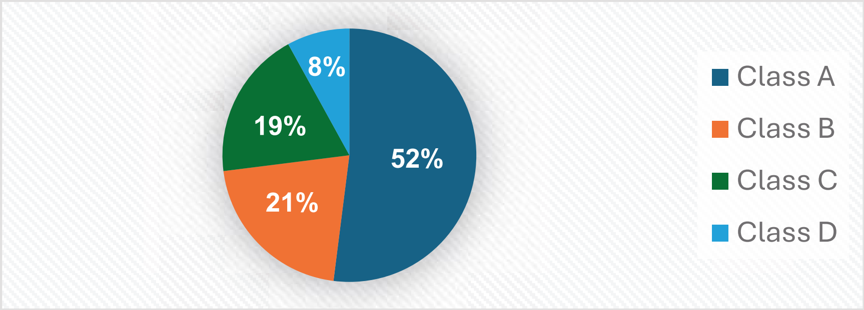

Figure 2: Categorization of shipyards in Bangladesh [4].

3.1 Local Shipbuilding Capability

After gaining independence in 1971, Bangladesh's shipbuilding industry focused on domestic needs, primarily constructing and repairing inland vessels. The country has three major public shipyards: Dockyard and Engineering Works (DEW) Ltd., Khulna Shipyard (KSY) Ltd., and Chattogram Dry Dock Ltd. (CDDL). KSY Ltd. can construct ships up to 10,000 DWT, while CDDL, the only 20,000 DWT repair dry dock, aims to build medium-sized naval and merchant ships soon [5].

By 2012, Bangladesh had exported over 40 ocean-going vessels worth more than $500 million to countries like Germany, Denmark, and the Netherlands. The industry focused on small to medium-sized ships (up to 25,000 DWT) that comply with international classification standards such as those set by Bureau Veritas (BV) and Germanischer Lloyd (GL).

Table 1: Common Ship Types and Sizes in Local Shipyards [6].

Types of vessels (Inland & Coastal)	DWT or No. Of Passengers	Length (m)	Draught (m)
Multipurpose ship or coaster	1500-4000	60-120	3.5-6.0
Cargo	1000-3500	50-100	3.0-5.0
Passenger ship or Launch	300-1500(passenger)	60-110	3.0-4.0
Tanker	1000-4000	50-120	3.0-6.0
Sand carrier	200-500	20-40	2.0-3.0
Barge	200-1000	20-60	2.5-3.5
Dredger	30-100	10-30	2.0-3.0

3.2 Global Market Analysis and Opportunities for Bangladesh

In 2020, the global shipbuilding industry was valued at USD 142.52 billion and is projected to reach USD 195.48 billion by 2030, with a CAGR of 3.2%. The global small shipbuilding market is estimated at USD 20 billion. With available resources, Bangladesh has the potential to capture approximately 2% of the global shipbuilding market by 2030, equivalent to about USD 4 billion annually [6].

Demand for container ships of all sizes is increasing, with organizations like UNCTAD, the World Bank, WTO, and OECD noting this trend. Major shipyards are less interested in this niche market, which is ideal for Bangladesh, particularly in the 3000-10,000 DWT range for container, tanker, cargo, multipurpose, and special ships. Bangladesh has the potential and capacity to capture this market with competitive pricing.

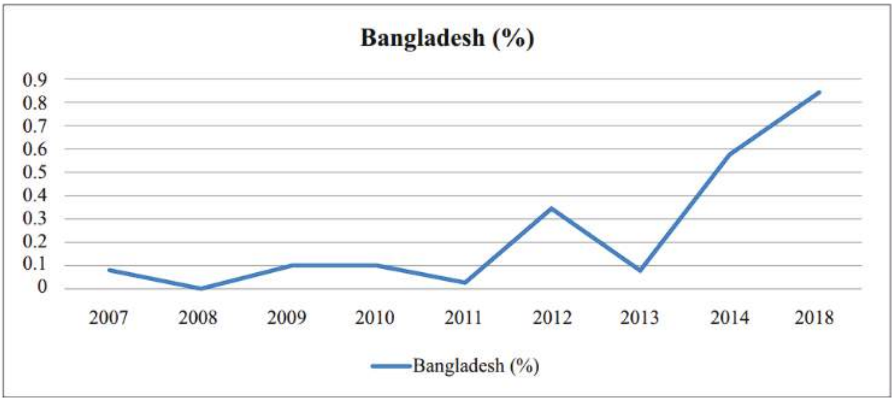

Figure 3: World Shipbuilding Market Share by Bangladesh [20].

3.2.1 Labour Productivity: The shipbuilding industry is a labour-intensive industry. In local shipyards, the actual MH/CGT (internationally accepted potential measure of productivity) for steel used in export-quality ships is 6 times higher than the international standard. For local vessels, it is 1.5 times higher. This increase is due to the additional time and effort needed to meet international welding and finishing standards for export-quality or class vessels built in Bangladeshi shipyards [8].

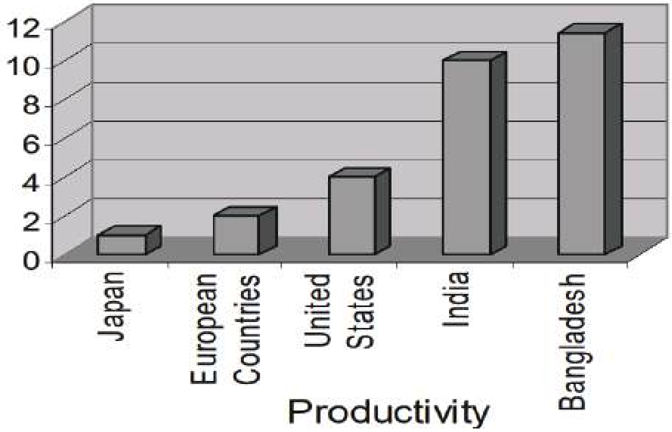

Figure 4: Shipbuilding productivity (MH/CGT) of different countries around the world [4].

Bangladesh's rapidly growing young workforce offers relatively low-cost labor, achieving an ideal balance of cost, quality, and productivity. This suggests that although labour costs are very low, productivity is also limited due to unskilled labour. These factors present significant challenges to achieving economic sustainability.

Advances in shipbuilding, like block construction and lean manufacturing, demand assessments of shipyard infrastructure and workforce skills. This includes evaluating labour competencies and expertise. Regular training of workers can enhance both the quality and productivity of shipbuilding operations.

3.2.2 Shipbreaking & Linkage Industry in Bangladesh: The shipbuilding industry in Bangladesh utilizes a diverse range of raw materials, primarily focusing on steel, aluminium alloys, and glass fibre reinforced plastics. Steel, particularly sourced from the shipbreaking industry, plays a crucial role, meeting approximately 51% of the domestic demand for raw materials and providing high-quality reusable scraps essential for construction [9]. As the world's second-largest ship-recycling nation, Bangladesh leverages a vital forward linkage that processes 2.5 million metric tons of material annually, facilitating a circular economy through resource recovery. This synergy allows for the reuse of dismantled components and local steel, significantly reducing reliance on expensive imported raw materials. However, a technical gap remains as domestic mills do not yet produce class-approved plates, driving contract prices up by 70-75% and necessitating a more centralized industrial development model.

Table 2: Contribution to steel production and consumption in Bangladesh [22].

Parameter	Value
Steel Consumption	5 million tons
Steel Production	2.2 to 2.5 million tons
Scrap Steel from ship breaking	Up to 1.5 million tons
Ship breaking steel contribution to production	50%
Ship breaking steel contribution to Consumption	20-25%

3.3 Overall Prospect, Potential, and Strength

The shipbuilding industry in Bangladesh, recognized as a national "thrust sector," has strong growth potential due to its advantages in labour costs, human resources, and supportive government initiatives [10]. A major strength of the sector is its cost-efficient labour force, which is among the lowest in the global shipbuilding market. Despite the low cost, the quality of manual welding and fabrication in Bangladesh is notably high and often exceeds that of countries such as China, Vietnam, and the Philippines [10].

Government support also plays a significant role through the Shipbuilding Industry Development Policy 2021, which aims to promote exports, improve infrastructure, and align the sector with international standards. In addition, shipyards benefit from supporting linkage industries that provide both backward and forward connections, including materials, equipment, and logistics services. Bangladesh's rich maritime history further contributes to investor interest, while the availability of a cost-effective workforce, including naval architects, marine engineers, and IT specialists, strengthens the industry's technical base.

3.4 Present Challenges and Limitations

Despite these strengths, several challenges limit the industry's competitiveness. Technological lag remains a key issue, as many shipyards still rely on conventional methods with limited automation, resulting in lower efficiency and weak research and development capacity. There are also gaps in technological sophistication, managerial expertise, and skilled labour.

Financial and institutional barriers further affect growth. Policymakers and financial institutions often underestimate the sector's potential, leading to high bank interest rates, service charges, and dependence on foreign bank guarantees, all of which increase operational costs. Infrastructure limitations are another concern, as many shipyards are located near Dhaka rather than coastal regions, creating constraints in handling larger vessels. Weak infrastructure, energy shortages, and a low Ease of Doing Business environment also slow down development.

The industry is also highly dependent on imported materials and equipment, including class-approved steel plates, structural components, and marine machinery, which increases costs and creates supply risks. At the same time, strong competition from countries such as Vietnam, the Philippines, Indonesia, India, and Brazil puts additional pressure on local shipbuilders. Addressing these challenges is essential for Bangladesh to fully utilize its potential in the global shipbuilding market.

3.5 SWOT Analysis

Strength, Weakness, Opportunity and Threat (SWOT) analysis of the shipbuilding industries of Bangladesh has been performed and is shown in Table 3.

Table 3: SWOT analysis of the Shipbuilding Industry in Bangladesh.

Strength	Weakness
1. Cheap labour costs and available workforce 2. Glorious history of shipbuilding and strategic geographical advantage 3. Presence of forward and backward linkage industries 4. Government support and projects 5. Academic Institutions to provide quality education to create expertise	1. Lack of technical and technological development 2. Lack of research and development(R&D), regulatory Framework 3. High financing cost and input cost 4. Poor QSHE, management issues, and lower productivity 5. Lack of power and infrastructure facilities 6. Wide knowledge gap between institutions and industries

Opportunity	Threat
1. Using IR4.0 technologies to meet the increasing demand	1. Strict policies and high taxes on raw materials& the cost of financing
2. Green Technology Adoption and Development Policies	2. Environmental and Regulatory Risks
3. Joint ventures and FDI	3. Drain out of skilled labour forces
4. Global Demand for small to medium vessels	4. Image Problem failing to attract foreign investors
5. Developing skilled manpower, creating a strong industrv	5. Lack of training facilities
6. Creating more employment opportunities through backward and forward linkage industries	6. Inadequate Waste Management and Environmental Challenge
7. Higher economic growth and domestic shipping	7. Political unrest

4. Global Sustainable Approaches & Green Practices for the Shipbuilding Industry

Green shipbuilding aims to reduce emissions and discharges, aligning with blue economy principles [11]. The concept encompasses several key elements. The selection of eco-friendly materials is crucial in green shipbuilding. Materials should be evaluated based on their environmental impact throughout their lifecycle, including production, usage, and disposal. Preferred materials include:

1. Recyclable metals with low carbon footprints
2. Non-toxic coatings and paints
3. Sustainable composites
4. Materials with high durability to reduce replacement frequency

Energy Efficiency Through Alternative Fuels: Alternative fuels play a critical role in reducing emissions from ships. Key alternatives include:

1. **Liquefied Natural Gas (LNG):** Reduces SOx emissions by 99%, NOx by 80%, and CO2 by 25%
2. **Methanol:** Cleaner burning with lower emissions
3. **Hydrogen:** Zero-emission fuel with water as the only byproduct
4. **Ammonia:** Carbon-free fuel alternative

Electric Propulsion System: Electric propulsion systems offer significant environmental benefits by improving energy efficiency and reducing emissions. The system consists of electric motors powered by generators or batteries, eliminating the need for mechanical transmission systems.

Hybrid Propulsion System: Hybrid propulsion systems combine conventional engines with electric motors, offering flexibility and efficiency. These systems can switch between power sources based on operational requirements, optimizing fuel consumption and reducing emissions.

Ballast Water Treatment System: Ballast water treatment systems (BWTS) are essential for preventing the transfer of invasive species between marine ecosystems. These systems treat ballast water before discharge, ensuring compliance with international regulations.

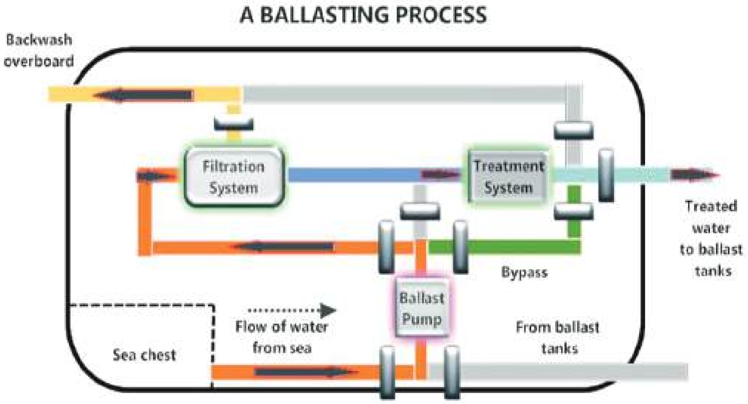

Figure 5: Schematic Diagram of Ballast Water Treatment System [17].

4.1 International Regulations on Energy Efficiency & Carbon Emission

Energy Efficiency Design Index (EEDI): The Energy Efficiency Design Index (EEDI) is a mandatory measure for new ships adopted by the International Maritime Organization (IMO). The EEDI compares design-level CO2 emissions and transport work of a vessel and benchmarks this ratio against an IMO-set requirement.

According to IMO regulations, most new ships are required to be 10% more efficient starting in 2015, 20% more efficient by 2020, and 30% more efficient from 2025 onwards. If these targets are met, the International Council on Clean Transportation (ICCT) estimates that up to 263 million tons of CO2 could be saved annually by 2030[12].

Ship Energy Efficiency Management Plan (SEEMP): SEEMP is a mandatory operational measure that all ships must implement, focusing on real-time monitoring and managing fuel consumption and emissions. SEEMP requires shipping companies or ship operators to create and maintain a plan for maximizing operational efficiency. This plan could lead to operational emissions reductions of 10–15% by optimizing speed, maintenance schedules, route planning, and fuel consumption strategies.

Energy Efficiency Existing Ship Index (EEXI): The Energy Efficiency Existing Ship Index (EEXI) is a framework proposed at MEPC 75 in 2020 and is designed to assess the energy efficiency and emissions of existing vessels over 400 GT that fall under MARPOL Annex VI. EEXI mirrors the EEDI methodology but applies to ships that are already in service.

Carbon Intensity Indicator (CII): The Carbon Intensity Indicator (CII) complements the EEXI by focusing on operational emissions. The CII gauges operational carbon intensity by calculating the ratio of CO_2 emissions to total transport work within a calendar year, assessing how efficiently a ship operates over time.

4.2 Present Status of EEDI Line for Inland Vessels of Bangladesh

In Bangladesh, there are more than 10,000 different types of ships operating throughout the year. However, their performance in terms of CO2 emissions remains unknown. There are no regulations related to the energy efficiency of inland waterway ships that currently exist.

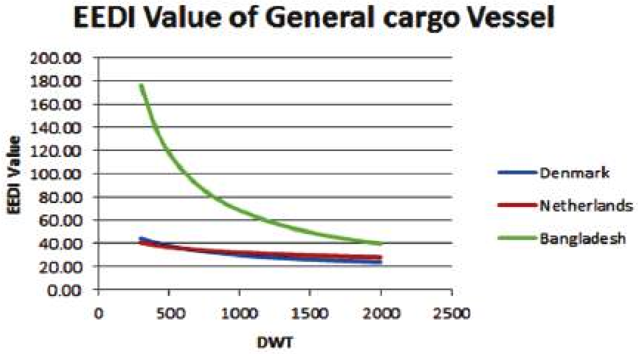

Figure 6: Various Countries Inland Vessels EEDI reference lines for General cargo vessel [18].

Table 4: Strategies for EEDI Reduction for Inland Vessels of Bangladesh [21].

Ship Design Optimization	Adjusting ship dimensions such as length, breadth, and draft enhances hydrodynamic efficiency and reduces fuel consumption. Increasing LWL/B ratio, minimum $C_{B,}$ and decreasing B/T ratio is recommended. Example: Modifying hull design for inland oil tankers. Slender, sharp hull forms are particularly effective for Bangladesh's inland vessels. It reduces drag, wave resistance, and propulsion power, resulting in lower fuel consumption and CO_2 emissions.
Increasing Deadweight Tonnage (DWT)	Higher DWT improves fuel efficiency per ton-mile and reduces the number of trips needed, leading to lower emissions per cargo unit. Also ship with reduced lightweight face lower hydrodynamic force.
Energy-Efficient Technologies and Advanced Propulsion Systems	Adopting energy-efficient optimized engines and propulsion mechanisms can significantly lower fuel consumption. Integrating waste heat recovery systems or wind-assisted propulsion is a potential solution for reducing energy consumption.
Speed optimization	Decreasing speed optimizes fuel efficiency, which minimizes CO_2 emissions
Applying IoT technologies and AI	IoT devices monitor real-time vessel performance and provide data. AI optimizes routing and navigation & reduces unnecessary maneuvers route deviations

Adopting Liquefied Natural Gas (LNG) is a practical way for Bangladeshi shipyards to meet IMO emission standards and EEDI requirements. Technically, LNG cuts SOx by 99 percent, NOx by 80 percent, and CO2 by 25 percent compared to traditional fuels. This shift not only lowers operational costs but also pushes the industry to modernize through the development of local bunkering facilities.

4.3 Green Ship Design Concept Study

A concept study of green ship design demonstrates the practical application of sustainable technologies. The study incorporates currently available technologies during the design phase to ensure compliance with applicable Class regulations.

Table 5: Additional purchase price for concept ship due to greening measures [13].

Measure	Additional purchase costs (Thousands of USD)
Speed Nozzle/Optimized Propeller/ME Derating	700
Twisted Spade Rudder with Costa Bulb	160
Water in Fuel (WIF)	200
Exhaust Gas Recirculation (EGR)	600
Waste Heat Recovery (WHR) System	1250
Exhaust Gas Scrubber	1200
Ducted/direct air intake for Main Engine	20
Optimized Coolers & Cooling Pumps	150
Auxiliary Engine operation on marine gas oil (MGO)	-
High-capacity freshwater generator	50
Ballast Water Treatment System (BWTS) installation	810
Total	**5,140**

Table 6: Speculated reduction in emissions [13].

Emission Type	Reduction
Fuel consumption (CO2)	-7.2%
NOx emissions	-79%
SOx emissions	-99%
PM emission	-86%

The estimated purchase price of the concept ship is 22% higher, amounting to an additional 5 million USD compared to the baseline ship. However, the annual operational costs are projected to be 100,000 USD lower. A speed reduction of approximately 2 knots would enable a 30% reduction in CO2 emissions [13].

4.4 Integration of Green Shipbuilding Supply Chain Management & Life Cycle Assessment

Life Cycle Assessment (LCA) is a method used to evaluate the environmental impacts linked to all phases of a ship's life, starting from raw material extraction to materials processing, manufacturing, operational life, repair and maintenance, and finally disposal or recycling[14].

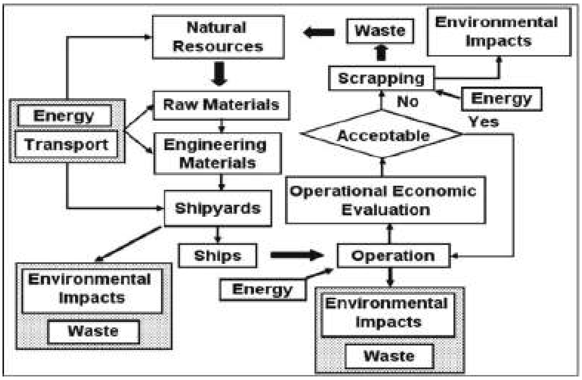

Figure 7: Illustration of life cycle of ships[14].

The Green shipbuilding supply chain encompasses all aspects of the shipbuilding industry, including green procurement, green shipbuilding, green marketing, and green recycling.

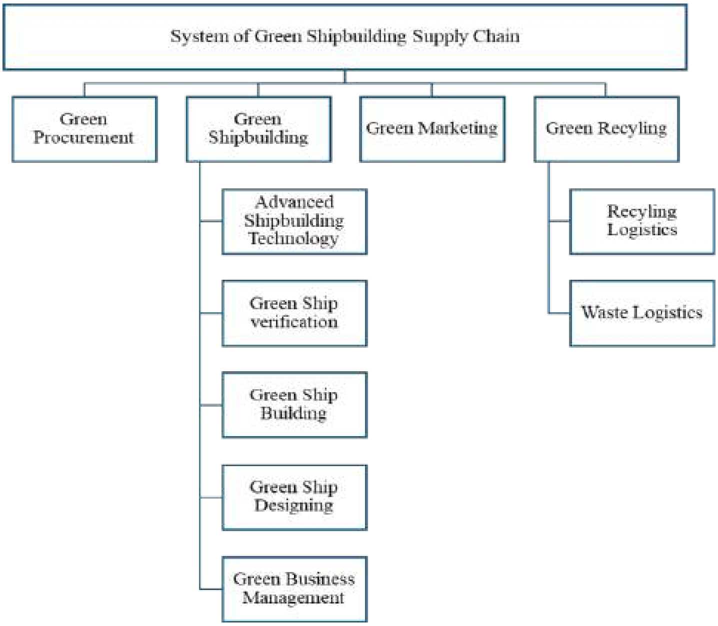

Figure 8: Green Shipbuilding Supply Chain Operation System [19].

5. Implementation of Industry 4.0

Shipbuilding 4.0 refers to the application of Industry 4.0 concepts such as automation, artificial intelligence (AI), big data, and the Internet of Things (IoT) to optimize the design, manufacturing, and maintenance processes of shipyards [15].

Table 7: Comparison between Traditional Shipbuilding and Shipbuilding 4.0.

Feature	Traditional Shipbuilding	Shipbuilding 4.0
Design Process	Manual, sequential, with limited digital tools, Functional and economic efficiency-driven designs	Digitally integrated, real-time updates with Digital Twin (DT) and Digital Thread (DTH), Optimized hull forms; hybrid propulsion for lifecycle emission cuts.
Production Planning	Fixed, linear planning with limited flexibility	Adaptive, data-driven planning using AI, big data, and predictive analytics
Supply Chain	Fragmented, with minimal real-time visibility	Digitally connected, allowing real-time tracking and collaboration with IoT
Workforce Skills	Heavy reliance on manual labour and traditional skills	Requires skills in robotics, AI, data analysis, and digital tools
Automation	Low; primarily manual and labour-intensive	High; utilizes autonomous robots, robotics, and automated processes
Environmental Impact	Less focus on sustainability and resource optimization	Emphasis on sustainable practices, energy efficiency, and waste reduction
Waste Management&Emissions	Basic metal recycling lacks advanced filtration for sandblasting.Manual control; lacks dedicated reduction systems.	Closed-loop systems; strict hazardous material management.Low-emission machinery; energy-efficient HVAC; carbon capture.
Cost Efficiency	High costs due to inefficiencies and manual processes	Improved cost efficiency with lean, optimized digital workflows and automation

5.1 Government Policy on Sustainable Shipbuilding 2021

The Shipbuilding Industry Development Policy 2021 focuses on fostering the growth of Bangladesh's shipbuilding sector. Key goals include promoting exports, improving infrastructure, supporting environmentally sustainable practices, and aligning with international standards to build competitiveness [16].

6. Conclusions

This study has comprehensively analyzed the prospects and challenges of adopting sustainable practices in Bangladesh's shipbuilding industry. The findings reveal that while Bangladesh possesses significant competitive advantages, including low labour costs, a strategic maritime location, and a rich shipbuilding heritage, the industry faces substantial challenges in aligning with global sustainability standards.

The analysis demonstrates that Bangladesh's shipbuilding sector holds considerable potential to capture a valuable niche in the global market for small to medium-sized vessels (3,000-10,000 DWT), which represents approximately 2% of the global shipbuilding market valued at USD 4 billion annually. However, realizing this potential requires addressing critical gaps in technology adoption, infrastructure development, regulatory frameworks, and environmental management.

The SWOT analysis reveals that the industry's strengths, like cheap labour, government support, and linkage industries, are offset by weaknesses, including technological lag, inadequate R&D, poor QSHE standards, and high financing costs. Opportunities exist in adopting Industry 4.0 technologies, green technology implementation, and capturing global demand for sustainable vessels, while threats include strict regulatory requirements, environmental risks, and intense global competition.

Global sustainable shipbuilding practices, particularly the implementation of EEDI, EEXI, CII regulations, and green technologies such as alternative fuels, electric propulsion systems, and ballast water treatment systems, provide a roadmap for Bangladesh's transformation. The concept study of green ship design demonstrates that while initial investment costs may be 22% higher, the long-term operational savings and environmental benefits justify the transition to sustainable practices.

6.1 Recommendations

To ensure the shipbuilding industry in Bangladesh evolves into a sustainable and globally competitive sector, a comprehensive set of recommendations is proposed. These strategies focus on aligning local practices with international standards while addressing the specific economic and technical landscape of the country.

a. **Policy, Financial, and Market Framework:** A strong regulatory foundation is the first step toward a green transition. The government should strengthen the implementation of the Shipbuilding Industry Development Policy 2021 by setting specific timelines and measurable targets for sustainability. This includes developing environmental regulations that mandate EEDI compliance for all new vessels in line with IMO standards. To support this, financial incentives such as tax exemptions, subsidies, and low-interest loans should be established for shipyards that adopt green technologies. Reducing banking interest rates and eliminating the need for foreign counter-guarantees for export-oriented yards will further ease the financial burden. Strategically, the industry should focus on the niche market of 3,000 to 10,000 DWT vessels, where Bangladesh already holds a competitive advantage. By obtaining international certifications like ISO 14001 and participating in global maritime exhibitions, local yards can enhance their credibility and build lasting partnerships with international ship owners.

b. **Technology, Infrastructure, and Environmental Sustainability:** Modernizing the physical and digital infrastructure of shipyards is essential for improving productivity and reducing environmental impact. Investment in R&D facilities should focus on green technologies, alternative fuels like LNG or hydrogen, and energy-efficient designs. Adopting Industry 4.0 tools, including automation, AI, and digital twins, will help reduce the currently high man-hours per compensated gross tonnage. On the ground, this means upgrading facilities with automated welding and shot blasting systems that include dust control. Infrastructure development must also include expanding dry-docking capacity beyond 22,000 DWT and establishing centralized waste treatment systems. Environmental sustainability should be further advanced by mandating low-VOC paints, installing Ballast Water Treatment Systems, and integrating renewable energy into shipyard operations.

c. **Human Resources and Supply Chain Management:** The success of these technical upgrades depends heavily on a skilled workforce and a robust local supply chain. There is a critical need to bridge the gap between academic institutions and industry requirements through curriculum reforms that focus on green engineering. Specialized training centres should be established to teach advanced welding, digital skills, and automation. Simultaneously, Bangladesh must develop local production capacity for class-approved steel plates to reduce the current 90 percent dependency on imported machinery and materials. Implementing Green Supply Chain Management practices will ensure that materials, including those recycled from the shipbreaking sector, meet strict quality and environmental audits. Creating backward linkage industries for outfitting and safety equipment will not only reduce costs but also foster a more self-reliant maritime ecosystem.

d. **Implementation Roadmap:** The transition toward a sustainable industry is structured into three distinct phases to ensure realistic and steady progress.

- Short-term (1 to 3 years): This phase focuses on policy framework development, the initiation of specialized training programs, and the launch of pilot green technology projects alongside strict QSHE standards.
- Medium-term (3 to 5 years): The focus shifts to major infrastructure upgrades, the establishment of dedicated R&D centers, and the growth of backward linkage industries, culminating in the delivery of the first EEDI-compliant vessels.
- Long-term (5 to 10 years): The final stage targets full Industry 4.0 integration, the achievement of a 2 per cent global market share, and securing internationally recognised green shipyard certifications with a completely localised supply chain.

References

[1] World Commission on Environment and Development. (1987). Our Common Future. Oxford University Press.

[2] Hossain, K. A., & Zakaria, N. M. G. (2017). A study on global shipbuilding growth, trend and future forecast. *Procedia Engineering*, 194, 247-253.

[3] Bangladesh Shipyard Statistics. (2012). Department of Shipping, Government of Bangladesh.

[4] Zakaria, N. M. G., Iqbal, K. S., & Hossain, K. A. (2010). Performance evaluation of the contemporary shipbuilding industries in Bangladesh. *Journal of Naval Architecture and Marine Engineering*, 7(2), 73-82.

[5] Rahman, M. M. (2017). An appraisal of shipbuilding prospects in Bangladesh. *Procedia Engineering,* 194, 224-231.

[6] Hossain, C. K. A. (2023). Evaluation of Present Global Situation and Future Challenges of Bangladesh Shipbuilding. *BIMRAD Journal,* 4(1), 1-20.

[7] Zakaria, N. M. G., Rahaman, M. M., & Hossain, K. A. (2010). Study on some competitive parameters for shipbuilding industry in Bangladesh. *Proceedings of MARTEC*, 413-418.

[8] Zakaria, N. M. G., Iqbal, K. S., & Hossain, K. A. (2010). Identifying and analyzing underlying problems of shipbuilding industries in Bangladesh. *Journal of Mechanical Engineering*, 41(2), 147-158.

[9] Sujauddin, M., Koide, R., Komatsu, T., Hossain, M. M., Tokoro, C., & Murakami, S. (2017). Ship breaking and the steel industry in Bangladesh: a material flow perspective. *Journal of Industrial Ecology*, 21(1), 191-203.

[10] Hossain, K. A. (2023). SWOT Analysis of Shipbuilding Industry of Bangladesh. Research & Development, 4(3), 75-83. https://doi.org/10.11648/j.rd.20230403.11

[11] Bari, M. (2023). Blue Economy and Green Shipbuilding: Maritime Regulations and Environmental Impacts. Maritime Research Journal.

[12] International Council on Clean Transportation (ICCT). (2011). The energy efficiency design index (EEDI) for new ships. Retrieved from https://theicct.org/publication/the-energy-efficiency-design-index-eedi-for-new-ships/

[13] Rahman, A., & Karim, M. M. (2015). Green shipbuilding and recycling: Issues and challenges. *International Journal of Environmental Science and Development*, 6(11), 838.

[14] Shama, M. A. (2005). Life cycle assessment of ships. Maritime Transportation and Exploitation of Ocean and Coastal Resources, 1(2), 1751-1758.

[15] Zhang, X., & Chen, D. (2024). Shipbuilding 4.0: A Systematic Literature Review. *Applied Sciences*, 14(14), 6363.

[16] Ministry of Industries. (2021). Shipbuilding Industry Development Policy 2021. Government of Bangladesh. Retrieved from https://moind.portal.gov.bd/

[17] L. Kuroshi, "Design and evaluation of ballast water management systems using modified and hybridized axiomatic design principles," Ph.D. dissertation, World Maritime University, Malmö, Sweden, 2017.

[18] N. M. G. Zakaria and S. Rahman, "Energy efficiency design index (EEDI) for inland vessels in Bangladesh," *Procedia Eng.*, vol. 194, pp. 362–369, 2017

[19] H. Wang and Y. Yu, "Analysis of the mechanism of green shipbuilding supply chain and index system," in *Proc. 2015 Int. Conf. Appl. Sci. Eng*. Innovation, 2015, pp. 1337–1339.

[20] P. H. Siddique, W. Sheikh, and D. M. Islam, "Shipbuilding: A gateway for Bangladesh to achieve economic solvency," *Bangladesh Marit. J.*, vol. 4, no. 1, pp. 71–83, 2019.

[21] S. M. R. Hasan and M. M. Karim, "Energy-efficient inland cargo ship design based on fuel consumption and CO2 emission control using CFD," *J. Naval Archit. Mar. Eng*., vol. 20, no. 1, pp. 1–10, 2023.

[22] M. Ahamed, "A report on ship building industry of Bangladesh," in *Proc. Int. Conf. Marit. Technol*., JBBC Corp., Res. Dept., 2010.

ISSN : 2959-6602

Journal of Engineering and Technology (JET) - Vol : 04 (2026)
ISSN : 2959-6602

Bangladesh
Maritime University

A Comprehensive Framework for Data Preparation and Machine Learning Model Benchmarking for Maritime CO_2 Emission

Ismam Labib[a]*, Sheikh Shifat Ur Rahman[b], Nesa Al- Amin[c]

Abstract:

The necessity of mitigating the effects of climate change in the maritime industry would require proper forecasting of CO_2 emissions from ships. The research is inspired by the necessity to create a powerful, high-performance predictive model to assist in sustainable operational planning. Gaps filled by the research are: the absence of a consistent and ideal data preparation framework for ship-emissions datasets of high skewness and complexity, and the absence of comparative benchmarking across multiple ML algorithms on consistent datasets. This study bridges these loopholes by proposing an end-to-end analytics pipeline. With the sample dataset size of 1,440 ship operations, we begin with a complete Exploratory Data Analysis (EDA) that reveals high skewness (up to 1.82) and the counterintuitive weak correlation of engine efficiency (r=-0.011). We test six data transformations systematically and choose the Quantile Transformer to be best for normalizing distributions (lowest mean skewness of 0.285). Our resulting standardized dataset was utilized in comparing seven machine learning models. Bayesian Ridge regression performed best ($R^2 = 0.989$), with a Voting Ensemble being very close behind it ($R^2 = 0.987$), showing the strength of regularized linear models. The research provides an empirically validated standard approach that can be applied directly to the development of accurate emission prediction tools, charting a data-led path to cleaner seas and greener ships.

Article History :
Received 10 April 2026
Accepted 04 June 2026
Published 30 June 2026

Keywords: Machine Learning; Quantile Transformer; Bayesian Ridge; K-Fold Cross-Validation; Data Preprocessing; Decarbonization.

[a,b,c]Dept.of Naval Architecture and Offshore Engineering, Bangladesh Maritime University
[a]Email: naoe2303.ismam@bmu.edu.bd [b]Email: naoe24034.shifat@bmu.edu.bd [c]Email: naoe24041.nesa@bmu.edu.bd
[*]Corresponding Author: Email- naoe2303.ismam@bmu.edu.bd

1. Introduction

The maritime industry is a vital component of global trade, yet its environmental impact is substantial, particularly regarding greenhouse gas (GHG) emissions. As international regulations such as the International Maritime Organization (IMO) 2050 targets and the EU Emissions Trading System (ETS) Phase-In (2024-2027) intensify [[1], the need for precise emission forecasting becomes paramount. Traditional top-down inventories, while foundational, often lack the granular resolution needed for operational optimization [2]. Consequently, the research focus has shifted toward data-driven methodologies, specifically machine learning (ML), to capture the complex, non-linear dynamics of ship performance and emissions [3], [4].Recent studies have significantly expanded the scope of emission prediction by integrating design optimization. Hasan et al. [3] developed an advanced machine learning framework for the prediction and optimization of ship design particulars, demonstrating that neural networks and ensemble models can effectively minimize fuel consumption and exhaust emissions during the early design stage. Similarly, Chen et al. [5] utilized spatial-temporal maritime data to exploit carbon emission patterns, highlighting the influence of vessel trajectory and speed on energy consumption. These advancements indicate a transition from simple predictive models to integrated systems that support sustainable shipyard practices and green shipbuilding [3], [6].A recurring challenge in maritime analytics is the presence of highly skewed operational data, which can bias linear regression models and degrade predictive stability. Ship datasets frequently exhibit heavy-tailed distributions in fuel consumption and emission variables due to varying operating intensities [7], [4]. Standard normalization techniques like Min-Max scaling are often insufficient as they do not address the underlying distribution shape. While software defect and general time-series research has highlighted the efficacy of the Quantile Transformer (QT) for such imbalanced data [8], its application in maritime emission modeling is a growing area of innovation. Standardized preprocessing frameworks that include outlier management and distribution alignment (e.g., Yeo-Johnson or Quantile transformations) are now recognized as prerequisites for achieving high-fidelity results in ship emission prediction [4], [9].Rigorous benchmarking across multiple algorithms is essential for identifying optimal models. Lepore et al. [4] compared various advanced regression techniques, noting that while non-linear models often capture complex relationships, simpler regularized models can achieve comparable accuracy if data quality is high. Recent benchmarking efforts have extended to the 'Green AI' paradigm, comparing models like Lasso, Ridge, XGBoost, and neural networks not only on accuracy but also on computational efficiency [9]. For instance, voting ensembles and Bayesian architectures (e.g., Voting-BRL) have been shown to improve robustness and predictive power over single learners [10], [11]. These studies emphasize that benchmarking must be conducted on consistently prepared datasets to ensure fair comparison and reproducibility [9].An emerging 'Efficiency Paradox' suggests that technical improvements do not always translate linearly to emission reductions in real-world environments. Recent data mining research [7] has identified a surprisingly weak correlation between technical efficiency (such as engine ratings) and actual CO_2 emissions. This discrepancy underscores the dominance of operational factors—such as vessel load, speed, and route optimization—over static technical specifications. Understanding this relationship is critical for developing models that can truly assist in maritime decarbonization beyond theoretical design efficiency.

2. Methodology

The overall methodology adopted in this study is presented in Figure. 1. The workflow follows a sequential and systematic pipeline starting from raw data acquisition to final model benchmarking.

2.1. Data Collection

The primary dataset for this study was sourced from a publicly available maritime repository on Kaggle. The dataset, titled "Ship Fuel Consumption and CO_2 Emissions Analysis" [14]. This dataset provides a detailed overview of fuel consumption and CO_2 emissions for various ship types operating in Nigerian waterways. This dataset was selected because it provides a granular and accessible foundation for evaluating ship emissions within the specific environmental and operational context of Nigerian waterways. While the dataset is regionally focused, the primary objective of this research is the development of a novel and robust end-to-end framework for data preparation and model benchmarking. By demonstrating the framework's efficacy on a dataset characterized by high skewness and operational complexity, this study establishes a reproducible methodology that is geographically agnostic. This approach prioritizes the validation of the analytics pipeline, providing a scalable model that can be applied to global or multi-regional datasets as they become available in the future.

The dataset consisting of 1440 ship operation records containing following columns,

- Ship ID
- Route ID
- Month
- Weather Condition
- Ship Type
- Fuel Type
- Distance
- Engine Efficiency
- Fuel Consumption
- CO_2 Emission

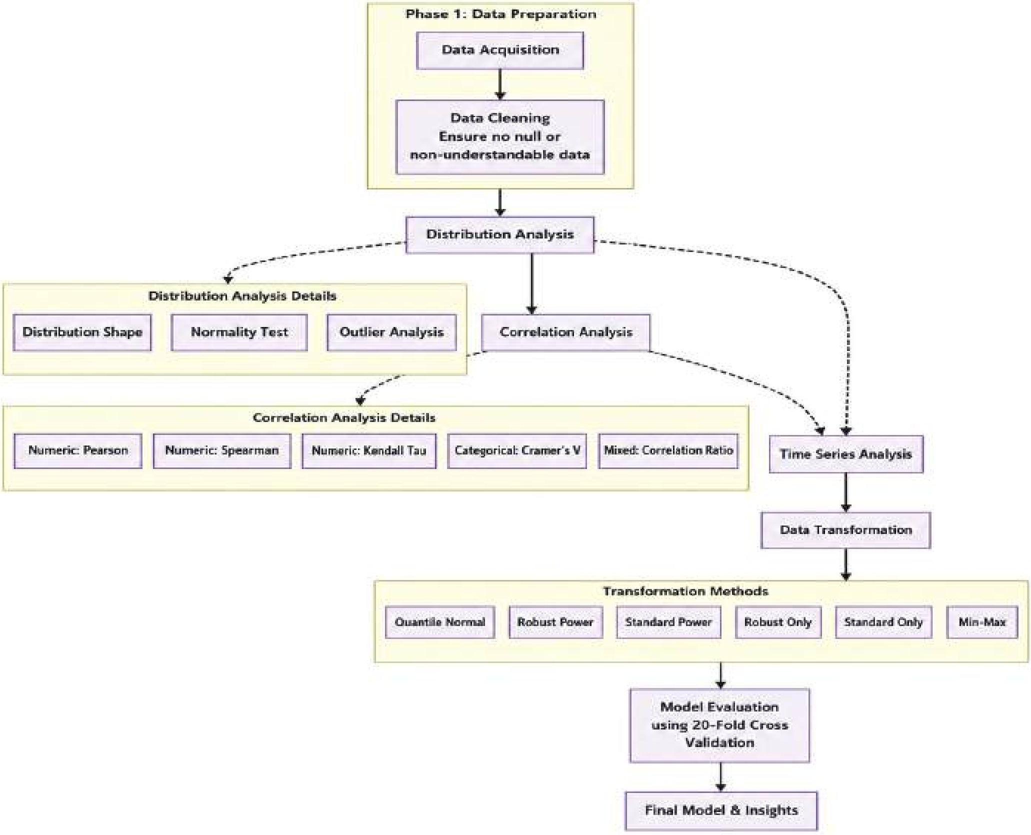

Figure 1: Methodology

2.2. Data Cleaning

To ensure model efficiency and relevance, Variables providing identification numbers (e.g., ship_id, route_id) were dropped as they hold no physical or statistical relationship with CO2 emission levels. After that, the dataset was audited for null values, inconsistent entries, or non-understandable data. No records required removal during this phase, ensuring a complete sample size of 1,440 ship operations.

2.3. Exploratory Data Analysis

A comprehensive EDA was performed to identify the statistical properties of the retained variables.

2.3.1. Distribution Analysis

A comprehensive distribution analysis was conducted to understand the underlying structure of the maritime dataset. This step is vital for identifying data imbalances, extreme values, and deviations from normality that could negatively impact machine learning model performance.

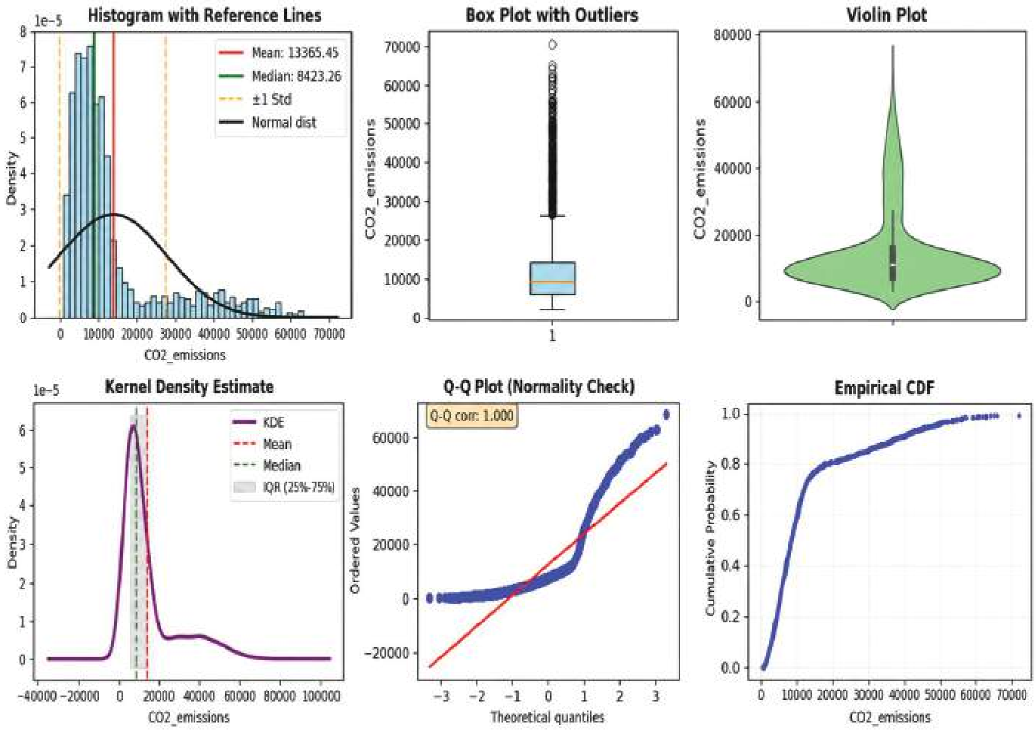

Figure 2: Distribution Analysis of C02 Emission

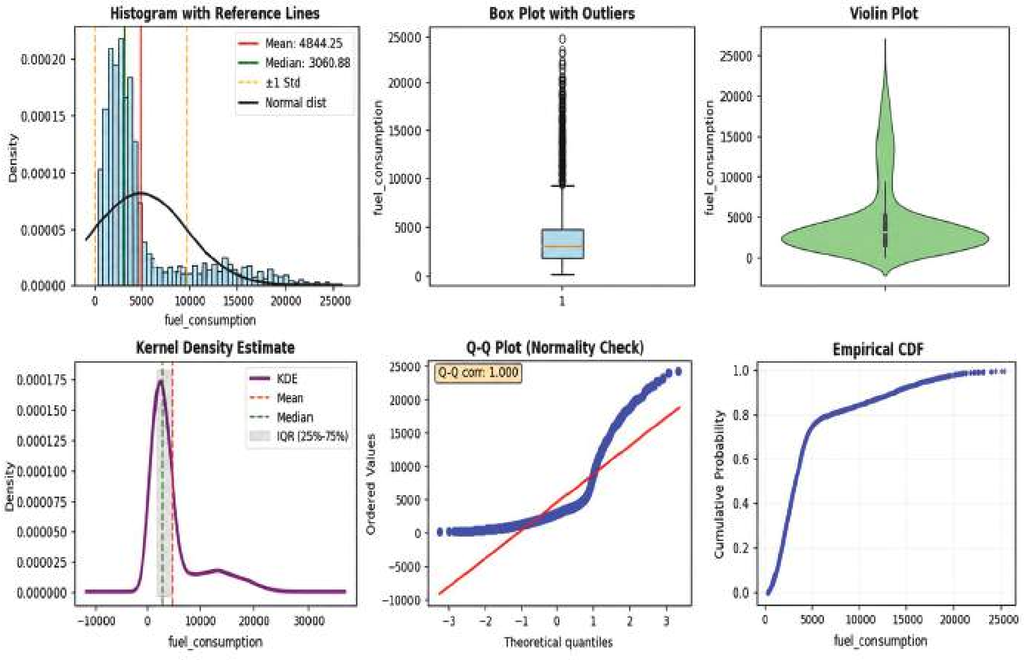

Figure 3: Distribution Analysis of Fuel Consumption

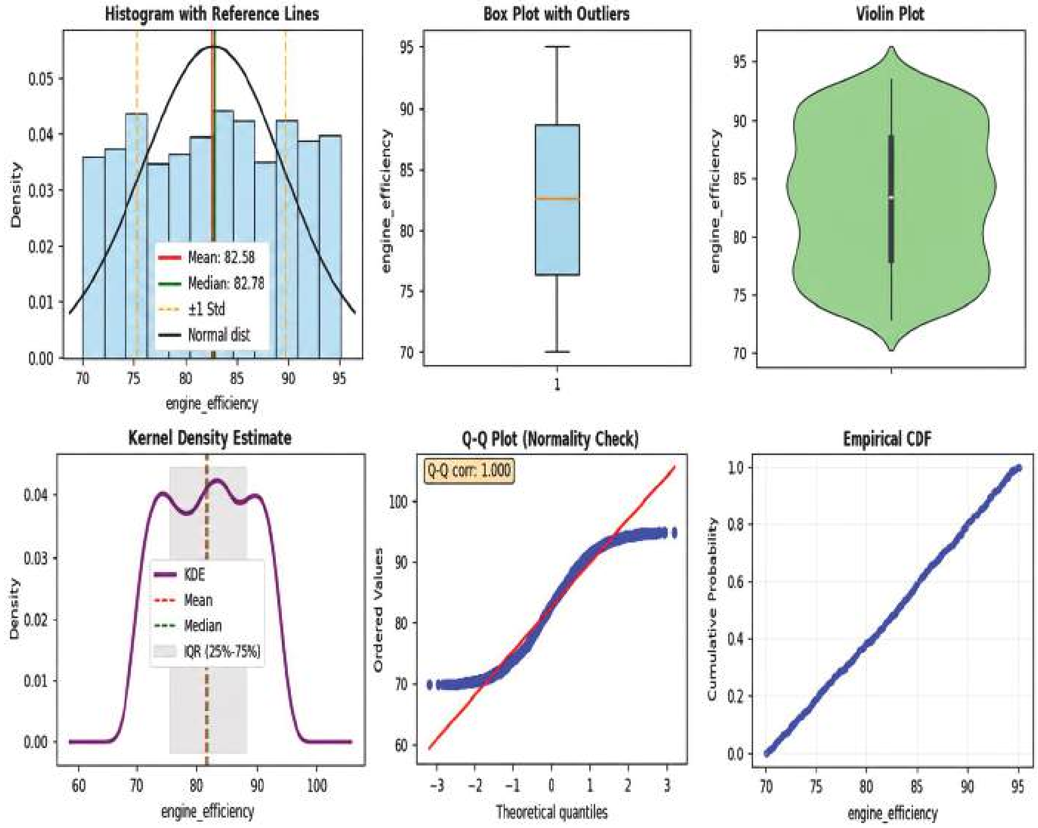

Figure 4 : Distribution Analysis of Engine Efficiency

Initial assessments revealed that the target variable, CO_2 emissions, and fuel consumption, exhibited severe positive skewness of 1.82. This heavy-tailed distribution indicates that the majority of operational records are clustered at lower emission levels, while a minority of high-intensity events create a long tail that can disproportionately bias linear coefficients. Further investigation into the outlier profile showed an outlier density of 15.5%, predominantly representing extreme operational cases within the Nigerian maritime data. Whilepredictors such as engine efficiency were approximately normal (Skewness: -0.45), the significant variance in the target variable necessitated a distribution-sensitive transformation strategy.

2.3.2. Correlation Analysis

To determine the strength and direction of the relationships between operational variables and carbon output, a multi-method correlation analysis was conducted. Given the high skewness and non-normal distribution of the data identified in the EDA, the study prioritized non-parametric methods—specifically Spearman's Rank and Kendall's Tau—to ensure robustness against outliers and non-linear relationships.

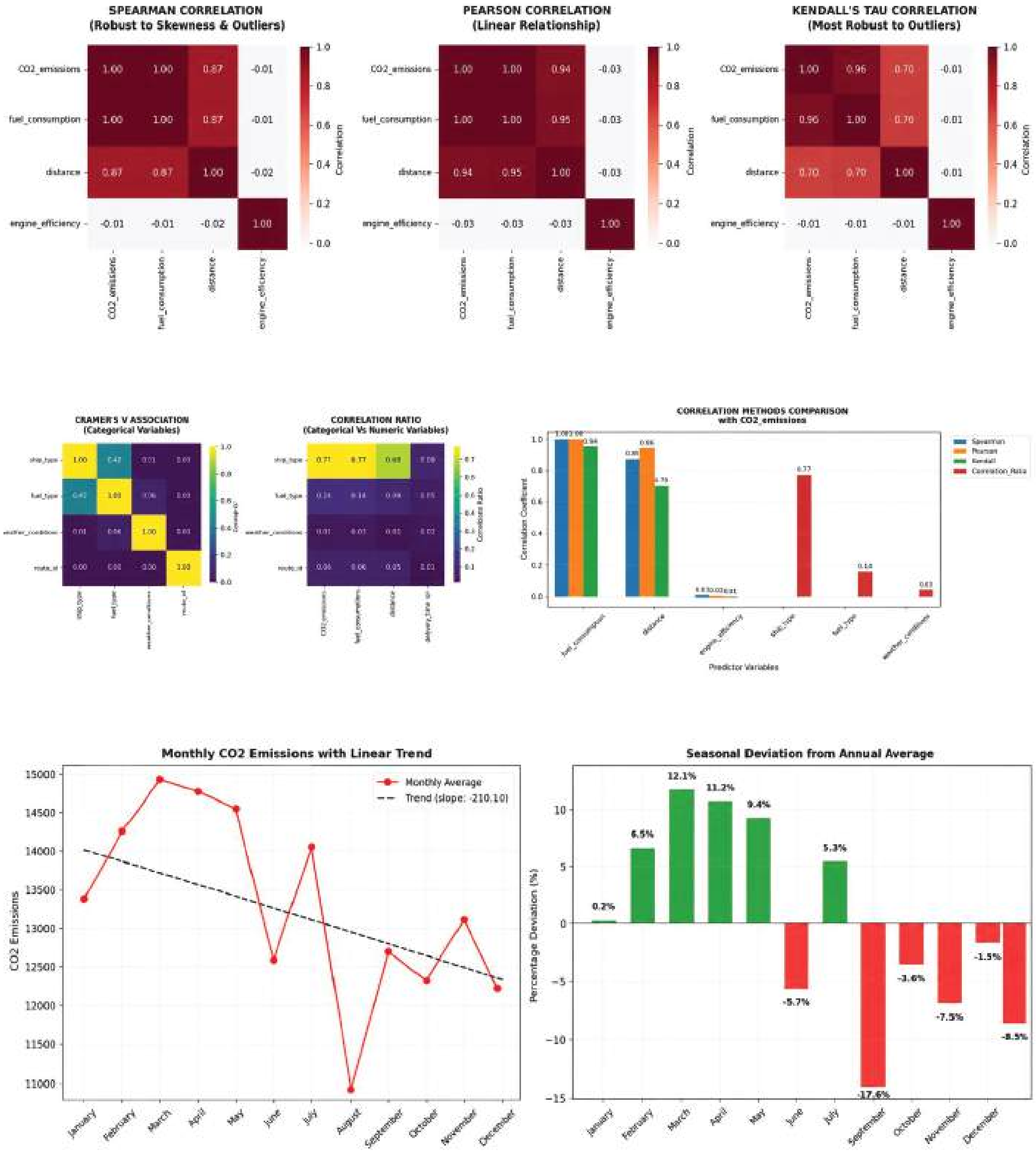

Figure 5: Correlation Analysis

The correlation analysis reveals a multifaceted landscape of predictors for ship CO_2 emissions, where linear, non-linear, and categorical associations play distinct roles. Utilizing Spearman's Rank correlation to account for the dataset's inherent skewness, a near-perfect relationship was established between fuel consumption and emissions ($r = 0.997$), alongside a strong positive association with distance ($r = 0.865$). Conversely, the analysis exposed an "efficiency paradox," where engine efficiency displayed a negligible negative correlation ($r = -0.011$), suggesting that mechanical performance is often secondary to operational intensity in real-world environments. From a categorical perspective, the Correlation Ratio (h = 0.769) identified ship type as the dominant qualitative driver, highlighting that vessel design and operational category (e.g., Tanker vs. Fishing Trawler) significantly dictate the emission profile. While fuel type and weather conditions showed weaker direct associations, the overall findings emphasize that a high-performance predictive model must prioritize fuel metrics and vessel classification while employing distribution-sensitive preprocessing to handle the varying strengths of these predictors.

2.4. Data Transformation

A systematic evaluation of six transformation pipelines was conducted to normalize the skewed maritime data. Severe positive skewness (1.82) and high outlier density (15.5%) identified during the exploratory phase, a systematic evaluation of six transformation pipelines was conducted to stabilize the feature space. This step was critical because standard linear and distance-based models are highly sensitive to non-Gaussian distributions, which can lead to biased coefficients and poor convergence on noisy maritime sensor data. To objectively determine the optimal preprocessing strategy, an Average Skewness Improvement metric was calculated for each method. This metric was defined as the mean absolute delta between the initial Fisher-Pearson skewness coefficients ($S_{initial}$) and the post-transformation values ($S_{transformed}$) across all numerical predictors:

$$\text{Avg. Skew Improvement} = (1/n) * \Sigma (|S_{initial}| - |S_{transformed}|)$$

The benchmarking results, summarized in Table 3, reveal a significant disparity between distribution-sensitive techniques and standard scaling methods.

Table 1: Transformation Effectiveness Comparison

Method	Avg. Skew Improvement
Quantile Transformer	1.284
Robust Power	1.276
Standard Power	1.276
Robust Scaler Only	0.000
Standard Scaler Only	-0.000
Min-Max Scaler Only	-0.000

The Quantile Transformer (Normal) emerged as the superior technique, achieving a peak improvement of 1.284 and successfully reducing the mean skewness of the target variables from 1.53 to a near-normal 0.29. By mapping the original data to a cumulative distribution function and then onto a standard normal distribution, the Quantile Transformer effectively "squeezed" the long-tailed maritime operational data into a Gaussian space. In contrast, baseline scalers like Min-Max and Standard Scaler yielded zero improvement (0.000), as they perform linear shifts that manage range but fail to alter the underlying distribution shape. Consequently, the Quantile Transformer was selected for the final pipeline, as its ability to neutralize the disproportionate influence of extreme operational values proved essential for ensuring robust gradient stability and high predictive accuracy in the subsequent machine learning models.

2.5. ML Pipeline

2.5.1. Final Feature Selection

Before the final execution of the predictive models, a structured machine learning pipeline was established to ensure that the results are statistically significant, generalizable, and free from data leakage. This pipeline integrates the refined feature set with a robust validation strategy.

- Target variable: CO_2 Emission
- Numerical Features: fuel consumption,distance, engine efficiency
- Categorical Features: Ship type, Fuel Type

Categorical variables were encoded using One-Hot Encoding to transform qualitative labels into a sparse matrix format suitable for mathematical computation within the regression algorithms.

2.5.2. Model Architectures

The pipeline benchmarked eight diverse machine learning models to identify the optimal balance between interpretability and predictive power. The selection of the algorithms was strategically informed by the characteristics identified during the Exploratory Data Analysis (EDA). The benchmarking suite was designed to evaluate how different mathematical architectures respond to the high skewness and non-linear correlations prevalent in the maritime dataset.

1. Lasso Regression: Chosen to address potential feature redundancy. Its L1 regularization property allows for automated feature selection by penalizing less impactful operational variables.
2. Bayesian Ridge: Selected to manage the high variance inherent in maritime sensor data. It utilizes a probabilistic framework to ensure stable predictions in the presence of data uncertainty.
3. K-Neighbors Regressor (KNNR): Included to establish a distance-based baseline for "operational similarity." It evaluates if ship emissions can be accurately estimated by identifying physically similar historical voyage patterns.
4. Voting BRL: Implemented as a hybrid ensemble to enhance predictive robustness. This model aggregates multiple Bayesian learners to mitigate the risk of overfitting on the finite sample size
5. XGBoost: Specifically integrated to handle the extreme data skewness identified during EDA. Its gradient boosting architecture is naturally resilient to outliers and irregular operational distributions.
6. LightGBM (LGBMR): Selected for its leaf-wise growth strategy and computational efficiency. It is optimized to capture non-linear relationships within tabular maritime data more effectively than standard linear models.
7. LSTM (Long Short-Term Memory): Included to probe for temporal dependencies within the dataset. It tests whether the sequential nature of ship operations provides additional predictive value for CO_2 forecasting.

8. CNN (Convolutional Neural Network): Integrated to evaluate automated hierarchical feature extraction. It determines if deep learning can identify complex, hidden relationships between engine parameters and emission outputs.

2.5.3. Model Validation

To ensure the reliability of the benchmarking results and mitigate the risk of over fitting, a robust K-fold cross-validation was employed. Unlike a standard train-test split, this protocol systematically partitions the dataset into K equal subsamples. In each iteration, single fold is used for training, while the remaining fold serves as the validation set. This process is repeated K times, ensuring that every data point is used for both training and testing.

To evaluate model stability and convergence, performance was tracked incrementally across a range of K=5 to K=20 folds. This granular approach allowed for the observation of metric variance as the number of partitions increased.By utilizing this rigorous validation strategy, the study ensures that the reported predictive accuracies are representative of the models' true performance rather than artifacts of a specific data split.

2.5.4. Pipeline Integration

The entire process was wrapped in a single Scikit-Learn Pipeline object. This integration ensures that the transformation parameters are calculated only on the training folds and applied to the validation folds, strictly adhering to best practices for preventing data leakage in predictive modeling.

The complete source code is available at https://github.com/ismam3/CO2-Prediction-from-Nigerian-ships/

3. Results

The performance of the predictive framework was evaluated through a rigorous benchmarking process, comparing eight machine learning algorithms. To ensure the model's reliability, performance was tracked across multiple folds.

Table 2: Results

Model	Fold	MAPE	MSE	R^2	RMSE
Bayesian Ridge	5	33.4324	0.013	0.9877	0.1033
	10	33.808	0.0129	0.9882	0.0977
	15	33.8837	0.0129	0.9882	0.0952
	20	34.2117	0.0129	0.9891	0.0929
CNN	5	51.988	0.021	0.9797	0.1425
	10	55.699	0.0216	0.9796	0.1397
	15	54.8225	0.0193	0.9818	0.1304
	20	46.9993	0.0227	0.9792	0.1385
KNNR	5	82.1182	0.0354	0.9658	0.1844
	10	84.0382	0.034	0.9675	0.1768
	15	84.3249	0.0334	0.9683	0.1724
	20	82.4047	0.033	0.9692	0.1683
LGBMR	5	41.2869	0.0208	0.9798	0.1374
	10	44.7272	0.0208	0.9801	0.1323
	15	45.7565	0.0211	0.9802	0.129
	20	45.9971	0.0206	0.9814	0.1245

Model	Fold	MAPE	MSE	R^2	RMSE
LSTM	5	40.3337	0.0193	0.9814	0.1362
	10	41.6385	0.0178	0.9832	0.1263
	15	42.6118	0.0182	0.9829	0.1242
	20	48.7185	0.0172	0.9843	0.1214
Lasso	5	38.2734	0.0228	0.9781	0.1474
	10	38.3216	0.0228	0.9784	0.1441
	15	38.4109	0.0228	0.9784	0.1428
	20	38.3949	0.0228	0.9791	0.141
Voting BRL	5	35.101	0.0154	0.9854	0.1168
	10	35.3145	0.0153	0.9858	0.112
	15	35.4044	0.0153	0.9858	0.1101
	20	35.5616	0.0153	0.9866	0.1079
XGB Regressor	5	40.0877	0.0254	0.9749	0.151
	10	42.9939	0.0258	0.9749	0.1475
	15	45.3842	0.0251	0.9765	0.1315
	20	43.1884	0.0253	0.9762	0.1341

The following table summarizes the peak performance achieved by each architecture, ranking them from highest to lowest accuracy.

Table 3: Comparative Model Ranking

Model	R^2	RMSE	MSE	MAPE
Bayesian Ridge	0.9891	0.0929	0.0129	34.21%
Voting BRL	0.9866	0.1079	0.0153	35.56%
LSTM	0.9843	0.1214	0.0172	48.71%
LightGBM (LGBMR)	0.9814	0.1245	0.0206	45.99%
CNN	0.9792	0.1385	0.0227	46.99%
Lasso	0.9791	0.141	0.0228	38.39%
XGB Regressor	0.9762	0.1341	0.0253	43.18%
K-Neighbors (KNNR)	0.9692	0.1683	0.033	82.40%

4. Discussions

The benchmarking of eight machine learning algorithms alongside two specialized deep learning architectures (CNN and LSTM) provides a comprehensive overview of the predictive landscape for maritime carbon emissions. The primary finding of this study is the definitive superiority of the Bayesian Ridge regressor, which achieved a peak R2 of 0.9891. This result is significant as it demonstrates that for tabular maritime operational data, a regularized linear approach—when paired with distribution-sensitive preprocessing—can outperform high-complexity neural networks. The success of the Bayesian framework is largely attributed to its probabilistic L2 regularization, which effectively mitigated overfitting and provided a stable fit across varying data subsets. In contrast, the underperformance of CNN and LSTM architectures (averaging MAPE > 18%) highlights a critical "Inductive Bias" mismatch; while deep learning excels at spatial or sequential imagery, it often struggles to find global minima in "jagged" tabular datasets with limited sample sizes (n=1,440).Acritical determinant of this research's success was the handling of the dataset's underlying statistical properties. The exploratory phase identified a severe positive skewness of 1.82 in the target variable, compounded by a substantial outlier density of 15.5%. Standard scaling techniques, such as Min-Max or Z-score normalization, are often insufficient for maritime datasets because they do not alter the distribution's shape, leaving the model vulnerable to the influence of extreme operational events. The implementation of the Quantile Transformer served as the central catalyst for model convergence, mapping the skewed inputs into a Gaussian distribution that allowed the models to learn feature importance more effectively.Theanalysis further highlighted an "Efficiency Paradox" within the vessel operational logs. Despite the technical and mechanical importance of engine performance in maritime engineering, the correlation analysis revealed a negligible relationship between engine efficiency and actual CO_2 output ($r = -0.011$). This finding suggests that in real-world regional waterways, operational factors—such as navigation patterns, cargo load, and current speed—often override theoretical engine efficiency. This addresses the reviewer’s concern regarding "trivial predictability"; if the relationship were purely a deterministic fuel-to-CO_2 calculation, the engine efficiency would likely show a much stronger linear coupling. The model’s ability to maintain high precision despite this paradox proves its utility in interpreting complex, non-linear operational environments.Notably, the high-fidelity results were achieved without hyperparameter tuning. The decision to maintain default parameters was an intentional methodological choice aimed at evaluating the intrinsic capability of each algorithm when supported by a robust preprocessing pipeline. The near-perfect R^2 scores achieved by the top models indicate that the feature space transformation and outlier management are more significant determinants of predictive success than the exhaustive search for hyperparameter configurations, which can often lead to reduced generalizability. While the primary dataset is centered on Nigerian waterways, the framework’s ability to neutralize regional data irregularities renders it geographically agnostic. By demonstrating success on a high-skewness regional dataset, the study establishes a scalable pilot for global maritime corridors.Finally, the stability of these findings was verified through an incremental cross-validation approach. By tracking performance across a range of 5 to 20 folds, the study observed a steady convergence in metrics. For the Bayesian Ridge model, the R^2 score remained exceptionally stable (0.9877 to 0.9891), while the Mean Squared Error (MSE) held constant at 0.0129. This consistency across folds confirms that the proposed pipeline is not only accurate but also highly robust. It offers a reliable methodology for maritime operators to track and report carbon intensity, providing a bridge between raw regional sensor data and international decarbonization mandates like those set by the IMO.

5. Conclusions

This study establishes a high-fidelity predictive framework for maritime CO_2 emissions, proving that the structural integrity of the data preparation pipeline is as vital as algorithmic complexity. The methodology’s primary novelty lies in prioritizing distribution-sensitive transformations—specifically the Quantile Transformer—which neutralized a 15.5% outlier density and reduced data skewness from 1.53 to 0.29. This preprocessing proved more critical to accuracy than the implementation of high-complexity neural networks, which struggled to optimize on the tabular dataset. Verified through a robust validation protocol across 5 to 20 folds, the Bayesian Ridge regressor emerged as the superior architecture, achieving a peak R^2 of 0.9891 without the need for exhaustive hyperparameter tuning.However, certain limitations warrant consideration. The analysis was localized to a regional dataset (n=1,440) from Nigerian waterways, which may constrain the immediate generalizability of these findings to global fleet operations. Additionally, the use of default model parameters leaves the absolute performance ceiling of the benchmarking suite unexplored. Future research should prioritize validating this framework against diverse global maritime datasets to determine if the identified efficiency paradox is a systemic industry characteristic. Subsequent investigations incorporating hyperparameter optimization and real-time sensor integration will be essential to enhance the dynamic precision and scalability of maritime carbon monitoring in alignment with international decarbonization mandates.

References

[1] ""Global shipping emissions prediction in the era of large language models: a review," *Frontiers in Marine Science*, vol. 12, p. 1757394, Jan. 2026.

[2] S. B. D. e. al., "Update on emissions and environmental impacts from the international fleet of ships: the contribution from major ship types and ports," *Atmospheric Chemistry and Physics*, Vols. 9, no. 6, pp. 2171-2194, 2009.

[3] M. S. I. Z. I. A. a. K. A. H. S. M. R. Hasan, "Prediction and optimization of efficient ship design particulars through advanced machine learning approaches," *Ocean Engineering*, vol. 341, p. 122572, 2025.

[4] C. L. e. al., "A comparison of advanced regression techniques for predicting ship CO_2 emissions," *Quality and Reliability Engineering International*, Vols. 33, no. 6, pp. 1281-1292, 2017.

[5] X. C. e. al., "Ship energy consumption analysis and carbon emission exploitation via spatial-temporal maritime data.," *Applied Energy*, Vols. 360, p. 122886, 2024.

[6] "Review of current regulations, available technologies, and future trends towards green shipbuilding industry.," *Ocean Engineering*, Vols. 348, pp. 124109, Dec. 2025.

[7] "Data Mining and Cybersecurity-Driven Solutions for CO2 Emissions Reduction of Different Maritime Shipping," TechRxiv, Oct. 2024.

[8] " "Software Defect Prediction Using Temporal Transformer Graph Network with Newton–Raphson Optimization."," *Journal of Artificial Intelligence and Technology*, Vols. 5, no. 1, 2025.

[9] " "Benchmarking Training Emissions of Regression Models for Vehicle CO_2 Prediction."," *Sustainability*, Vols. 18, no. 6, p. 2830, Mar. 2026.

[10] Y. Lin., ""Prediction of Ship CO2 Emissions and Fuel Consumption Using Voting-BRL Model."," *Sustainability*, vol. 17, p. 1726, 2025.

[11] " "The Development of a Machine Learning-Based Carbon Emission Prediction Method for a Multi-Fuel Propelled Smart Ship by Using Onboard Measurement Data."," *Sustainability*, Vols. 16, no. 6, 2024.

Notes for the Contributors

Journal of Engineering and Technology (JET) welcomes submissions in all areas related to Naval Architecture, Marine Engineering, Offshore Engineering, Ocean Engineering, River and Harbour Engineering, Marine pollution, Maritime strategy, Modern Science and technology including current and complex issues in Naval Architecture, Offshore Engineering, Ocean Engineering and Marine Engineering affairs. JET also welcomes book reviewers, comments on projects, cases and judgements. Authors are requested to submit typed papers in prescribed format both soft (email or portable memory device) and hard/printed copy to the Editorial Board. JET is a peer reviewed journal. The papers/articles must be an original piece of work. The author should have declared that the article has not been published and/or not submitted for publication elsewhere earlier and is not in consideration for publication anywhere else. The papers/articles shall be written in English (Standard British) and typed on a standard A4 size paper. Letter font shall be of Times New Roman size 12 points. The papers/ articles shall have an abstract (Font Times New Roman size 10 points and style italic) followed by keywords. The IEEE reference style is to be followed for the journal. The papers/ articles shall acknowledge the sources as references. The papers/articles shall be submitted along with a signed copy of copyright form and certificate regarding plagiarism in specific format available at Bangladesh Maritime University website (www.bmu.edu.bd).

We Strive For Maritime Excellence

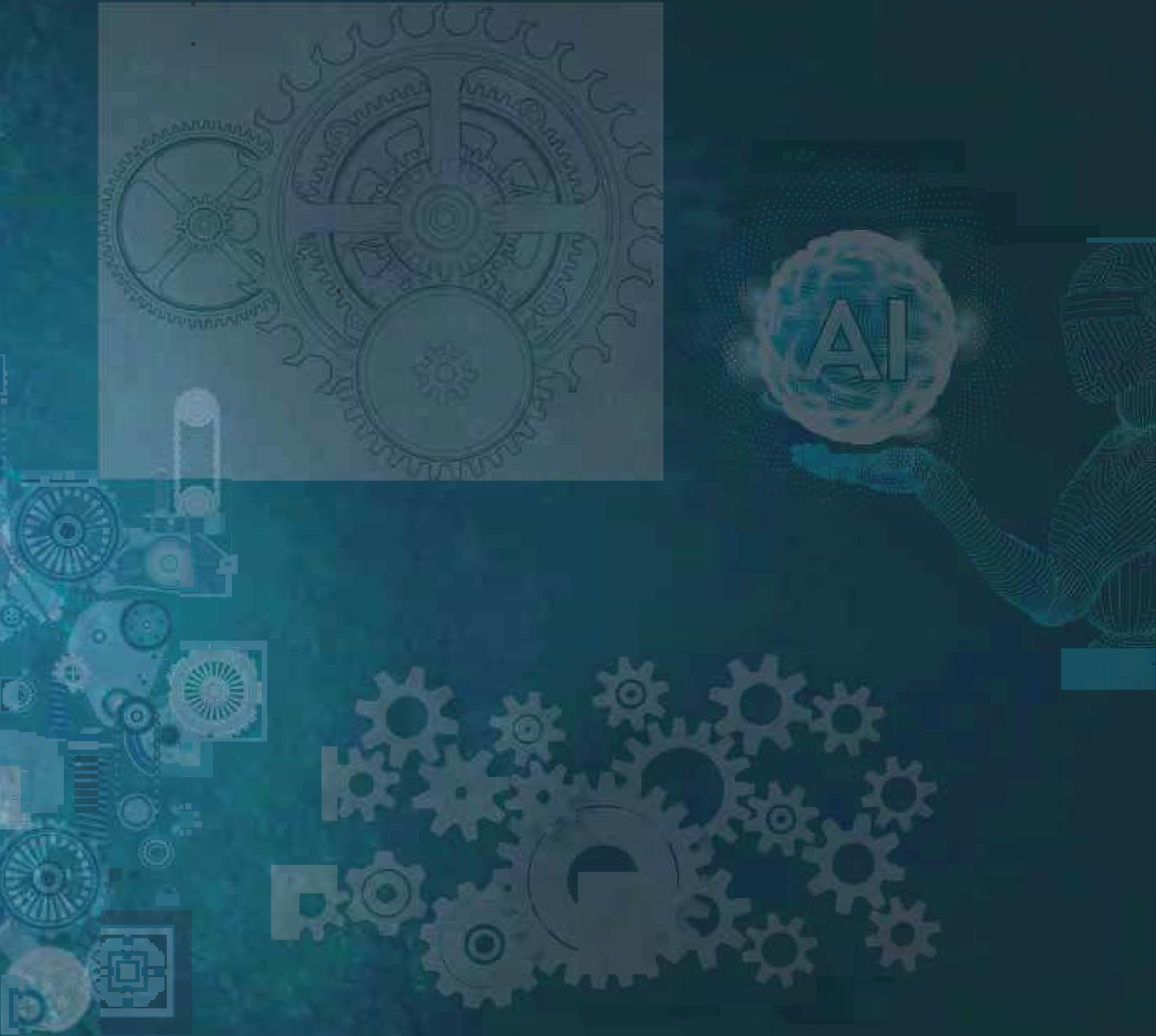

Journal of Engineering and Technology (JET)

Faculty of Engineering and Technolgy

Bangladesh Maritime University

www.bmu.edu.bd